Title

The Progression of Spiropyran as a Chemical Sensor to an Activatable Contrast Agent for MRI

Author

Trevino, Kimberly M.

Publication Date

2023

Peer reviewed|Thesis/dissertation

The Progression of Spiropyran as a Chemical Sensor to an Activatable Contrast Agent for MRI

By

KIMBERLY M. TREVINO
DISSERTATION

Submitted in partial satisfaction of the requirements for the degree of

DOCTOR OF PHILOSOPHY

in

Chemistry

in the

OFFICE OF GRADUATE STUDIES

of the

UNIVERSITY OF CALIFORNIA

DAVIS

Approved:

Angelique Y. Louie, Chair

Marie C. Heffern

Jared T. Shaw

Committee in Charge

2023

ABSTRACT

Spiropyrans (SP) are a class of switchable molecules that exhibit two different isomers; (1) SP "closed" isomer and (2) merocyanine (MC) "open" isomer. Their distinct differences in polarity, structure, and color due to their interchanging ability make them a great candidate as a small molecule sensor. Chapter 1 introduces the origins of spiropyrans and a detailed description of the isomerization to merocyanine. The respective UV-Vis electronic transitions are explained as well as the chemical properties of the two isomers. The layout of this dissertation work is thus described.

Chapter 2 reviews 102 colorimetric copper(II) sensors from the years 2010-2022 and evaluates common metal ions that offered dual detection or anions that interfered with detection. Copper(II) is an essential metal in the body aiding in various physiological functions and is commonly found in the environment. However, excess copper(II) can result in toxicity both biologically and environmentally. Therefore, a sensor for rapid colorimetric copper(II) detection was synthesized. A dimethylamine-functionalized spiropyran (SP-14) was found to selectively and sensitively detect copper(II) over biologically and environmentally relevant metal ions. UV-Vis spectroscopy and DFT calculations were used to investigate the SP-14–Cu^{2+} interaction.

Chapter 3 provides a complete ^{1}H and ^{13}C NMR assignments for three GSH-stabilized MC species as well as their respective individual SP configurations. GSH is a redox active molecule present in the human body that acts as a powerful antioxidant. Alterations in GSH levels are indicative of oxidative stress resulting in several pathological conditions. This chapter further explores the stereochemistry between GSH and merocyanine using NOESY NMR to present a most favorable *trans* conformation. These findings may provide insight in elucidating how SPs interact with other chemical stimuli.

Based on the sensitivity and selectively for GSH, two SPs mentioned in the previous chapter, were utilized in Chapter 4 to construct a manganese-based contrast agent for MRI. Upon examining the literature, variance in GSH concentrations between benign and malignant tumors was noticed. This chapter is directed towards developing an MR agent that can observe fluctuations in GSH concentrations in hopes to discern between these two types of tumors. Details into the individual components chosen for the formation of the agent, the synthetic procedure, testing of the r_1 relaxation rate and future work will be discussed.

ACKNOWLEDGEMENTS

First and foremost, I would like to thank my Trevino, Taufer, Rosa, Moreno, Bossi and Leija family for all their love and support throughout my PhD endeavor. I cherish family and I am so grateful to have achieved this milestone with you guys by my side.

To my husband, Cory Taufer, who was and continues to be an integral person throughout this journey. Thank you for being a constant source of love and stability when the failures of grad school became too much at times. You have the innate ability to refocus my mindset by providing a positive perspective on all outcomes. This gives me the confidence and courage to tackle any obstacle ahead.

Mom and Dad, thank you for always encouraging me to pursue my passions. Whether it was my goal of being a point guard in the WNBA or becoming the first in our family to obtain a PhD. You never questioned my rationality but instead expected me to give it my all. Dad, you once told me you never thought you were smart enough to become a doctor and therefore never tried. I hope this achievement is proof that anything is possible, and I am glad to share this with both of you!

To my principal investigator, Dr. Angie Louie. Thank you for molding me into the scientist I am today. I am so appreciative of the time and effort you spent guiding me to think critically and independently. You eloquently balanced being a boss while also providing encouragement through troubling and exciting times, and for that I am grateful to call you my friend. To the graduate and undergraduate students in the Louie Lab, thank you for being amazing group members. I will never forget the feeling of camaraderie between a bunch of like-minded people going through the thick of it.

Lastly, I want to thank the staff, faculty and graduate students of the chemistry and biomedical engineering department for their guidance and support. Especially, my dissertation committee members, Dr. Jared Shaw and Dr. Marie Heffern, for providing thoughtful advice and feedback. To all the people not mentioned but had even the slightest impact on this achievement, thank you.

"Success is not final. Failure is not fatal. It is the courage to continue that counts."

Winston Churchill

TABLE OF CONTENTS

INTRODUCTION 1

CHAPTER 1: AN INTRODUCTION TO SPIROPYRANS 4

1.1 THE CHEMICAL PROPERTIES OF SPIROPYRANS 5

1.2 THIS WORK 8

CHAPTER 2: EMPLOYMENT OF SPIROPYRAN AS A COPPER(II) SENSOR 9

2.1 SMALL MOLECULE COPPER(II) SENSORS AND THEIR USE FOR COLORIMETRIC DETECTION 10

2.1.1 IMPORTANCE OF COPPER AND COPPER SENSING 10

2.1.2 CURRENT METHODS FOR DETECTING COPPER(II) 11

2.1.3 CURRENT COPPER(II) SENSORS 11

2.2 HIGHLY SENSITIVE AND SELECTIVE SPIROPYRAN-BASED SENSOR FOR COPPER(II) QUANTIFICATION 15

2.2.1 SP-14 AS A COPPER(II) SENSOR 15

2.2.2 SYNTHESIS OF SP-14 17

2.2.3 RESPONSE TO LIGHT AND REFERENCE COMPOUNDS (PHENOL AND N, N-DIMETHYLANILINE) 18

2.2.4 SENSITIVITY OF COPPER(II) 21

2.2.5 SELECTIVITY OF COPPER(II) 25

2.3 MATERIALS AND METHODS 33

2.3.1 MATERIALS 33

2.3.2 SYNTHESIS AND STRUCTURAL CHARACTERIZATIONS 33

2.3.3 COPPER TITRATION PROCEDURES 35

2.3.4 ABSORBANCE PROFILE OF SP-14 WITH EQUIMOLAR (1X) METAL CHLORIDES 37

2.3.5 Competition studies 37

2.4 Conclusion and future directions 39

Chapter 3: Examination of the merocyanine-glutathione interaction 41

3.1 Glutathione and its biochemical function 42

3.2 Glutathione's effect on spiropyran 42

3.3 Investigating the interaction between merocyanine and glutathione (GSH) through a comprehensive NMR analysis of a GSH-stabilized merocyanine species 45

3.3.1 Synthesis of SP-3, SP-7, & SP-9 45

3.3.2 ^{1}H and ^{13}C NMR assignments of MC-3, MC-7, & MC-9 46

3.3.3 Strategy in determining the spectral assignments for MC-3, MC-7, & MC-9 48

3.3.4 *Examination of NOESY to determine the most favorable conformation for GSH-stabilized MC-3, MC-7, & MC-9* 54

3.4 Experimental Methods 57

3.4.1 *Synthesis and mass spectrometry characterization* 57

3.4.2 *NMR sample preparation* 57

3.4.3 *NMR experiments* 57

3.5 Conclusion 58

3.6 Additional figures 60

Chapter 4: Spiropyran as an activatable MRI contrast agent for Glutathione 76

4.1 Background on MRI 77

4.1.1 Basic principles 77

4.1.2 T_1- VS T_2-WEIGHTED IMAGING 78
4.1.3 T_1 CONTRAST AGENTS 82
4.1.4 ACTIVATABLE CONTRAST AGENTS 83
4.2 THE IMPORTANCE OF GLUTATHIONE IN HUMAN DISEASE 84
4.2.1 GSH VARIANCE IN BENIGN VS MALIGNANT TUMORS 84
4.2.2 METHODS TO DETECT GSH 85
4.3 SPIROPYRAN AS A GLUTATHIONE SENSOR 86
4.4 THE DEVELOPMENT OF A MANGANESE-BASED ACTIVATABLE MRI CONTRAST AGENT RESPONSIVE TO GLUTATHIONE 88
4.4.1 CONCEPT OF A GSH SENSITIVE MRI AGENT 88
4.4.2 SYNTHESIS OF THE ACTIVATABLE CONTRAST AGENT 90
4.4.3 (r_1) RELAXIVITY 91
4.5 MATERIALS AND METHODS 94
4.5.1 MATERIALS 94
4.5.2 SYNTHESIS AND STRUCTURAL CHARACTERIZATIONS 94
4.5.3 RELAXIVITY MEASUREMENTS 101
4.6 CONCLUSION AND FUTURE DIRECTIONS 102

REFERENCES 103

INTRODUCTION

Spiropyrans are molecules exemplified by their switchable nature from "closed" spiropyran (SP) to "open" merocyanine (MC) due to various stimuli such as light, metal ions, thiols etc. The dramatic difference in the chemical properties of the two isomers is what distinguishes them as chemical sensors over other molecular switches. The beginning of this dissertation work, Chapter 1, introduces the origins of SPs, followed by a detailed description of the SP to MC conversion and the resulting distinct chemical properties of the two isomers. In Chapter 2, an SP derivative is utilized for its metal sensing capability. Small molecules, like SPs can display certain electronic and structural features that enable their use for metal-sensing applications in different fields. Of the reported metal sensors, there has been increasing interest in copper sensing in the past decade, given the biological importance of copper as well as its presence as a potential contaminant in water and fuels. Molecules used for copper(II) sensing generally consist of a fluorophore/chromophore and a ligand for selective metal ion recognition. A comprehensive literature review was conducted from the years 2010-2022 concerning small molecule copper(II) sensors that provide a naked-eye color response in solution. In addition, challenges and future prospects of fluorophore/chromophore–ligand chemistry in applications of small molecules for fluorometric and colorimetric assays of copper(II) is discussed. Furthermore, we present a dimethylamine-functionalized spiropyran (SP-14) and demonstrate its metal-sensing properties using UV–Vis spectrophotometry. The formation of a metal complex between SP-14 and Cu^{2+} was associated with a color change that can be observed by the naked eye as low as ≈ 6 μM and the limit of detection was found to be 0.11 μM. Colorimetric data showed linearity of response in a physiologically relevant range (0–20 μM Cu^{2+}) with high selectivity for Cu^{2+} ions over biologically and environmentally relevant metals such as Na^{+}, K^{+}, Mn^{2+}, Ca^{2+}, Zn^{2+}, Co^{2+}, Mg^{2+}, Ni^{2+}, Fe^{3+},

Cd^{2+}, and Pb^{2+}. Since the color change accompanying SP-14–Cu^{2+} complex formation could be detected at low micromolar concentrations, SP-14 could be viable for field testing of trace Cu^{2+} ions.

Expanding on the switchable nature from SP to MC by certain stimuli, Chapter 3 focuses on the utilization of glutathione (GSH) to induce a series of GSH-stabilized merocyanine species: MC-3, bearing a methoxy on the indoline unit, MC-7 bearing a methoxy on the phenolic oxygen and MC-9 bearing a methoxy on both sides. GSH is of importance because it plays a vital role in cell homeostasis by scavenging for reactive oxygen species (ROS) where excess generation of ROS results in oxidative stress leading to the development of various diseases. Thus, insight into the structural interaction between merocyanine and glutathione could potentially aid in elucidating how spiropyrans interact with other chemical stimuli. Therefore, ^{1}H and ^{13}C NMR assignments were determined for these three GSH-stabilized MC species using NMR techniques such as HSQC, HMBC, COSY and NOESY. In addition to elucidating the structural assignments, examination of the NOESY spectrum allowed for stereochemical analysis to provide the most favorable *trans* TTT conformation. Information about how these GSH-stabilized merocyanine species interact with GSH may aid in an improved understanding of the sensing mechanism of spiropyran for GSH.

To further elaborate on the importance of GSH, there have been many studies showing heterogeneity in GSH levels in malignant tumors while benign tumors displayed a more homogeneous GSH concentration. Hence, the ability to differentiate between tumor types would greatly aid in diagnosis. Molecular imaging of GSH is proposed to examine fluctuations of GSH levels in real time without disturbing tissue physiology while MRI is employed as the imagining modality because it is noninvasive and has high spatial resolution. Although GSH has a profound

importance, the reported GSH sensors are limited by sensitivity and selectivity. Thus, in Chapter 4 we proposed the use of a spiropyran-based probe sensitive towards fluctuations in GSH concentrations in the sub micro-molar range. Using a library of spiropyran photoswitches previously synthesized by others in our group, SP-7 and SP-9 were chosen for their selectivity of GSH over biologically relevant metal ions and sensitivity with an LOD of 2.4 µM & 2.2 µM, respectively. SP-7 or SP-9 was conjugated to a 1,4-DO2A chelator and metalated with manganese in lieu of the clinically used gadolinium, due to recent reports on toxicity. Positive electrospray ionization-mass spectrometry, ^{1}H and ^{13}C NMR were used to characterize all products throughout the multistep reaction. Longitudinal (r_1) relaxivity measurements for both MR agents exhibited no change when exposed to GSH but instead were responsive to 374 nm UV light. Further efforts will be directed toward maximizing the conversion to the MC isomer to get the optimal change in relaxivity to be applied as a light activatable agent.

CHAPTER 1: AN INTRODUCTION TO SPIROPYRANS

1.1 THE CHEMICAL PROPERTIES OF SPIROPYRANS

Spiropyrans belong to a class of switchable molecules that were first discovered by Decker and Felser in 1908.[1] Interestingly, the coined term "spiropyran" was based on the non-photoactive derivative that had a chiral center adjoining two pyrans and it wasn't until 1952 when their photochromism was detected by Emil Fischer and Hirshberg.[2] In general, the synthetic pathway involved the condensation of a Fisher base with salicylaldehyde that lead to the discovery of the photoactive spiropyran containing an indoline (green) and chromene (purple) moiety joined by the sp^3-hybridized spirocarbon (Scheme 1.1).

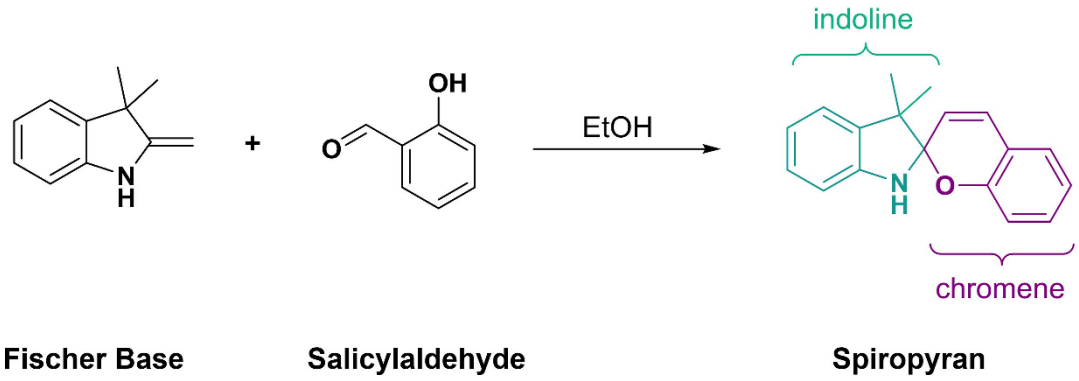

Scheme 1.1. *Synthesis of spiropyran by Fischer and Hirshberg using a Fischer base (methylene indoline) and salicylaldehyde to produce the photoactive derivative composed of an indoline (green) and chromene (purple) unit.*

It was noticed that upon irradiation of the colorless spiropyran in an ethanol or methanol solution, the color became intensely violet red. This was reversible at a rate dependent on temperature and the change in color was only noticed in solution; No such change occurred in solid form. These molecules became attractive to study due to the shift in color seen via naked-eye and many studies

were directed towards understanding this mechanism.[3–6] Figure 1.1 describes the chemical properties as well as the conversion of spiropyran to merocyanine. Initially in the "closed" form, spiropyran is uncharged, hydrophobic, and colorless in solution, absorbing light in the UV region depicted by the purple line in the UV-Vis spectra shown. Two absorption bands, one between 200-300 and the other between 310-400 nm, are attributed to the orthogonal indoline and chromene components providing their own localized π-π* electronic transitions.[7] The band between 200-300 nm is assigned to the indoline moiety while the band between 310-400 is assigned to the chromene unit.[7–10] When spiropyran is irradiated with UV light, it produces enough energy to break the spirocarbon C-O bond (red) and undergoes heterolytic cleavage to afford the merocyanine isomer.[11,12] In the process two electrons are transferred to the indole to generate the positively charged indolium and a negatively charged phenolic oxygen. The "open" merocyanine is zwitterionic, hydrophilic and colored in solution, absorbing light in the visible region depicted by the dashed orange line in the UV-Vis spectra shown in Figure 1.1. A new peak arises in the 450-650 nm range due to the extended π-conjugated system of the merocyanine isomer.[12,13] Converting merocyanine back to spiropyran can be achieved with irradiation of visible light or thermal relaxation (Δ).[14,15] This switching capability and distinct differences in polarity, structure, color and respective absorbance spectrum makes spiropyrans a great candidate as a small molecule sensor.

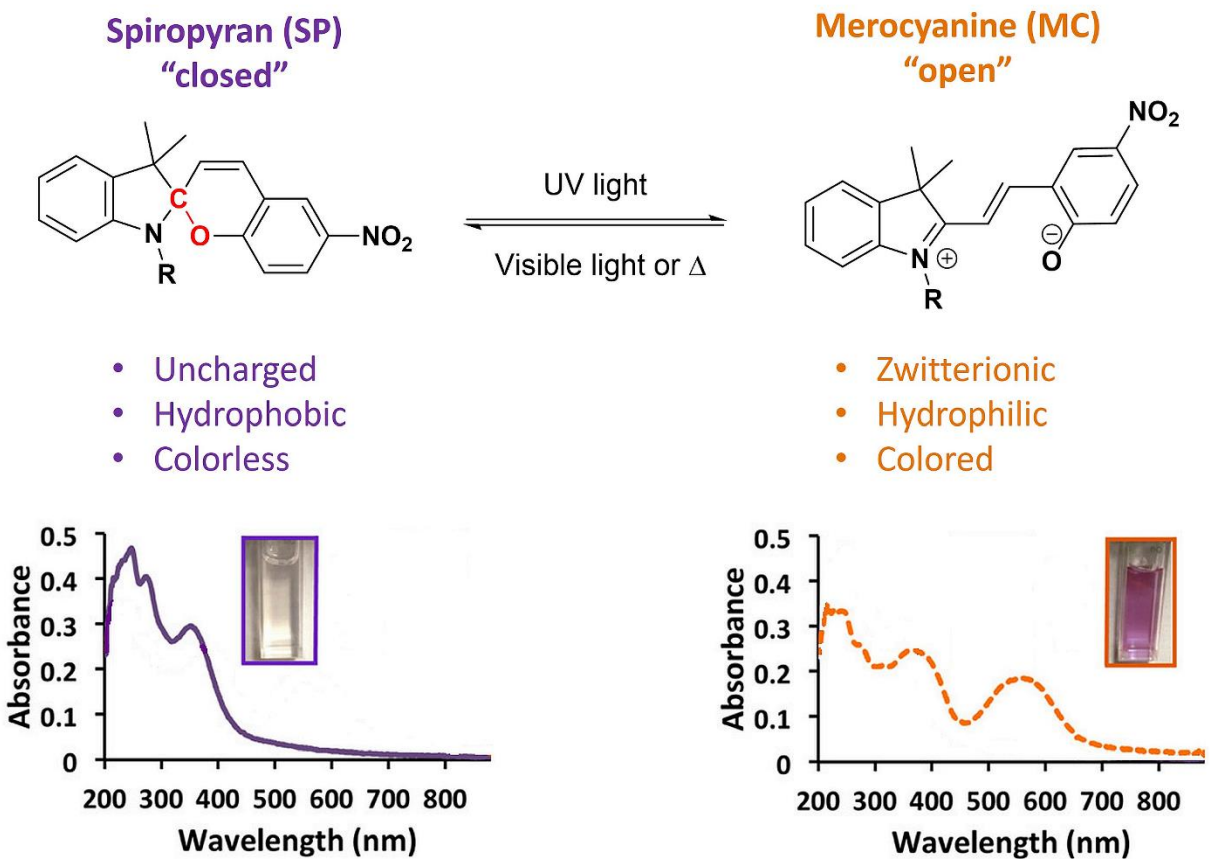

Figure 1.1. *"Closed" spiropyran conversion to "open" merocyanine using UV light irradiation to break the spirocarbon C-O bond (red) and undergo heterolytic cleavage to afford the merocyanine isomer. Reversibility is achieved with visible light or thermal relaxation* (Δ). *The respective chemical properties are detailed below each isomer. Adapted with permission from [*16*]. Copyright 2017 American Chemical Society (ACS)*

1.2 THIS WORK

Understanding the photochromism of spiropyrans lead to their development as molecular switches for light activated motors,[17,18] polymers,[19,20] logic gates,[21,22] etc. Since these advancements, it had been found that spiroyrans respond to several stimuli such as metal ions, anions, pH, and redox chemistry.[23–26] In this dissertation work, we first examine spiropyran as a metal ion sensor, specifically for copper(II) and examine the sensitivity and selectivity for this metal ion. Next, we transition to using spiropyran to sense glutathione to investigate the stereochemistry between these two molecules. Lastly, two spiropyrans are selected based on their sensitivity and selectivity for glutathione to construct an activatable contrast agent for MRI. In each chapter, a background and summary of the relevant sensors are reviewed, followed by results, materials, and methods, and ending with a conclusion.

CHAPTER 2: EMPLOYMENT OF SPIROPYRAN AS A COPPER(II) SENSOR

The work described in this chapter has been reported in:

Trevino, K. M.; Tautges, B. K.; Kapre, R.; Franco Jr, F. C.; Or, V. W.; Balmond, E. I.; Shaw, J. T.; Garcia, J.; Louie, A. Y. Highly Sensitive and Selective Spiropyran-Based Sensor for Copper(II) Quantification. *ACS Omega* **2021**, 6 (16), 10776–10789. https://doi.org/10.1021/acsomega.1c00392.

Adapted with permission from American Chemical Society (ACS)

Trevino, K. M.; Wagner, C. R.; Tamura, E. K.; Garcia, J.; Louie, A. Y. Small Molecule Sensors for the Colorimetric Detection of Copper(II): A Review of the Literature from 2010 to 2022. *Dyes Pigm.* **2022**, 214, 110881. https://doi.org/10.1016/j.dyepig.2022.110881.

Adapted with permission from Elsevier

2.1 SMALL MOLECULE COPPER(II) SENSORS AND THEIR USE FOR COLORIMETRIC DETECTION

2.1.1 IMPORTANCE OF COPPER(II) AND COPPER(II) SENSING

Transition metals are essential for many biological functions, including catalysis, metabolism, and signaling.[27,28] The transition metals that are recognized as being critical to biology include iron, zinc, manganese, cobalt, nickel, molybdenum, and copper; physiological imbalances in these metals can lead to several distinct health problems.[29,30] Copper is a first-row transition metal and an essential trace mineral that plays key roles in physiological functions, such as serving as a cofactor for many enzymes involved in energy production and metabolism.[31] As a cofactor for 30 enzymes, copper plays an important role in biological processes such catecholamine biosynthesis, ATP production, and protecting the cell from oxygen free radicals.[32,33] Bioavailable copper exists as Cu(I) and Cu(II) in physiological conditions, while Cu(II) is the most stable and is highly redox active, which gives it utility as an antioxidant.[34] However, perturbations in copper(II) homeostasis can be highly toxic to cells and has been linked to the development of neurodegenerative diseases such as Alzheimer's,[35–37] Parkinson's,[38,39] Menkes,[40,41] and amyotrophic lateral sclerosis (ALS).[42,43]

In addition to its role in disease, copper(II) can be an undesirable contaminant in the environment and contamination of soil and waterways can occur from agricultural sources, where copper is found in pesticides and fertilizers, and from industrial sources, such as mining and manufacturing operations.[44] The World Health Organization (WHO) has determined the maximum acceptable level of copper in drinking water to be 2 mg/L (31.5 μM) [45] and the Environmental Protection Agency (EPA) sets the threshold at 1.3 mg/L (20.5 μM).[46] Due to the potential health

risks of environmental copper contamination, there is great interest in methods for the analytical detection of Cu^{2+} ions, particularly for use in field applications.

2.1.2 CURRENT METHODS FOR DETECTING COPPER(II)

Current methods for copper quantification include inductively coupled plasma mass spectrometry (ICP-MS),[47–49] atomic absorption spectroscopy (AAS),[50,51] organic colorimetric sensors,[52–54] and fluorescent sensors.[55,56] Analytical methods such as ICP-MS and AAS offer parts per billion sensitivity, but these methods often require protracted sample extraction, preparation, and the use of sophisticated instruments, precluding use for rapid or in-the-field analysis.[47–51] Fluorescent sensors can provide detection of copper ions without protracted sample preparations, but still require advanced instrumentation to analyze the changes in fluorescence.[55,56] Optical, colorimetric sensors for copper offer the potential for naked eye detection of copper ions without extensive sample manipulation or the use of large instrumentation[52–54] and represent a low-cost, rapid alternative to laboratory testing methods. Furthermore, the development of inexpensive portable UV-vis spectrometry instruments means that highly quantitative sub-micromolar readings could one day be taken directly in the field.[57] This would be particularly useful for the rapid detection and quantification of potentially harmful levels of copper through field testing.

2.1.3 CURRENT COPPER(II) SENSORS

Several colorimetric and fluorescent sensors with structures ranging from small molecules,[58–61] large macrocycles,[62–66] and nanoparticle/quantum dots,[67–73] have been recorded. The strong interest in copper sensors is highlighted by a recent PubMed search for “colorimetric

copper sensor", which revealed a steady increase in the numbers of copper sensors reported from 2007-2019 (decreasing number of reports from 2020-21 were likely due to work disruption during the 2020 COVID pandemic) (Figure 2.1). To date, most reviews on copper(II) sensors report fluorescent sensors for copper(II).[74–79] Other reviews discuss colorimetric and fluorescent copper(II) sensors in a range of sizes such as small molecules, enzymes, polymers and nanoparticles[80,81] or organize by the type of optical emission produced (colorimetric, fluorescent, luminescent, chemiluminescent, photoluminescent, surface plasmon resonance) from these copper(II) sensors.[82] However, there have been fewer reviews addressing small molecules for the colorimetric detection of copper(II).[83–85] Further reviews on colorimetric sensing of metals have broadly focused on a number of metals.[86–89]

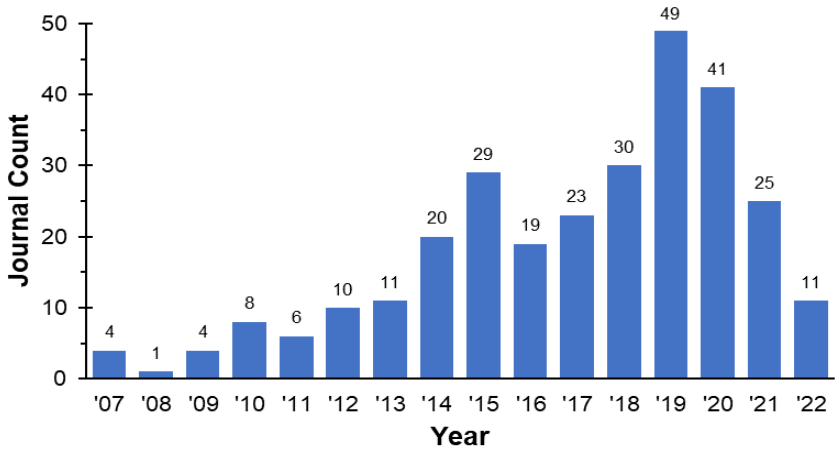

Figure. 2.1. *PubMed search of "colorimetric copper sensor" resulting in the depiction of published copper sensors over the years 2007-2022.*

Small molecule copper ion sensors that produce optical signals are of great interest and we have identified 102 small molecule copper(II) sensors that offer a colorimetric response in solution, with naked eye detection, published in the years 2010-2022. In our review article,[90]

copper(II) sensors were arranged from lowest to highest limit of detection determined by fluorescence or absorbance spectroscopy. Sensors that possessed naked-eye detection but did not report a LOD were included at the end of the review. The extracted data was organized into twelve tables that provided information such as chemical structure of the sensor, the proposed mechanism of Cu^{2+} coordination, additional cations and anions detected by the sensor, K_a = association constant, binding stoichiometry (sensor: Cu^{2+}), concentration of sensor and Cu^{2+} for naked eye detection, the Cu^{2+} selectivity assay conditions including concentration of sensor, Cu^{2+} and competing metal ions tested and solvent conditions. Some sensor designs that were explored included chemosensors incorporating rhodamines,[91–100] Schiff-base units,[101–110] sulfide groups,[111–120] and spiropyrans.[121–128]

Upon evaluation of the copper(II) sensors, metals such as Fe^{3+}, Fe^{2+}, Pb^{2+}, Hg^{2+}, and Co^{2+} were commonly found to offer dual detection. According to the hard-soft acid-base (HSAB) theory, metals are classified as either hard acids (small ionic radii with a high positive charge) or soft acids (large ionic radii with a low positive charge). Utilizing Pearson's absolute hardness values ranging from 3.4-45.8, where the lower the value reflects the softer metal, hardness values for these metal ions were 7.3 (Fe^{2+}), 7.7 (Hg^{2+}), 8.3 (Cu^{2+}), 8.5 (Pb^{2+}), and 13.1 (Fe^{3+}).[129] Co^{2+} was not listed but is considered borderline, displaying intermediate characteristics.[130] Since Cu^{2+} is considered a borderline soft acid, it is reasonable to suggest interference from Fe^{2+}, Pb^{2+}, Hg^{2+}, and Co^{2+} are due to HSAB theory. Although Fe^{3+} is regarded as a hard acid, it is plausible that HSAB does not apply in this case. Recognition of Fe^{3+} was primarily in the form of fluorescence "turn-on" detection. Interestingly, all sensors utilized a Schiff-base unit in the sensing mechanism. It is well known that various metal ions preferentially bind a Schiff-base imine due to the non-bonded electrons on nitrogen in the C=N unit.[131–133] Depending on several factors such as pH,

coordinating ability of the counter anions, the amine or aldehyde fragment regenerated, etc.[134–137], two possible mechanisms could explain this phenomenon. (1) Coordination of Fe^{3+} in the binding pocket containing a Schiff-base unit induces hydrolytic cleavage of the C=N and formation of an amine and carbonyl. This results in partial decomposition of the sensor and generation of a fluorophore enabling fluorescent enhancement. (2) The second possible sensing mechanism involves the coordination of Fe^{3+} in the binding pocket containing a Schiff-base unit but instead of undergoing hydrolysis, the Fe^{3+}-sensor complex is stabilized by the donation of the electrons from nitrogen on C=N imine. Upon emission of this complex, PET is inhibited due to the Fe^{3+}-sensor stabilization, allowing for full relaxation of the electrons back to the ground state, resulting in fluorescence. As for Cu^{2+}, it has been often used as a fluorescent "turn-off" sensor due to its paramagnetism.[58,97,105,106,138–143] Upon emission of a Cu^{2+}-fluorophore complex, PET is possible when an excited electron relaxes to the dx^2-y^2 orbital, resulting in fluorescence quenching.[75,76,85]

Common anions that interfered with copper sensing, and offered dual detection, were S^{2-}, CN^-, and F^-. Further expanding on HSAB theory, hard acids preferentially react with hard bases and analogously, soft acids preferentially react with soft bases. Therefore, the HSAB theory could account for interference by sulfur and cyanide acting as soft bases. The high affinity of copper(II) for these ligands can displace the metal from the sensor to form CuS or $Cu(CN)_2$. Since fluoride is considered a hard base, the possible mechanism for detection of F^- could be due to its electronegativity and high propensity to intermolecular hydrogen bond. Of the sensors that detected F^-, this is particularly seen with hydrogens covalently bound to either an amine or phenol. The lone pair electrons on nitrogen and oxygen induce a dipole creating a partial positive charge on hydrogen, making it susceptible to intermolecular hydrogen bonding with fluoride.

Overall, the ideal copper(II) sensor used for in-field analysis would be able to detect copper only, even in the presence of competing metal ions, and be able to do so in a 100% aqueous medium, whether it be free in solution or fixed to a test strip. Another important feature in developing an in-field sensor for detecting Cu^{2+} contamination in soil and water is the ability of the sensor to be applied to aqueous solutions. A common workaround to adapt a sensor that was soluble in an organic or mixed-organic solvent, was to fix them to paper and make test strips. This is a practical option as long as competition studies are performed to confirm that Cu^{2+} selectivity remains. However, this was not fulfilled in the papers discussing paper-based copper sensors that were reviewed. Interference studies, especially with excess competing metal ions and solubility in water, should be a priority that is addressed for future advancement of sensors being developed for copper(II) detection.

2.2 HIGHLY SENSITIVE AND SELECTIVE SPIROPYRAN-BASED SENSOR FOR COPPER(II) QUANTIFICATION

2.2.1 SP-14 AS A COPPER(II) SENSOR

Spiropyrans are of interest due to their switchable nature from closed spiropyran (hydrophobic & nonionic) to open merocyanine (hydrophilic & zwitterionic) and because of this their derivatives have been utilized for the detection of copper(II) ions.[121–128] However, most of these sensors suffer from low sensitivity for naked eye detection with the concentration of Cu^{2+} detection ranging primarily from 20 µM – 2 mM,[121–127] which can be above critical thresholds of interest, such as in environmental contamination. Of the spiropyran-based copper sensors previously referenced, only one demonstrated naked-eye detection below 10 µM for the

spiropyran-copper(II) complex.[128] However, the color change is inconsistent, going from pinkish-violet in the absence of copper, to violet at 1 μM, to blue at 10 μM. The distinct color change from purple to blue is proposed to be due to copper(II) metal ligation to the naphthanolate and the hydroxyl group, but mechanistic studies were not performed. In addition, competitive binding experiments were performed with the sensor (10 μM) to Cu^{2+} (10 μM), mixed with other metal ions (50 μM) via UV-Vis spectrometer, however, naked-eye detection under these conditions was not reported. It is evident that while there have been many copper sensor designs, sensitivity and selectivity for naked-eye detection remain elusive. For example, of the 102 sensors mentioned above, only 15 sensors displayed naked-eye detection below 10 μM.[95,100,109,114,120,128,139,144–151] Furthermore, only 6 out of the 15 sensors challenged copper sensing in the presence of a competing metal ion[109,128,145–147,149] and 2 challenged copper sensing in the presence of ten-fold excess competing metal to copper,[147,149] which is achieved in this work.

In our published article[152] we synthesized a dimethylamine-functionalized spiropyran, **SP-14**, sensor for copper(II) detection. **SP-14** was able to achieve naked-eye detection down to ≈ 6 μM and a limit of detection of 0.11 μM, showing promise for in-the-field applications. We found that placing an electron-donating group on the indoline portion of a spiropyran yielded an enhanced metal ion response for optical detection. With this information, we developed a methoxy-functionalized spiropyran with a pendant dimethyl amine on the chromene portion in an effort to enhance sensitivity while maintaining high copper(II) selectivity (Figure 2.2). Herein, we examine the metal sensitivity and selectivity of this derivative for copper(II) ions.

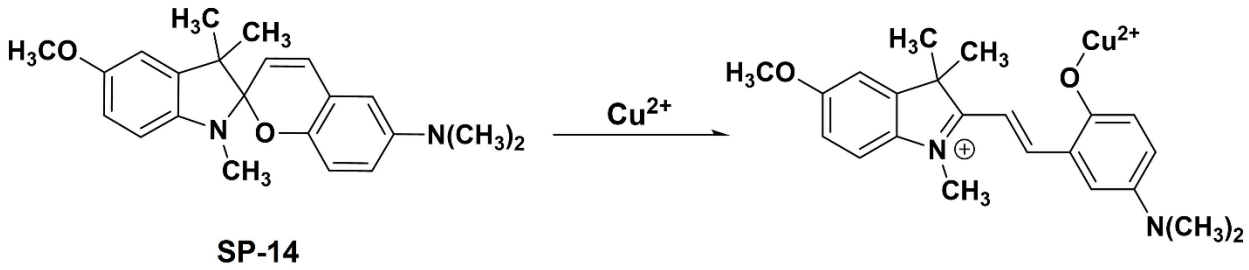

Figure 2.2. *Generalized isomerization of* ***SP-14*** *in the presence of* Cu^{2+}.

*2.2.2 SYNTHESIS OF **SP-14***

The synthesis of this spiropyran derivative has previously been reported.[153] Briefly, the synthesis of **SP-14** proceeded conveniently through the convergent synthesis of the appropriate indolium iodide and dimethylaminobenzaldehyde (Scheme 2.1). The indolium iodide was prepared from the methoxyhydrazine through an interrupted Fisher indole synthesis, followed by methylation with iodomethane. The one-pot reduction and methylation of 2-hydroxy-5-nitrobenzaldehyde with palladium on carbon, formaldehyde, and hydrogen afforded the requisite 5-dimethylamino-2-hydroxybenzaldehyde. Subsequent condensation of the indolium iodide with 5-dimethylamino-2-hydroxybenzaldehyde, in the presence of Et_3N, afforded **SP-14**.

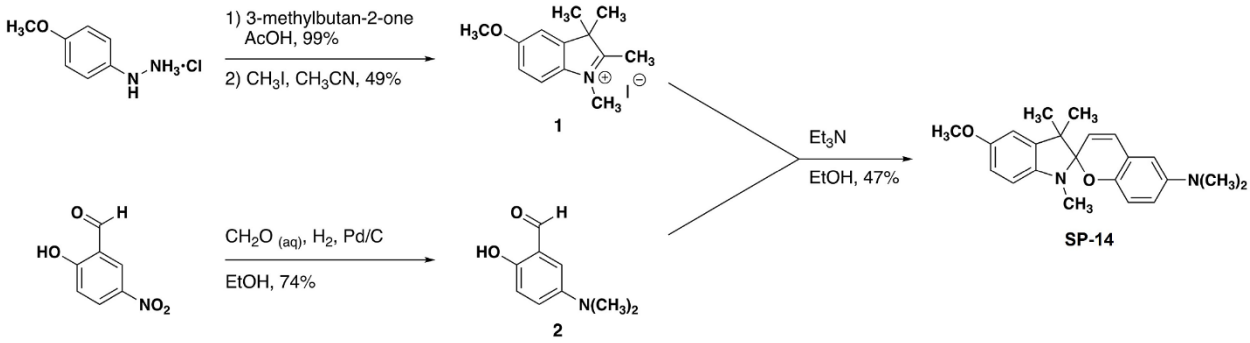

Scheme 2.1. *Synthesis of* ***SP-14.***

2.2.3 Response to light and reference compounds (phenol and N,N-dimethylaniline)

In an effort to evaluate the relative photochromism of **SP-14**, the absorption profile was compared before and after irradiation with UV light. Figure 2.3A shows the absorption spectral changes of **SP-14** after UV irradiation. Prior to UV exposure, the absorption plot of **SP-14** is characterized by large absorbance bands at 250 and 312 nm corresponding to the ring-closed spiro (SP) form (Figure 2.3A, solid line). No significant absorption was found in the visible region, which suggests that most of **SP-14** was present in its spiro form. It was postulated that the electron-donating character of the amine substituent on chromene suppresses spiro-to-mero conversion.[125] Upon irradiation with UV light, a modest increase in absorbance (0.04 A.U.) at 483 nm, corresponding to the ring-open mero (MC) form, was observed (Figure 2.3A, dotted line). While the UV-vis spectrum suggested that the absorption properties of **SP-14** were minimally influenced by UV light, addition of one equivalent of Cu^{2+} to a solution of **SP-14** in ethanol with a 15 min incubation period produced a green solution with strong mero absorption bands centered at 418 and 677 nm. A hypsochromic shift of the mero lambda max from 483 to 418 nm (Figure 2.3B) was observed, which could be attributed to the change in the local environment such as an increase in the ionic strength due to the added copper(II) salt in the solution. The strong absorption band at 677 nm was assigned to possible **SP-14**–Cu^{2+} complex in solution; this bathochromic shift of the mero band from 483 to 677 nm was consistent to reported absorbance changes accompanying the formation of MC–Cu^{2+} complex exhibited by quinaldine-indole-based spiropyran.[123] Copper(II) is an intermediate hard Lewis acid and therefore is hypothesized to preferentially interact with hard Lewis bases such as dimethylamino and phenolic oxygen groups on chromene, forming MC–Cu^{2+} adducts.

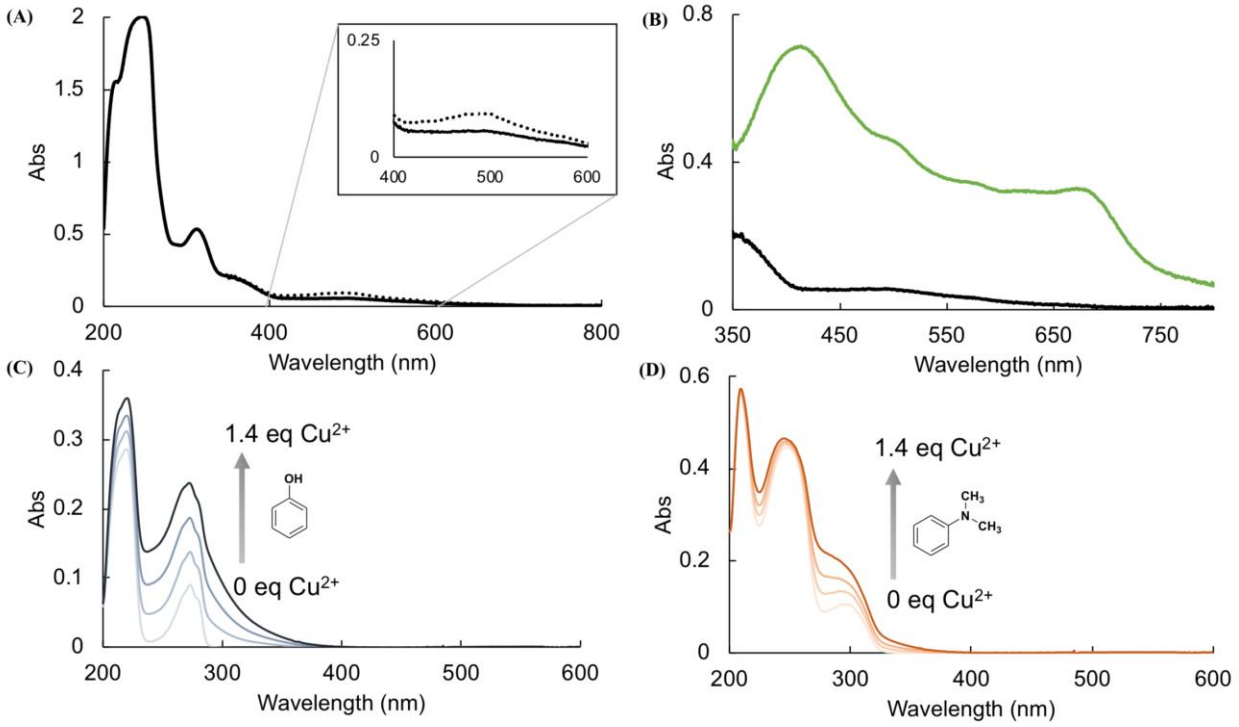

Figure 2.3. *(A) Absorbance profile of* ***SP-14*** *(100 μM in ethanol) after preparation in the dark (black, solid) and after 15 min UV irradiation at 302 nm with an 8-Watt UV source (black, dotted). Inset shows the modest increase (0.04 A.U.) in response to UV irradiation indicating minor photoswitching for* ***SP-14****. (B) Absorbance profile of* ***SP-14*** *in the absence (black) and presence (green) of* Cu^{2+}*. Response of reference compounds (100 μM): (C) phenol and (D) N,N-dimethylaniline to varying amounts (0–1.4 eq) of* Cu^{2+} *in ethanol.*

To test the hypothesis of copper(II) binding to phenolic and/or dimethyl amine groups on chromene, we investigated the changes in the UV-vis profile of the reference compounds: phenol and *N*,*N*-dimethylaniline upon addition of copper(II) in ethanol (Figure 2.3C and 2.3D). In the presence of copper(II), significant increases in absorbance were observed in the 250–375 nm range for both molecules. The absorbance in this wavelength range continually increased as more copper(II) ions were introduced. These copper(II)-induced changes in UV-vis profile indicate that

the methylated amine and phenolic oxygen in **SP-14** are capable of interacting with copper(II). Theoretical calculations of copper interactions with **SP-14** yielded *TTT* being the most stable ring-open merocyanine isomer (Figure 2.3A). Several minima including binding of copper to the phenolic oxygen or the dimethyl amine concluded that binding to phenolic oxygen was the lowest energy, and most stable option (Figure 2.3B). This binding is illustrated in Figure 2.4. Also, this UV-vis data underscores the importance of the amine substituent for copper(II) sensing as the electron-donating character of the former is expected to stabilize the spiro form of **SP-14** forming a photostationary spiropyran state.[154] Upon coordinately binding to copper(II) ion, the electron donating character of the methylated amine decreases, consequently favoring spiro-to-merocyanine conversion as illustrated by the appearance of strong merocyanine bands in the visible region in Figure 2.3B.

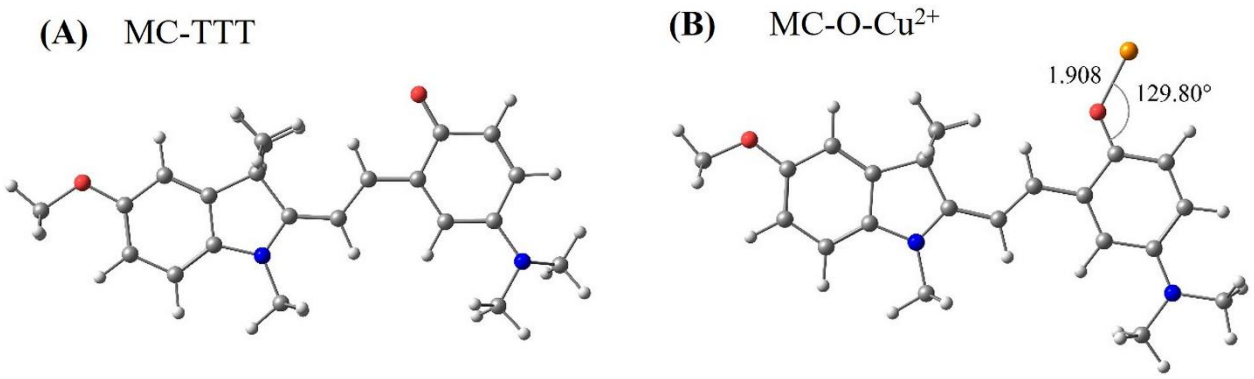

Figure 2.4. *DFT calculations performed to determine (A) the TTT isomer to be the most stable ring-open merocyanine form and (B) the phenolic oxygen (red) to be the strongest interaction between* ***SP1*** *and* Cu^{2+} *(orange). Nitrogen atom represented as blue. DFT calculations were performed by Francisco Franco from the Chemistry Department of De La Salle University, Manila Philippines.*

2.2.4 SENSITIVITY TO COPPER(II)

The sensitivity of **SP-14** for copper(II) ion was evaluated by colorimetric and titration studies with concentrations of copper(II) varying from 0 to 200 μM. The distinct visual color change of **SP-14** allows qualitative differentiation among different concentrations of copper(II) ions present (Figure 2.5A). Without copper(II) present, the solution of **SP-14** is light pink in color; however, after incubating with 25 μM of copper(II) for 15 min, the color of the **SP-14** solution changed to green. This green color became progressively darker as the copper(II) concentration was increased from 25 to 175 μM of copper(II), which could allow a field user to employ **SP-14** much like a pH strip to roughly quantify the copper(II) concentration. To validate this concentration-dependent darkening of green color, absorption profile of **SP-14** was monitored as aliquots of copper(II) chloride were added to the solution of **SP-14**. Significant increase in the absorbance of **SP-14** at 418 and 677 nm was evident with increasing concentration of copper(II) ion (Figure 2.5A inset). To resolve that copper(II) chloride alone was not inducing the green color, concentrations ranging from 0 – 175 μM copper(II) chloride in ethanol were evaluated (Figure 2.5B). No visual color was observed for copper(II) chloride at these concentrations (Figure 2.5B inset). In addition, the absorbance profile of copper(II) chloride displayed no absorbance peaks at 418 nm or 677 nm, further indicating the **SP-14**-Cu^{2+} interaction prompts the color change.

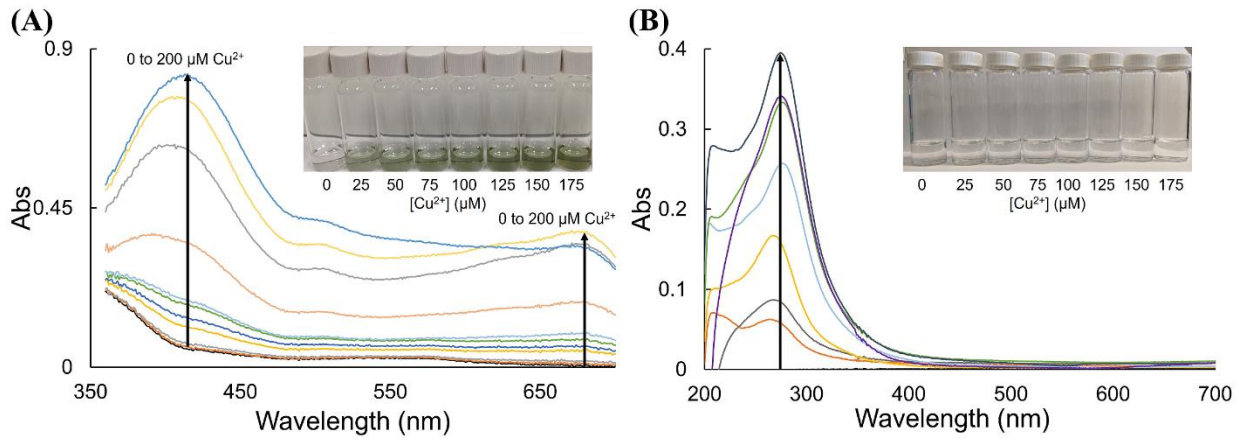

Figure 2.5. *(A) Absorbance profile of **SP-14** incubated with various concentrations of Cu^{2+}: 1 μM (orange); 2 μM (grey); 4 μM (gold); 6 μM (blue); 8 μM (green); 10 μM (light blue); 25 μM (light orange); 50 μM (light grey); 100 μM (yellow); and 200 μM (blue). 5A inset: Color change observed for **SP-14** with increasing concentrations of copper(II). An observable change in color between concentrations suggests **SP-14** is capable of being used in the field for naked eye qualitative assessment of copper(II) concentration. (B) Absorbance profile of copper(II) chloride (0 – 175 μM) in ethanol. Cu^{2+}: 0 μM (black); 25 μM (orange); 50 μM (grey); 75 μM (yellow); 100 μM (light blue); 125 μM (green); 150 μM (purple); 175 μM (dark blue). An increase in absorbance at λ_{max} =274 nm was observed. 5B inset: No observable change in color for copper(II) chloride with increasing concentrations from 0 – 175 μM suggest Cu^{2+} alone does not produce the green color.*

The linearity of **SP-14** and copper(II) interaction was also assessed and it was found that the absorbance increase was linear from 0 to 20 μM of copper(II) (inset, Figure 2.6A) with no increase in absorbance seen at 677 nm after one equivalent of copper(II) had been surpassed, suggesting possible 1:1 copper(II)–ligand stoichiometry (Figure 2.6A). The 1:1 stoichiometry

paired with the observations above for binding of copper(II) to reference compounds bearing either amine or phenolic oxygen moieties rules out the possibility of two different copper(II) ions binding simultaneously to dimethylamine *N* and phenolic *O*.

The stoichiometry of **SP1** and copper(II) was validated by Job's method, is a widely used analytical technique to determine the stoichiometry of a binding event. This method keeps the total molar concentration of two binding components constant, while varying the molar fraction of one binding component. In this study, the molar fraction of copper(II) was varied from 0 to 0.9 while keeping the sum of the initial concentration of **SP1** and copper(II) ion at 100 µM. The absorbance for each molar fraction of copper(II) was recorded at 677 nm and was plotted against the molar fraction of copper(II) ion as shown in Figure 3D. The maximum absorbance was achieved at a molar fraction of 0.5, indicating a 1:1 stoichiometry of the **SP1** and copper(II) ion. This stoichiometry is consistent with previous spiropyran-based colorimetric metal sensors, which often exhibited a 2:1 or 1:1 ligand–copper(II) stoichiometry.[154,155]

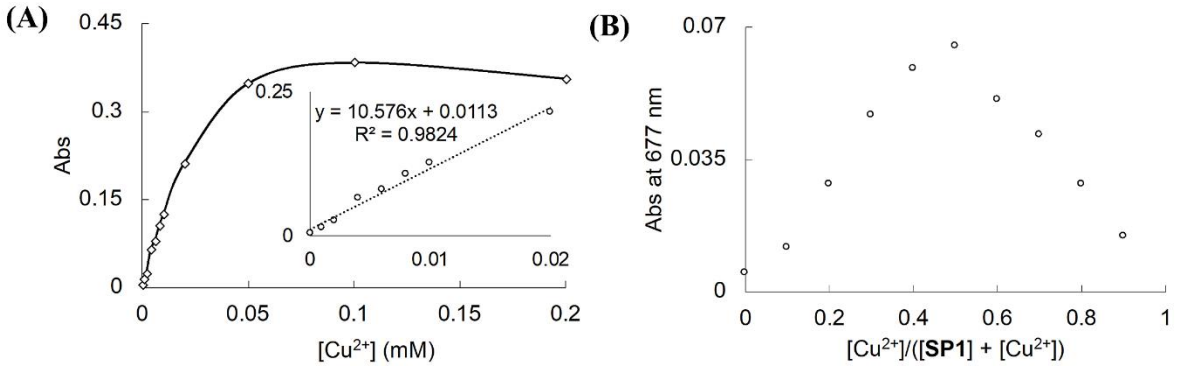

Figure 2.6. *(A)* ***SP-14*** *titrated with various concentrations of copper(II) with the absorbance measured at 677 nm. This titration study demonstrates a nearly linear response through 20 µM* Cu^{2+}*, indicating the utility of* ***SP-14*** *as a quantitative sensor for copper through 50 µM concentrations of copper(II). Inset shows the linearity of response from 0 to 20 µM. (B) Job's*

*analysis of **SP-14**–Cu^{2+} complex in ethanol. Absorbance recorded at 677 nm with maximal absorbance achieved at 0.5 molar fraction of copper(II) indicating a stoichiometry of 1:1 for the **SP-14**–Cu^{2+} complex.*

To determine the limit of detection (LOD) for copper(II) detection using **SP-14**, the change in absorption was plotted against the [Cu^{2+}] concentration. The detection limit of 0.11 μM by means of UV-Vis spectrometry, was determined by calculating the [Cu^{2+}] at 3SD (SD estimated using the root MSE of 0.0022) above the estimated intercept (0.0070) of the linear regression (Figure 2.7A). Compared to other spiropyran-based colorimetric copper(II) sensors, **SP-14** exhibited the second lowest limit of detection relative to other spiropyran-based colorimetric copper(II) sensors previously mentioned.[121–128] It is interesting to note the minor structural variations that contribute to the varying limits of detection. Amine placement and other electron donating groups on the indole may provide greater enhancement of this observed sensitivity and will be the focus of future studies.

The sensitivity of **SP-14** was further investigated at micromolar levels (0 – 10 μM of Cu^{2+} in D.I.U.F water) by subsequently varying copper(II) concentration to a solution of **SP-14** and monitoring the color change over a 15 min period. Figure 2.7B illustrates that, through naked eye detection, **SP-14** permits discrimination of ≈ 6 μM concentration of copper(II) over the control and can accurately quantify micromolar concentrations of copper(II). These results support the use of **SP-14** at concentrations well below physiological copper(II) ion concentrations (16 μM in serum, 300 μM in cells).[156]

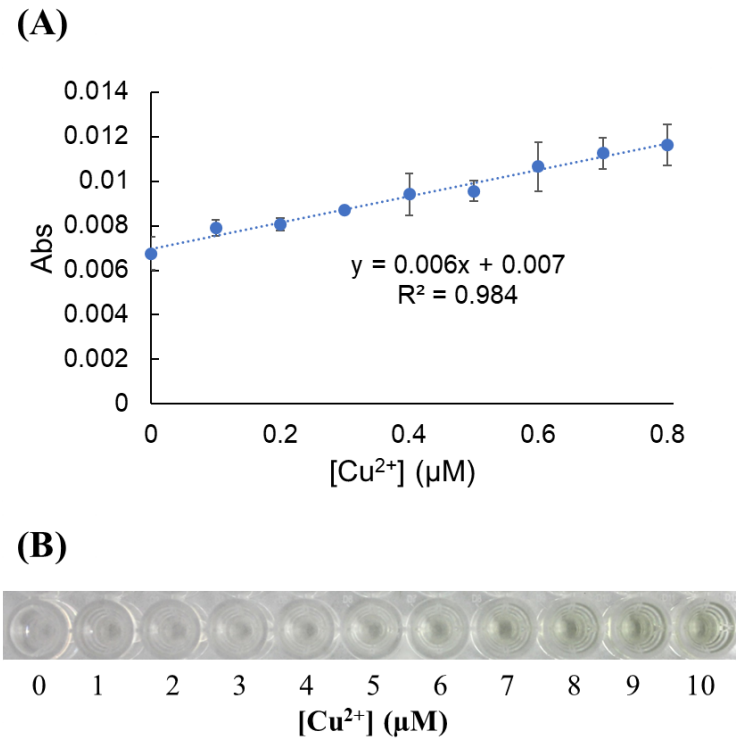

Figure 2.7. *(A) LOD curve for* ***SP-14*** *incubated with copper (II) concentrations ranging from 0 – 0.8 μM. The LOD was found to be 0.11 μM (B) Naked eye detection of* ***SP-14*** *incubated with increasing concentrations of copper(II) chloride, depicts visual identification of copper(II) ≈ 6 μM.*

2.2.5 SELECTIVITY TO COPPER(II)

Because of the promising sensitivity of **SP-14** towards copper(II), we also studied selectivity by monitoring the changes in the UV-visible absorption profile of **SP-14** in response to chloride salts of other biologically and environmentally relevant metals such as Na^{+}, K^{+}, Mn^{2+}, Ca^{2+}, Zn^{2+}, Co^{2+}, Mg^{2+}, Ni^{2+}, Fe^{3+}, Cd^{2+}, and Pb^{2+} in equimolar concentration. Selectivity of some sensors towards copper(II) over other metal ions has been attributed to the strong affinity of copper(II) ion toward N,O-chelate ligands and the fast metal-to-ligand binding kinetics of copper(II) to its ligand.[154] Thus, we hypothesize that the presence of the amine substituent in our

SP-14 ligand could provide copper(II) selectivity over possible confounding alkali, alkaline earth, and transition metal ions. To test this hypothesis, the absorption spectra of **SP-14** were taken after incubation with 1 equivalent of each metal salt (metal stock in D.I.U.F water). The presence of the distinct absorbance band at 677 nm allowed for copper(II) quantification over the other metal ions tested, which exhibited absorbance increases only at 418 nm when incubated with **SP-14** in ethanol (Figure 2.8A, copper = purple line). Metal ion selectivity was also quantified based on the relative absorbance increase of **SP-14** at 677 nm when incubated with one equivalent of various metals (Figure 2.8B). Absorbance data showed **SP-14** exhibiting a nearly 21-fold increase over the baseline when incubated with copper(II), which is almost six-fold greater change in absorbance at 677 nm compared to the next best metal ion, Fe^{3+} ($p<0.0010$, Welch's 2 sample t-test). Interestingly, copper is the only metal tested to exhibit a green solution with **SP-14**; other metals produced pink to reddish brown color (Figure 2.8B, inset).

The binding specificity of **SP-14** for copper(II) was further characterized by competition studies where the absorbance of **SP-14** with 1 equivalent of a competitive metal ion was determined in the presence and absence of 1 equivalent of Cu^{2+} at 418 and 677 nm. At 418 nm, other metal ions such as Mn^{2+}, Ca^{2+}, Zn^{2+}, Co^{2+}, Mg^{2+}, Ni^{2+}, Pb^{2+}, and Fe^{3+} induced significant absorbance changes (Figure 2.8A and 2.8C), and therefore could confound analysis of copper(II) levels if measurements were done at this wavelength; thus, the sensor should not be used at 418nm. In contrast, Figure 2.8A and 2.8D show that when absorbance was monitored at 677 nm, there was no absorbance at 677 nm for other metals except iron and lead, which showed much lower absorbance than copper. Therefore, 677 nm is recommended for copper sensing. However, there is a diminished response to copper(II) when iron(III) is present, suggesting that iron may interfere with Cu detection.

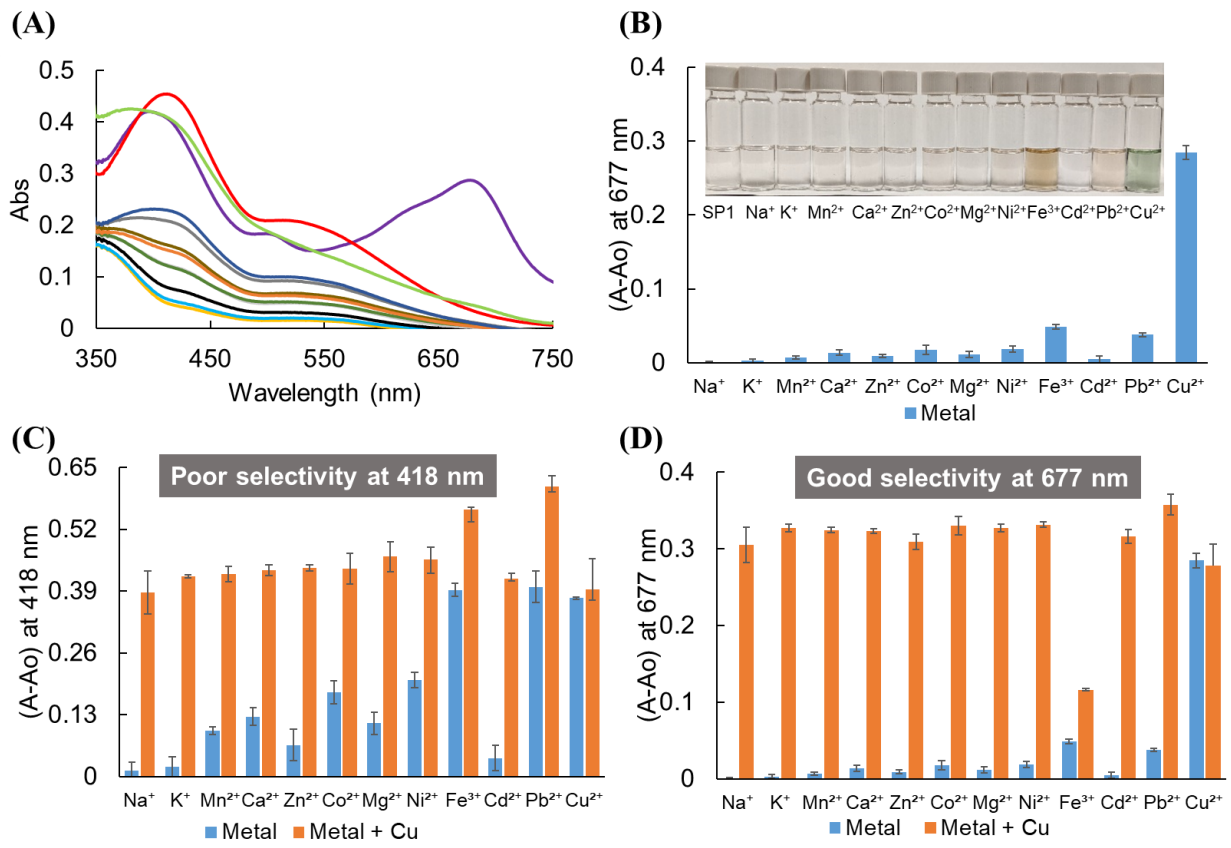

Figure 2.8. *(A) Absorbance profile of* ***SP-14*** *after 15 min incubation with one equivalent of various metal chlorides: Cu^{2+} (purple), Fe^{3+} (red), Ni^{2+} (dark blue), Mg^{2+} (orange), Co^{2+} (grey), Zn^{2+} (green), Ca^{2+} (brown), Mn^{2+} (light grey), K^{+} (light blue), Na^{+} (yellow), Cd^{2+} (black) and Pb^{2+} (light green). (B) Relative absorbance increases at 677 nm of* ***SP-14*** *incubated for 15 min with one equivalent of various metals. Blue bars represent the change in absorbance versus initial absorbance to give the relative absorbance increases at 677 nm. (C) Competitive binding experiment of with one equivalent of copper(II) in the presence of one equivalent of competing metal ions monitored at (C) 418 and (D) 677 nm. Blue bars represent the change in absorbance when* ***SP-1*** *is incubated with one equivalent of only one metal ion. Orange bars represent change in absorbance for* ***SP-14*** *when incubated with one equivalent copper(II) and one equivalent of a competing metal ion. The orange bars demonstrate that the response of* ***SP-14*** *to copper(II) is*

unaffected by the presence of competing metals. These results verify that ***SP-14*** *can be used to detect copper(II) reliably regardless of the other metal ions present in solution. Error bars represent standard deviation of three trials.*

The absorbance profile for each metal chloride at 1 x 10^{-4} M in ethanol was also evaluated (Figure 2.9). Metal ions Fe^{3+} and Pb^{2+} contained some absorbance at 418 nm, which could explain the relatively higher absorbance compared to the other metal ions with and without Cu^{2+}. None of the other metal ions displayed an absorbance at 677 nm. These results indicate that quantitative, relatively specific determination of Cu^{2+} levels using **SP-14** would be possible if measurements are done at 677 nm. This wavelength-dependent copper (II) selectivity by **SP-14** could be particularly useful, for example, when samples contain high concentration of other ions such as Mn^{2+} and K^{+}, two of the common ions found in soil.

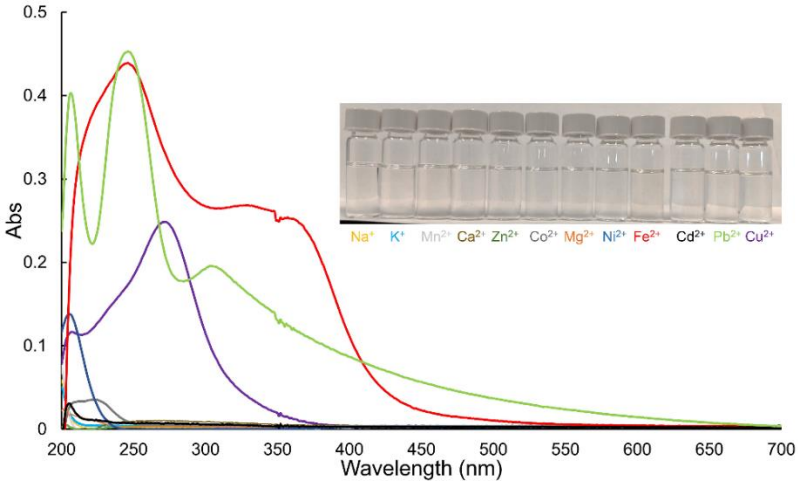

Figure 2.9*. Absorbance profile and corresponding picture (inset) of 1 × 10^{-4} M solution of metal chlorides in ethanol. Cu^{2+} (purple), Fe^{3+} (red), Ni^{2+} (dark blue), Mg^{2+} (orange), Co^{2+} (grey), Zn^{2+} (green), Ca^{2+} (brown), Mn^{2+} (light grey), K^{+} (light blue), Na^{+} (yellow), Cd^{2+} (black) and Pb^{2+} (light green).*

To further test the detection capability of **SP-14** for copper (II), the competition study was repeated at higher concentrations of competing metal, and the absorbance of **SP-14** was evaluated at 418 and 677 nm with 10 equivalents of a competitive metal ion in the presence and absence of 1 equivalent of Cu^{2+} (Figure 2.10). **SP-14** incubated with and without one equivalent of copper(II) was used as the control. Analysis done at 418 nm with **SP-14** in the presence of 10 equivalents of the metal displayed that all ions except Na^{+} and K^{+}, induced an increase in absorbance at that wavelength (Figure 2.10A). When 1 equivalent of Cu^{2+} was added, it is noted there was an additional increase in absorbance for each metal ion at 418 nm except Pb^{2+}. Due to the significant absorbances of metal ions, such as Mn^{2+}, Ca^{2+}, Zn^{2+}, Mg^{2+}, Ni^{2+} and Cd^{2+}, Co^{2+}, Fe^{3+} and Pb^{2+}, as previously noted, analysis at this wavelength would confound copper(II) detection. Therefore, 677 nm was again inspected (Figure 2.10B). At 677 nm, metal ions Co^{2+}, Fe^{3+}, and Pb^{2+} exhibited some absorbance.

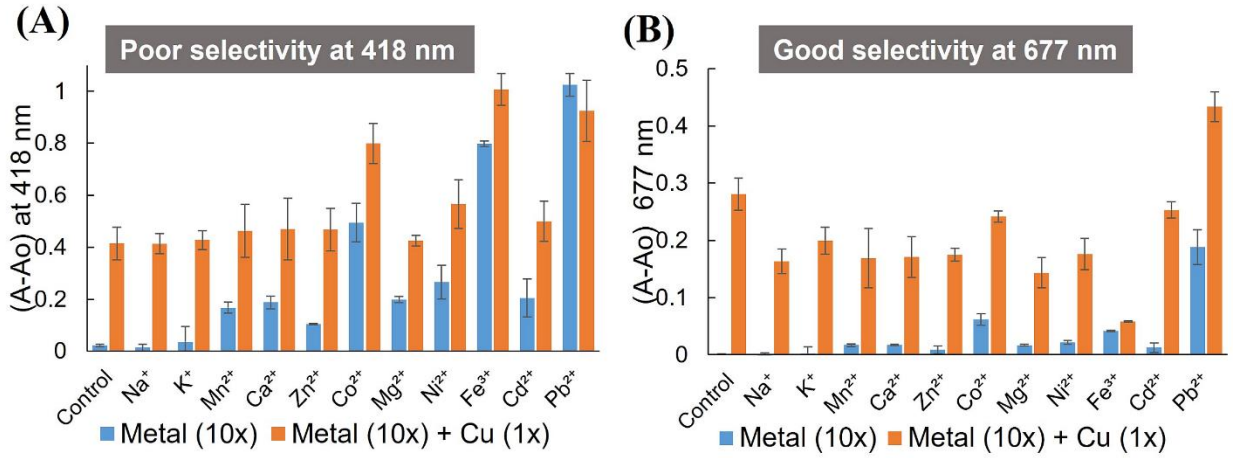

Figure 2.10. *Competitive binding experiment of* ***SP-14*** *with one equivalent of copper(II) chloride in the presence of ten equivalents of competing metal ions monitored at (A) 418 nm and (B) 677 nm. Blue bars represent the change in absorbance when* ***SP-14*** *is incubated with ten equivalents of only one metal ion. Orange bars represent change in absorbance for* ***SP-14*** *when incubated*

with ten equivalents of a competing metal ion and one equivalent of copper(II) chloride. ***SP-14*** *incubated without (blue) and with (orange) one equivalent of copper(II) was used as the control.*

However, when incubated with **SP-14** alone, both Co^{2+} and Pb^{2+} did not display the bathochromic shift associated with **SP-14**-Cu^{2+} complex (Figure 2.11A). Only in the presence of one added equivalent of copper(II), is the strong absorbance band at 677 nm witnessed (Figure 2.11B). Copper can again be detected by eye through a notable change to a greenish solution with the addition of one equivalent of copper, even in the presence of 10x excess competing metals, with the exception of Fe^{3+} and Pb^{2+} (Figure 2.11B inset). As for the 1:1 studies, monitoring the sensor at 677 nm provided optimal selectivity for copper, As expected with Fe^{3+}, there was a diminished response to copper(II), which was previously seen in the equimolar competition studies. At 10x excess, lead also contributes absorption that confounds copper interpretation, but it should be noted that the levels of lead represented by 10X are very high, on the order of lead concentrations in water found during the height of the Flint Michigan crisis.[157] There are several feasible approaches to navigate around these interferences. For example, the establishment of pre-treatment methods, such as a Fe^{3+} chelator that could effectively remove this metal ion from the sample. Singha et al.[158] developed a rhodamine functionalized mesoporous silica to remove Fe^{3+} from solutions. Due to the mesoporous solid support, this material can be effectively removed via filtration. Lead is a contaminant of great health concern and a number of separate sensors for lead have been developed,[159] which could be used to identify lead vs copper contribution. Furthermore, because copper still confers a distinct green color even in the presence of 10x competing metals (Figure 2.11B inset), for all metals except iron and lead, both of which are also undesirable contaminants; a field test with **SP-14** could be used as an initial screening mechanism to determine if samples

contain any of these three undesirable metals and need to be brought back for further lab analysis by other more sensitive methods.

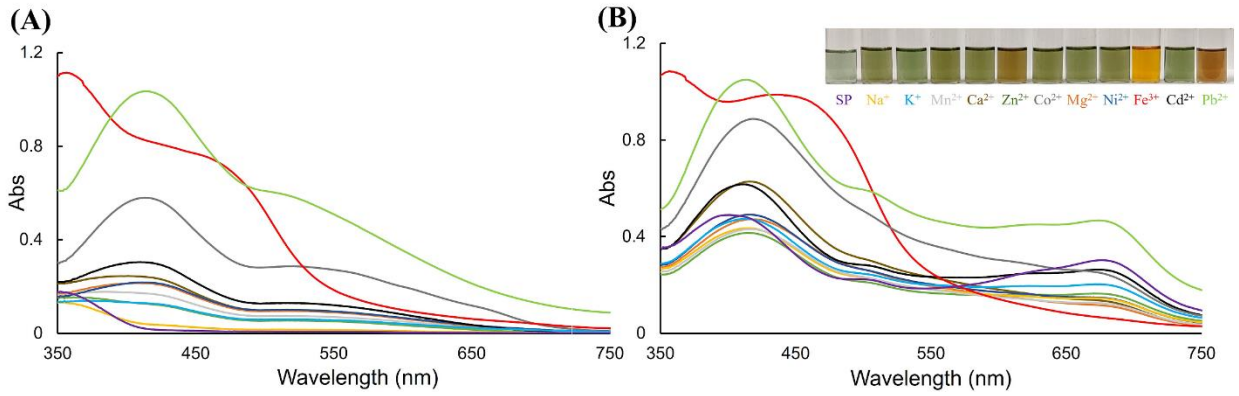

Figure 2.11. *(A) Absorbance profile of* ***SP-14*** *(1.0×10^{-4} M in ethanol) after 15 min incubation with ten equivalents of various metal chlorides. (B) followed by 15 min incubation with one equivalent of copper(II) chloride. Cu^{2+} (purple), Fe^{3+} (red), Ni^{2+} (dark blue), Mg^{2+} (orange), Co^{2+} (grey), Zn^{2+} (green), Ca^{2+} (brown), Mn^{2+} (light grey), K^{+} (light blue), Na^{+} (yellow), Cd^{2+} (black) and Pb^{2+} (light green). Inset: Visual representation of* ***SP-14*** *incubated for 15 min with ten equivalents of metal chlorides (1.4×10^{-2} M solution in water) followed by 15 min incubation with one equivalent of copper(II) chloride (1.4×10^{-2} M solution in water).*

The naked eye, colorimetric, selective detection of copper by **SP-14** is summarized and presented in Figure 2.12A for 1X competing metals and Figure 2.12B for 10X competing metals. These photographs mirror the solutions from the absorbance spectrophotometry studies previously discussed. As shown in Figure 2.12A, the 1X metals alone do not impart color to the solution. **SP-14** with metals at 1X plus are colorless to pink, except for copper(II), which is green. When copper is introduced to **SP-14** in the presence of 1:1 equivalent competing ion, metal: Cu^{2+}, this solution is still green, except for Fe^{3+}, which is brownish green. Figure 2.12B reveals metals alone at 10X,

do not possess any significant color, except for iron which is light yellow. When the **SP-14** sensor is present in the 10X metal solution, all are colorless to light pink except for Fe^{3+} and Pb^{2+}. **SP-14** plus copper in the presence of 10:1 molar equivalent competing metal: Cu^{2+} maintains the green color, except for Fe^{3+}, which is yellow, and Pb^{2+}, which is brown. These results demonstrate the ability of **SP-14** to detect copper even in the presence of excess amounts of other potential contaminating metals.

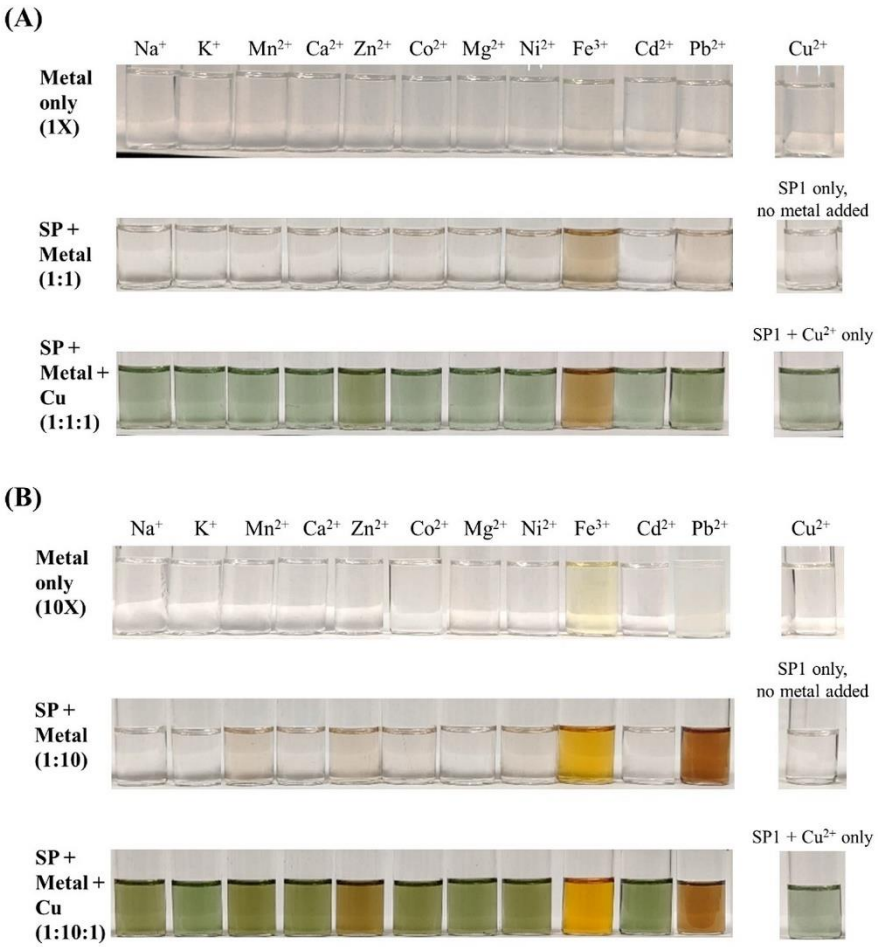

Figure 2.12. *Summary of the naked eye, colorimetric, selective detection of copper(II) by* ***SP-14.*** *Samples are shown in the presence and absence of (A) 1X and (B) 10X competing metals.*

2.3 MATERIALS AND METHODS

2.3.1 MATERIALS

All reagents were purchased from Sigma Aldrich and used without further purification unless stated otherwise. Accurate mass measurements were recorded on positive electrospray ionization (ESI) mode in CH_3OH or CH_3CN on a Thermo Electron LTQ-Orbitrap Hybrid MS (Thermo Fisher Scientific Waltham, MA). ^{1}H and ^{13}C NMR spectra were measured in the solvent stated at 400 or 600 MHz and 101 or 151 MHz, respectively (Bruker AVIIIHD Nanobay 400 MHz and Bruker VNMRS 600 MHz, Bruker LLC, Billerica, MA). UV-vis absorption spectra were recorded in 1.0 cm path length and 700 µL quartz cuvettes on a Cary Bio-100 UV-vis spectrophotometer (Aligent, Santa Clara, CA). All metal salts were prepared in de-ionized ultra-filtered (D.I.U.F) water purchased from Fisher Scientific.

2.3.2 SYNTHESIS AND STRUCTURAL CHARACTERIZATIONS

*5-Methoxy-1,2,3,3-tetramethyl-3H-indol-1-ium iodide (**1**).*[160]

Following a modified literature procedure,[161] a solution containing 3-methylbutan-2-one (5.90 mL, 55.2 mmol) in glacial acetic acid (88 mL) was added 4-methoxyphenylhydrazine hydrochloride (4.815 g, 27.57 mmol). The solution was stirred at reflux for 5.5 h. The solution was allowed to cool to room temperature and neutralized with KOH pellets. The crude material was extracted with Et_2O (3 × 100 mL), dried over $MgSO_4$, filtered, and concentrated *in vacuo*. The crude product was purified by flash column chromatography (70:30, hexanes/EtOAc) to afford 2,3,3-trimethyl-5-methoxy-3H-indole as a red amorphous solid (5.149 g, 99%). ^{1}H NMR (600 MHz, $CDCl_3$) δ 7.43 (d, J = 8.3 Hz, 1H), 6.84-6.80 (m, 2H), 3.82 (s, 3H), 2.24 (s, 3H), 1.28 (s,

6H). ^{1}H NMR is consistent with published data.[162] Following a modified literature procedure,[161] iodomethane (0.048 mL, 0.76 mmol) was added to a solution of 2,3,3-trimethyl-5-methoxy-3H-indole (0.133 g, 0.716 mmol) in anhydrous acetonitrile (14.3 mL). The solution was stirred at reflux for 21 h. The solution was allowed to cool to room temperature, concentrated *in vacuo*, and suspended in $CHCl_3$ (2.5 mL) and hexanes (20 mL). The suspension was sonicated for 30 min and filtered to afford indolium **1** as a pink amorphous solid (0.117 g, 49%). ^{1}H NMR (600 MHz, $CDCl_3$) δ 7.56 (d, *J* = 8.7 Hz, 1H), 7.07-7.01 (m, 2H), 4.23 (s, 3H), 3.90 (s, 3H), 3.04 (s, 3H), 1.65 (s, 6H). ^{1}H NMR is consistent with published data.[160] MS, ESI$^+$: *m/z* = 204.14 $(M+H)^+$.

*5-Dimethylamino-2-hydroxy-benzaldehyde (**2**).*[163]

Following the reported literature,[41] EtOH (30 mL) and aqueous formaldehyde solution (37%, 3.8 mL) were added to a flask containing 2-hydroxy-5-nitrobenzaldehyde (0.160 g, 0.957 mmol) and Pd/C (20 wt%, 0.098 g). CAUTION: Pd/C is pyrophoric and must be handled under appropriate safety protocols. The solution was purged with argon and then H_2. The mixture was then stirred under a balloon of H_2 for 18 h at room temperature. Additional aqueous formaldehyde solution (37%, 2.0 mL) was added, and the mixture was again purged with argon and H_2, and then stirred for an additional 24 h under a balloon of H_2. The mixture was filtered through Celite and the filtrate was acidified with 1 M HCl (15 mL) and concentrated *in vacuo*. The residue was neutralized with saturated aqueous $NaHCO_3$ and extracted with CH_2Cl_2 (3 × 35 mL). The combined organic extracts were dried over Na_2SO_4 concentrated *in vacuo*. Purification by flash chromatography (8:2, hexanes/EtOAc) afforded aldehyde **2** as a red oil (0.117 g, 74%). ^{1}H NMR (600 MHz, $CDCl_3$) δ 10.45 (s, 1H), 9.86 (s, 1H), 7.08 (dd, *J* = 9.0, 3.1 Hz, 1H), 6.91 (d, J = 9.0

Hz, 1H), 6.85 (d, *J* = 3.0 Hz, 1H), 2.91 (s, 6H). ^{1}H NMR was consistent with that reported in the literature.[163] MS, ESI^{-}: *m/z* = 164.07 $(M-H)^{-}$.

*5'-Methoxy-N,N,1',3',3'-pentamethylspiro[chromene-2,2'-indolin]-6-amine (**SP-14**).*

Following the reported literature,[154] to a solution containing indolium **1** (0.223 g, 0.707 mmol) in EtOH (5.0 mL) was added salicylaldehyde **2** (0.117 g, 0.708 mmol) and Et_3N (0.20 mL, 1.4 mmol). The solution was refluxed for 4 h before being concentrated *in vacuo*. Purification by column chromatography (85:15 to 80:20, hexanes/EtOAc) afforded **SP-14** as a red amorphous solid (0.118 g, 47%). IR (cm^{-1}); 2968 (CH_3 asymmetric stretching), 2874 (CH_3 symmetric stretching), 1650 (C=C stretching), 1600 (aromatic ring), 1488 (CH_3 asymmetric bending), 1390 (CH_3 symmetric bending), 1273 and 1251 (C–N stretching), 1217 (C–O stretching), 1183 ($COCH_3$ stretching), 1127 and 1097 (CH out of plane asymmetric stretching), 1031 and 1010 (CH out of plane symmetric stretching), 956 (O–C–N stretching); ^{1}H NMR (600 MHz, $CDCl_3$); δ 6.81 (d, *J* = 10.1 Hz, 1H), 6.73 (d, *J* = 2.5 Hz, 1H), 6.71 (dd, *J* = 8.2, 2.5 Hz, 1H), 6.66 (d, *J* = 8.8 Hz, 1H), 6.61 (dd, *J* = 8.8, 2.9 Hz, 1H), 6.51 (d, *J* = 2.9 Hz, 1H), 6.43 (d, *J* = 8.2 Hz, 1H), 5.68 (d, *J* = 10.1 Hz, 1H), 3.80 (s, 3H), 2.86 (s, 6H), 2.60 (s, 3H), 1.11 (s, 3H), 1.17 (s, 3H); ^{1}H NMR was consistent with previous literature report.[153] HRMS, ESI^{+}: *m/z* = 351.21 $(M+H)^{+}$.

2.3.3 COPPER TITRATION PROCEDURES

The absorption spectra were recorded on a Cary Bio-100 UV-vis spectrometer using a quartz cell with 1.0 cm path length and volume of 700 mL. For precision and accuracy, all solutions were freshly prepared and experimental conditions maintained for all assays. Stock solutions of the cations (1.4×10^{-2} M) were prepared in de-ionized ultra-filtered (D.I.U.F) water and **SP-14** (1

$\times 10^{-4}$ M) was prepared in ethanol in the dark. The titration was accomplished by placing 700 mL of an **SP-14** stock solution (1.16×10^{-4} M = 100 µM SP in ethanol) directly into the cuvette and adding copper(II) ([Cu^{2+}] from a stock (1.4×10^{-3} M in D.I.U.F water, 200 µM will be 116.6 mL), diluted to a fixed total volume (816.6 µL) was added for all concentrations, and incubated in the dark for 15 min. The change in absorbance at 418 nm and 677 nm was plotted against copper(II) ion concentration.

Response of Phenol and N,N-dimethylaniline to Cu^{2+} in ethanol

Absorbance profiles of phenol (100 mM) and *N*,*N*-dimethylaniline (100 mM) were obtained in a 700 µL solution of the above reference compounds after adding varying amounts (0-1.4 eq) of Cu^{2+} in ethanol and incubating in the dark for 15 min.

Job's Plot Analysis

Data for Job's plot was generated by maintaining a fixed total molarity of **SP-14** and copper(II) chloride at 1×10^{-4} M while varying the molar equivalents of each. The absorbance was recorded at 677 nm with maximal absorbance achieved at 0.5 molar equivalents of **SP-14** and copper(II) chloride. The ratio of copper(II) to **SP-14** was systematically varied (0 to 0.9) keeping a fixed total molarity (100 mM) and keeping constant sample volume (700 µL).

Limit of Detection (LOD)

700 mL of an **SP-14** stock solution (1.02×10^{-4} M = 100 µM SP in ethanol) was added directly into the cuvette. To the cuvette was added a known amount of copper(II) ([Cu^{2+}] from a

stock (3.8×10^{-5} M in D.I.U.F water , 0.80 µM = 15 mL), diluted to a fixed total volume (715 µL) , mixed with Pasteur pipet, and incubated in the dark for 15 min, followed by absorbance measurement. This was repeated in triplicate for copper (II) concentrations ranging from 0 – 0.80 µM and the triplicates at each concentration were averaged to obtain the value. The order of the copper (II) concentrations were determined using a random number generator. The LOD for the sensor was calculated by first using linear ordinary least squares (OLS) regression (R version 3.6.0) of baseline corrected absorbance vs [Cu] in µM to determine the mean square error (MSE). The MSE of OLS was used as an estimate of the error variance σ^2 while the intercept of the OLS fit was taken to be representative of the blank (0 µM) absorbance. The LOD was defined as the minimum [Cu] which resulted in an absorbance no greater than 3σ from the blank.

*2.3.4 Absorbance profile of **SP-14** with equimolar (1X) metal chlorides*

700 µL of a 1×10^{-4} M solution of **SP-14** in ethanol was added into a quartz cuvette. This solution, prepared under dark conditions, was scanned for an initial absorbance profile. To the cuvette, was then added one equivalent of metal chloride (5 µL of a 1.4×10^{-2} M solution of metal chloride in D.I.U.F water) and incubated in the dark for 15 min, followed by absorbance measurement.

2.3.5 Competition studies

Equimolar (1X) Metal Chlorides to Copper(II) Chloride (1X)

700 µL of a 1×10^{-4} M solution of **SP-14** in ethanol was added into a quartz cuvette. This solution, prepared under dark conditions, was scanned for an initial absorbance profile. To the

cuvette, was then added one equivalent of metal chloride (5 μL of a 1.4×10^{-2} M solution of metal chloride in D.I.U.F water) and one equivalent of copper(II) chloride (5 μL of a 1.4×10^{-2} M solution of copper(II) chloride in D.I.U.F water), mixed with a Pasteur pipet, incubated under dark for 15 min, followed by absorbance measurement. For the photographs in Figure 7, these procedures were scaled to 21.4 μL metal chloride, 21.4 μL copper (II) chloride and 3mL of ethanol, (metals only), or 3 mL of **SP-14** (colorimetric detection).

Ten Equivalents (10X) Metal Chlorides to Copper(II) Chloride (1X)

700 μL of a 1×10^{-4} M solution of **SP-14** in ethanol was added into a quartz cuvette. This solution, prepared under dark conditions, was scanned for an initial absorbance profile. To the cuvette, was then added ten equivalents of metal chloride (50 μL of a 1.4×10^{-2} M solution of metal chloride in D.I.U.F water), mixed with a Pasteur pipet, incubated under dark for 15 min, followed by absorbance measurement. Subsequently, one equivalent of copper(II) chloride (5 μL of a 1.4×10^{-2} M solution of copper(II) chloride in D.I.U.F water) was added to the cuvette, mixed with a Pasteur pipet, incubated under dark for 15 min, followed by absorbance measurement. For the photographs in Figure 7, these procedures were scaled to 214 μL metal chloride, 21.4 μL copper(II) chloride and 3mL of ethanol (metals only), or 3 mL of **SP-14** (colorimetric detection).

2.4 CONCLUSION AND FUTURE DIRECTIONS

In this work, the metal selectivity and sensing properties of a spiropyran molecular sensor was demonstrated. **SP-14** showed selectivity toward copper(II) ions, which offered qualitative naked eye detection (colorless to green) and quantitative detection of copper(II). The sensor demonstrated two absorbance maxima in response to metal ions with selectivity for copper(II) at a wavelength of 677 nm. The stoichiometry of metal binding was determined to be 1:1 and was consistent with other copper(II) colorimetric sensors.[153,154] Detection was possible even in the presence of 10x molar equivalents of other metals, with exception of iron and lead. **SP-14** exhibited sensitivity down to the micromolar range with a calculated limit of detection of 0.11×10^{-6} M. In addition, the ability to visually detect copper(II) concentrations down to ≈ 6 μM offers the potential for sensitive and rapid sensing in field samples.

We acknowledge that sensing in a solvent such as ethanol has some limitations, however, contaminants in organics can also be an issue and this system could be useful for other applications such as copper sensing in jet fuels, which is hampered by the volatility during typical analysis techniques.[164] The use of organics to enhance sensor solubility is not unusual. Of the 15 sensors with sub 10 micromolar naked eye sensitivity, similar to ours, 13 of these were in pure organic solvents or mixtures of solvents such as acetonitrile, methanol, DMSO, DMF, or ethanol. Three papers report results in water, but neither of these papers demonstrate naked eye detection even in the presence of competing metals.[128,147,149] While **SP-14** has limited solubility in water, efforts are currently underway to apply this sensor as a paper-based diagnostic and preliminary evidence shows that the sensor dried to paper can sense solutions of copper in water. We are also working to adapt this system for 100% aqueous applications by increasing solubility. Although it is a concern that spiropyrans undergo spontaneous ring opening in water, there have been studies in

which spiropyrans revealed to be an effective probe in PBS[128] and water.[165] As presented here, copper can be detected by visual inspection at low concentrations under a number of conditions, which could provide first-pass analysis of copper content in the field. Further experiments to explore the potential applications of these compounds are underway, as well as efforts to develop more sensitive copper(II) agents.

CHAPTER 3: EXAMINATION OF THE MEROCYANINE-GLUTATHIONE INTERACTION

The work described in this chapter has been reported in:

Trevino, K. M., Addison, B., Louie, A. Y., Garcia, J., Investigating the interaction between merocyanine and glutathione through a comprehensive NMR analysis of three GSH-stabilized merocyanine species, *Magn Reson Chem* **2023**, 61(8), 487. https://doi.org/10.1002/mrc.5369

Adapted with permission from Wiley

3.1 GLUTATHIONE AND ITS BIOCHEMICAL FUNCTION

Glutathione (GSH) is a tripeptide composed of glutamate, cysteine, and glycine. It is present in the human body with concentrations around 0.5-10 mM intracellularly[166–168] and 2-20 μM extracellularly.[169,170] GSH acts as a primary intracellular and extracellular antioxidant, stemming from the thiol on the cysteine that allows GSH to be oxidized to glutathione disulfide (GSSG).[171–173] Reduction of GSSG and regeneration of GSH is possible by means of glutathione reductase.[174] The reversibility from GSH to GSSG allows GSH to act as powerful antioxidant to scavenge free radicals produced by reactive oxygen species (ROS) and prevent oxidative stress, which is linked to several diseases such as Parkinson's, Alzheimer's, amyotrophic lateral sclerosis (ALS) etc.[175–178] While GSH has a profound importance, there have been shortcomings in the development of a biosensor for GSH due to issues such as specificity, selectivity, detection limit, detection method, etc. We have previously reported several GSH responsive spiropyrans[179] and acknowledge the complexity of the spiropyran glutathione interaction. Thus, in this chapter we present our current publication[180] in which we propose a favorable conformation between three GSH-stabilized merocyanine species in hopes of helping to elucidate the mechanism of spiropyrans for GSH.

3.2 GLUTATHIONE'S EFFECT ON SPIROPYRAN

Spiropyrans belong to a class of photochromic materials that are known to undergo reversible structural changes from ring-closed spiropyran to ring-open merocyanine isomer in response to different external stimuli, such as redox changes. Sensing redox active molecules such as the potent antioxidant glutathione (GSH) is of interest due to the observation that changes in

GSH levels are indicative of oxidative stress and correlated with a number of pathological conditions[181–183] Several GSH-responsive spiropyrans have been reported[54,179,184–188]; however, these spiropyrans exhibited modest sensitivity and selectivity towards the antioxidant. In addition, the specificity of recognition of these photoswitches to GSH remains imperfect. Understanding the structural details of the spiropyran isomers using NMR spectroscopy may provide insights to how these photoswitches sense GSH. While ^{1}H NMR spectra of different spiropyrans are readily available in the literature[189–200], the availability of ^{1}H NMR data of merocyanine species is rising but still limited.[179,201–211] Thiele et. al.[212] provided nearly complete ^{13}C chemical shift assignment of the merocyanine species from a light-irradiated spiropyran featuring a nitro substituent in the chromene group, and a carboxylic acid attached to the indolic nitrogen (Figure 3.1A). However, some ^{1}H and ^{13}C assignments, specifically the olefinic protons and carbons (shown in red asterisks in Figure 3.1A) at the bridging part of the molecule, were inconclusive. NMR characterization of these protons and carbons are important for determining spatial isomers (e.g., *cis* or *trans*), an important piece of structural information for understanding the mechanism governing GSH sensing using spiropyrans. Therefore, a complete NMR (^{1}H and ^{13}C NMR) characterization of three GSH-stabilized merocyanines: (E)-2-(2-(5-methoxy-1,3,3-trimethyl-3H-indol-1-ium-2-yl)vinyl)phenolate (**MC-3)**, (E)-4-methoxy-2-(2-(1,3,3-trimethyl-3H-indol-1-ium-2-yl)vinyl)phenolate (**MC-7)**, and (E)-4-methoxy-2-(2-(5-methoxy-1,3,3-trimethyl-3H-indol-1-ium-2-yl)vinyl)phenolate (**MC-9**) from a series of three spiropyrans: 5'-methoxy-1',3',3'-trimethylspiro[chromene-2,2'-indoline] (SP-3), 6-methoxy-1',3',3'-trimethylspiro[chromene-2,2'-indoline] (SP-7), and 5',6-dimethoxy-1',3',3'-trimethylspiro[chromene-2,2'-indoline] (SP-9) (Figure 3.1B) was accomplished. These three structures differ in the number of methoxy groups they contain: **MC-3** bearing a methoxy on the para position of the indoline unit, **MC-7** bearing a

methoxy on the para position of the phenolic oxygen and **MC-9** bearing a methoxy on both sides. Comprehensive NMR characterization of GSH-stabilized merocyanines could aid in the identification of stereochemistry of the GSH-stabilized merocyanine species and may help in providing improved understanding of the sensing mechanism of these photoswitches for GSH.

a) Previous work by Thiele et al.

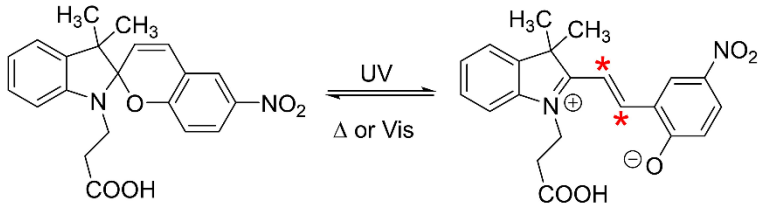

Spiro (SP) form **Mero (MC) form**

b) Our work

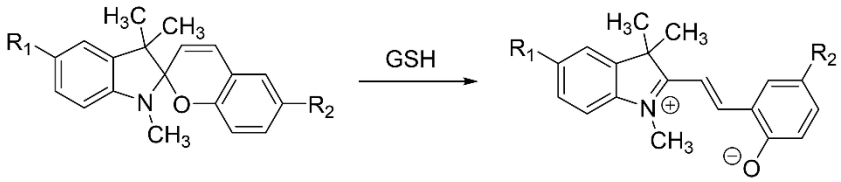

Spiro (SP) form **Mero (MC) form**

	R_1	R_2
SP-3 or **MC-3**	OCH_3	H
SP-7 or **MC-7**	H	OCH_3
SP-9 or **MC-9**	OCH_3	OCH_3

Figure 3.1. *Structures of the spiro and mero forms of (A) the photoswitch reported by Thiele et. al.*[212] *and (B) the glutathione-responsive spiropyrans SP-3, SP-7, and SP-9 presented in this chapter.*

3.3 INVESTIGATING THE INTERACTION BETWEEN MEROCYANINE AND GLUTATHIONE (GSH) THROUGH A COMPREHENSIVE NMR ANALYSIS OF THREE GSH-STABILIZED MEROCYANINE SPECIES

3.3.1 SYNTHESIS OF SP-3, SP-7, & SP-9

The synthesis of SP-3, SP-7, & SP-9 have previously been reported.[153] Briefly, for SP-3 and SP-9, the indolium iodide was prepared from the methoxyhydrazine through an interrupted Fisher indole synthesis, followed by methylation with iodomethane to produce 5-methoxy-1,2,3,3-tetramethyl-3H-indol-1-ium (Scheme 3.1A). Commercially available 1,3,3-trimethyl-2-methyleneindoline was used for the synthesis of SP-7 (Scheme 3.1B). The synthesis of these three derivatives ultimately proceeded through the nucleophilic attack of the Fischer base on the respective salicylaldehyde to produce the desired spiropyran (Scheme 3.1).

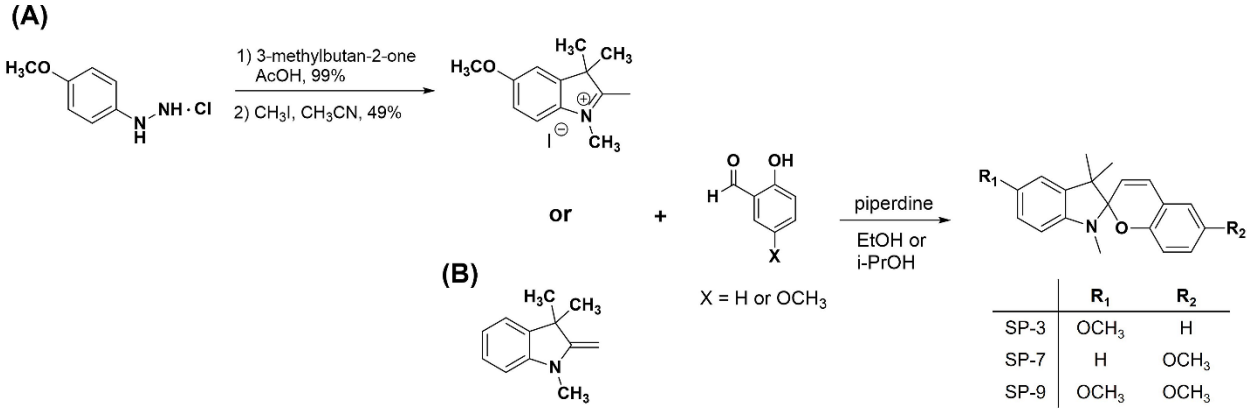

Scheme 3.1. *Synthetic routes for (A) SP-3, SP-9 and (B) SP-7.*

*3.3.2 ^{1}H AND ^{13}C NMR ASSIGNMENTS OF **MC-3**, **MC-7**, & **MC-9***

The ^{1}H and ^{13}C NMR characterization of GSH-stabilized merocyanine species, **MC-3**, **MC-7**, **MC-9**, was determined by using ^{1}H, ^{13}C, COSY, NOESY, HSQC and HMBC to better understand the interaction between spiropyran and GSH. The number of methoxy groups in each compound ranged from one to two, and there were three methyl groups for all the reported spiropyrans. The proposed ^{1}H and ^{13}C NMR chemical shifts, assignments, and general structure of merocyanines **MC-3**, **MC-7**, and **MC-9** are presented in Table 3.1. Additionally, the proposed ^{1}H and ^{13}C NMR chemical shifts, assignments, and general structure of spiropyrans SP-1, SP-2, and SP-3 are available in the additional information section 3.6, Table 3.2. All protons are numbered by their attached carbons. The respective proton peaks corresponding to the closed spiro form of SP-3, SP-7, and SP-9 alone (Additional Information, Figures 3.8, 3.9, & 3.10) and with the addition of GSH (Figure 3.2, Additional Information, Figures 3.11 & 3.12.) are provided in the additional figures section 3.6. The carbon peaks for the GSH stabilized merocyanines **MC-3**, **MC-7**, and **MC-9** can also be found in the additional information section 3.6, Figures 3.13, 3.14, & 3.15.

Table 3.1. *^{1}H and ^{13}C NMR chemical shifts of the merocyanine forms **MC-3**, **MC-7**, and **MC-9** in 1:1 CD_3CN/phosphate buffered saline (pH 7.4), and multiplicity and coupling constants (expressed in Hz) are given in parentheses.*

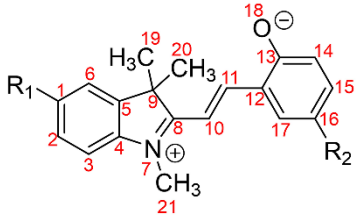

MC-3: $R_1 = {}^{22\,23}OCH_3$, $R_2 = H$

MC-7: $R_1 = H$, $R_2 = {}^{24\,25}OCH_3$

MC-9: $R_1 = {}^{22\,23}OCH_3$, $R_2 = {}^{24\,25}OCH_3$

m/z $(M+H)^+$
308.16
308.16
338.17

Position	**MC-3**		**MC-7**		**MC-9**	
	^{1}H	^{13}C	^{1}H	^{13}C	^{1}H	^{13}C
1	–	161.95	7.55–7.59 (m)	129.05	–	160.78
2	7.10 (dd; 2.5, 8.8)	115.85	7.55–7.59 (m)	129.31	7.10 (dd; 2.5, 8.9)	114.68
3	7.57 (d, 8.8)	116.74	7.66 (d, 7.0)	114.36	7.57 (d, 8.8)	115.55
4	–	136.08	–	141.38	–	134.90
5	–	146.32	–	142.86	–	145.16
6	7.23 (d, 2.5)	109.29	7.65 (d, 7.2)	122.38	7.23 (d, 2.5)	108.09
8	–	181.35	–	182.24	–	180.00
9	–	52.50	–	51.92	–	51.85
10	7.47 (d, 16.4)	112.66	7.50 (d, 16.4)	111.46	7.43 (d, 16.4)	111.47
11	8.40 (d, 16.4)	148.89	8.47 (d, 16.4)	148.92	8.38 (d, 16.4)	147.11
12	–	122.34	–	121.12	–	121.26
13	–	159.72	–	152.63	–	152.56
14	6.98 (d, 8.5)	117.83	6.95 (d, 9.0)	117.71	6.93 (d, 9.0)	117.77
15	7.40 (td; 8.5, 7.2, 1.6)	121.28	7.07 (dd; 9.0, 3.1)	123.11	7.04 (dd; 3.1, 9.0)	122.57
16	6.96 (t; 7.9, 7.2)	136.20	–	153.21	–	153.16
17	7.80 (dd;7.9, 1.6)	130.71	7.33 (d, 3.1)	111.75	7.30 (s)	111.62
19	1.69 (s)	26.63	1.71 (s)	25.38	1.69 (s)	25.43
20	1.69 (s)	26.58	1.71 (s)	25.36	1.69 (s)	25.38
21	3.91 (s)	34.83	3.96 (s)	33.62	3.92 (s)	33.69
23	3.84 (s)	56.60	–	–	3.84 (s)	55.74
25	–	–	3.78 (s)	55.36	3.77 (s)	55.56

Multiplicities, s, d, t, and m represent singlet, doublet, triplet, and multiplet, respectively.

3.3.3 STRATEGY IN DETERMINING THE SPECTRAL ASSIGNMENTS FOR MC-3, MC-7, & MC-9

The NMR spectral assignment strategy for all three merocyanine compounds was as follows: (1) identify all ^{1}H resonances associated with each of the three chemical species (i.e., closed-form spiropyran, open-form merocyanine, and glutathione) in the sample; (2) assign all ^{1}H resonances by analyzing chemical shifts, peak areas, homonuclear couplings and multiplicities, and NOE cross peaks; (3) assign all ^{13}C resonances with attached protons using heteronuclear single quantum coherence (HSQC) data; and (4) assign the remaining quaternary carbons using heteronuclear multiple-bond correlation (HMBC) data and chemical shift analysis. NMR data of merocyanine species **MC-7** and **MC-9** were determined using a similar procedure as **MC-3** described here: The sample used for NMR analysis contained three different chemical species, thus the first step was to assign all ^{1}H resonances to one of three compounds: glutathione (grey), SP-3 (closed-form, blue), or **MC-3** (open-form, black) and CD_3CN reference (red). (Figure 3.2).

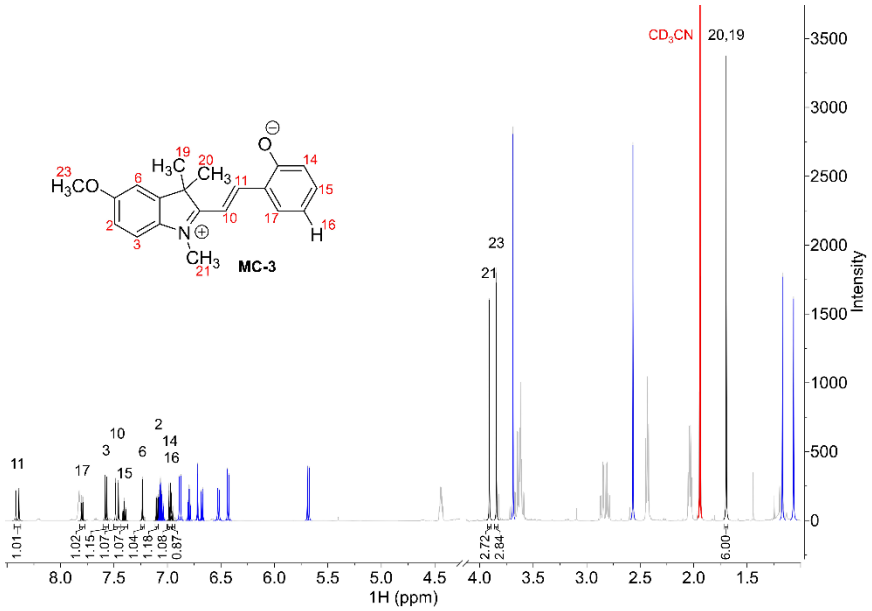

Figure 3.2. *^{1}H NMR Spectrum of GSH-stablilzed **MC-3**. **MC-3** (black), SP-3 (blue), GSH (grey), CD_3CN reference (red). The **MC-3** species was induced using 5 mM SP-3 and GSH in equimolar concentration in deuterated acetonitrile/phosphate buffered saline (PBS, 1X, pH 7.4) (1:1 v/v)*

This was easily accomplished by comparing integration areas; 9 conjugated and 4 methyl-group resonances were identified for **MC-3** and SP-3 with a ratio of 1:1.15 MC: SP. The ^{1}H signals at 1.69 ppm (H-19, H-20) were identified based on chemical shift and peak area (6H). The protons H-19 and H-20 are indistinguishable and appeared as singlet in the ^{1}H NMR spectrum suggesting two magnetically equivalent methyl groups in the indole moiety. The similar magnetic environment experienced by these methyl protons is a result of being in a planar merocyanine structure. However, it is interesting to note that these two methyl groups give rise to two unique ^{13}C resonances in the HSQC spectrum at 26.63 ppm and 26.58 (C-19 and C-20), shown in Figure S5, suggesting the existence of two slightly different methyl environments. This indicates either a slight bend in the planar merocyanine structure, or possibly a change in environment caused by the presence of GSH on either side of the molecule. This was observed for the **MC-7** and **MC-9** species as well, with a singlet for the H-19 and H-20 protons in **MC-7** (1.71 ppm) and **MC-9** (1.69 ppm) for the ^{1}H spectrum x-axis of the HSQC. Two unique ^{13}C peaks for **MC-7** (25.38 ppm and 25.36 ppm) and **MC-9** (25.38 ppm and 25.43 ppm) were also noticed for the ^{13}C spectrum y-axis of the HSQC spectrum (Additional Information, Figures 3.16, 3.17, & 3.18). Further insight into the interaction between GSH and spiropyrans can be gained through additional chemical shift interpretation and computational studies.

The remaining proton and carbon resonances were assigned as follows: NOESY NMR spectrum of **MC-3** allowed us to examine the spatial proximity of protons H-19/H-20 (1.69 ppm) to protons H-6 and H-11 at 7.23 and 8.40 ppm, respectively. Clear NOE cross peaks with H-19/H-20 with H-6 and H-11 were observed in the NOESY spectrum (Figure 3.3).

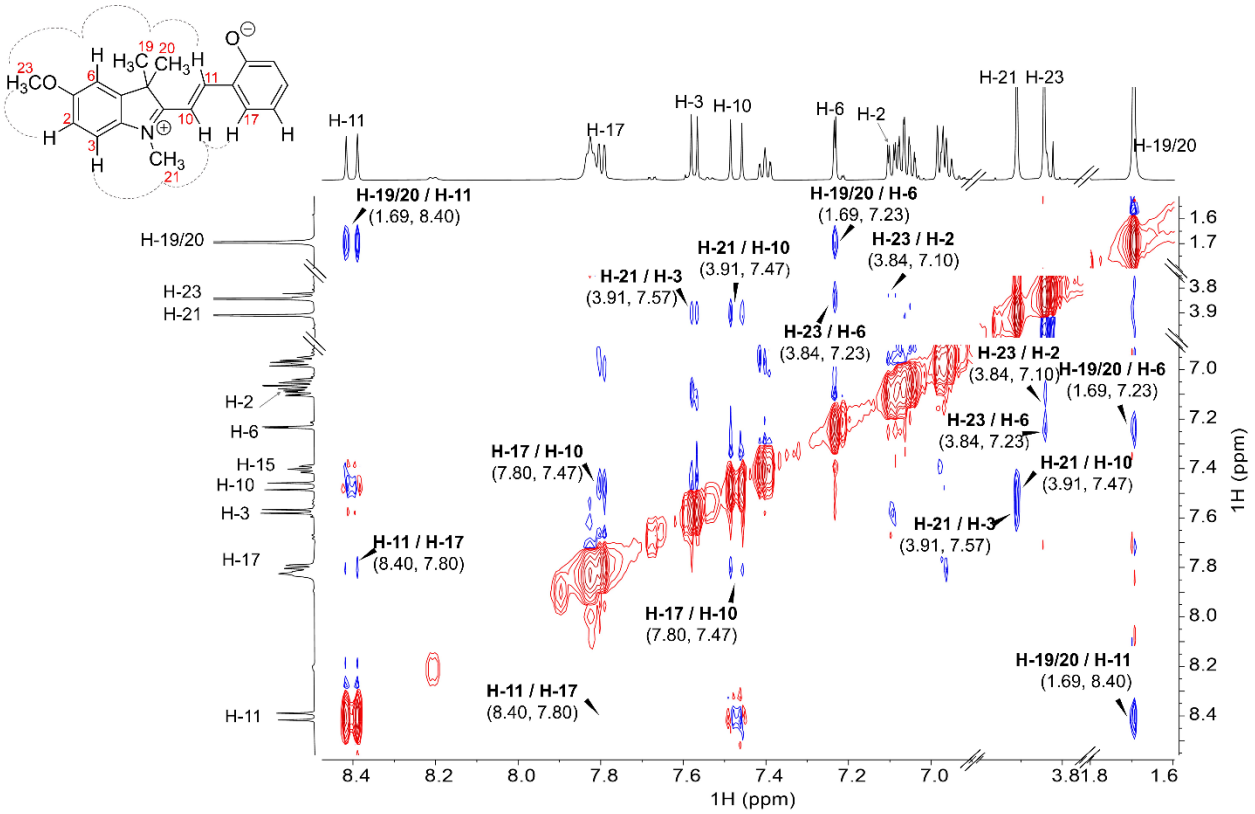

Figure 3.3. *NOESY spectrum of GSH-stabilized* ***MC-3****. NOESY correlations (dashed lines) of* ***MC-3****. NOESY spectrum has been cut for clarity and full spectrum can be found in supplementary Additional Information, Figure 3.19.*

Once the H-6 and H-11 proton chemical shifts were identified by NOESY, the direct correlation of these protons to the bound carbon was found to be C-6 (109.29 ppm) and C-11 (148.89 ppm) through HSQC NMR spectrum (Additional Information, Figure 3.22). Based on the identification of H-11, the H-10 proton could be assigned using COSY with a ^{1}H assignment of 7.47 ppm (Figure 3.4)

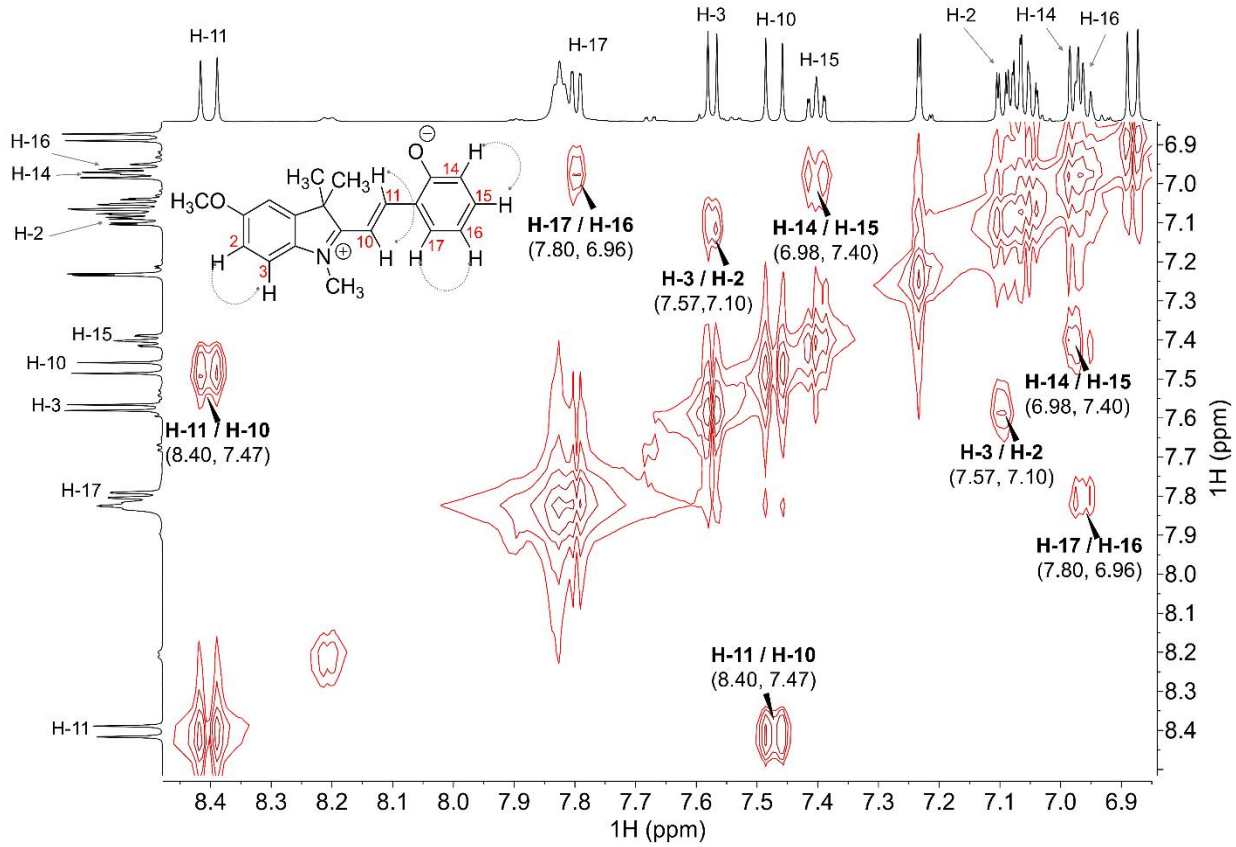

Figure 3.4. *COSY spectrum of GSH-stabilized* ***MC-3****. Inset: COSY correlations (dotted lines) of* ***MC-3****. The* ***MC-3*** *species was induced using 5 mM SP-3 and GSH in equimolar concentration in deuterated acetonitrile/phosphate buffered saline (PBS, 1X, pH 7.4) (1:1 v/v)*

Additionally, H-10 and H-11 could be identified based on chemical shift, multiplicity (doublets), and the characteristic *J*-coupling constant of 16 Hz for olefinic protons in a *trans* conformation. It is noted that H-11 is the most deshielded among the merocyanine ^{1}H peaks due to ring-current effects and additionally due to the delocalization of π electrons towards the positively charged indolic nitrogen, causing the carbon to which this proton is attached to carry a partial positive charge. The two protons H-11 and H-10 are correlated to ^{13}C peaks at 148.89 (C-11) and 112.66 ppm (C-10), respectively in the HSQC spectrum (Additional Information, Figure 3.22).

The protons in the methoxy group (H-23, 3.84 ppm) and the methyl attached to the indolic nitrogen (H-21, 3.91 ppm) were close in chemical shift but could be differentiated through observed NOE cross peaks shown in Figure 3; H-21 with resonances H-3 and H-10, and H-23 with resonances H-2 and H-6. Further elucidation of their associated ^{13}C chemical shifts was observed in the HSQC spectrum (Additional Information, Figure 3.22). The signals of the remaining ^{1}H resonances on the indoline fragment (H-2 and H-3) were assigned by analyzing homonuclear COSY and NOESY correlations. As aforementioned, an NOE cross peak was observed between H-21 and H-3, a doublet at 7.57 ppm (Figure 3.3). In the COSY spectrum of Figure 4, H-3 showed *J*-coupling to the doublet of doublets at 7.10 ppm (H-2). ^{13}C resonances C-2, C-3, and C-6 were identified from the HSQC spectrum (Additional Information, Figure 3.22).

The remaining four aromatic ^{1}H resonances from the ring-open chromene moiety (H-14, H-15, H-16, H-17) were assigned based on COSY, HSQC, and NOESY spectra. A NOE cross peak was observed between a doublet of doublets at 7.80 ppm and both H-11 and H-10; thus this was assigned to H-17 (Figure 3.3). Interestingly, the NOE cross peak intensity was much stronger between H-17 and H-10 than between H-17 and H-11, strongly suggesting a *trans* conformation *TTT*. (This is discussed further with respect to Figure 3.7). After assigning H-17, the triplet at 6.96 ppm could then be assigned to H-16 from the COSY spectrum in Figure 3.4. Furthermore, the triplet H-15 (7.40 ppm) and the doublet at 6.98 ppm could then be assigned to H-14, through observed COSY cross peaks (Figure 3.4). These assignments are consistent with chemical shielding concepts; H-14 and H-16 were more shielded compared to H-15 and H-17 due to the partial negative charge to the carbon atoms to which H-14 and H-16 are attached due to electron delocalization. Again, associated ^{13}C resonances were assigned using HSQC data by observed cross-peaks with attached protons (Additional Information, Figure 3.22).

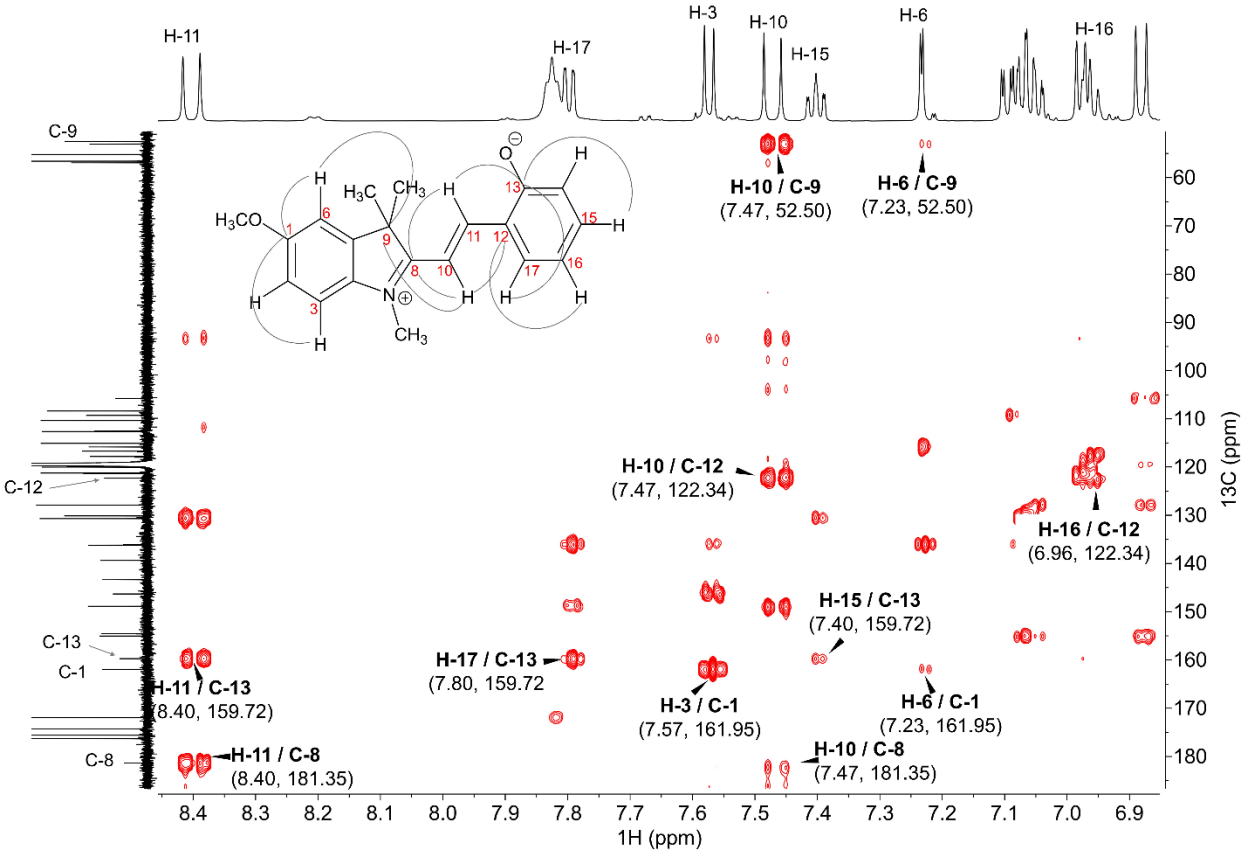

Figure 3.5. *HMBC spectrum of GSH-stabilized* ***MC-3.*** *Inset: HMBC correlations (solid lines) of* ***MC-3****. The* ***MC-3*** *species was induced using 5 mM SP-3 and GSH in equimolar concentration in deuterated acetonitrile/phosphate buffered saline (PBS, 1X, pH 7.4) (1:1 v/v)*

Five quaternary carbons were identified in the HMBC spectrum and assigned to C-1, C-8, C-9, C-12, and C-13 through careful analysis (Figure 3.5). Basic chemical shift prediction was used to aid in quaternary carbon assignments. For example, the three most downfield quaternary carbons at 181.35 ppm (HMBC to H-11 & H-10), 161.95 ppm (HMBC to H-3, H-6) and 159.72 ppm (HMBC to H-11, H-17, H-15) were assigned to C-8, C-1, and C-13, respectively. This was based on HMBC correlations and by the expectation that their chemical shifts would be the most downfield of all seven quaternary carbons. Similarly, the quaternary carbon C-9 at 52.50 ppm

(HMBC to H-10 & H-6) was easily identified as it is the most shielded among the seven. C-12 at 122.34 ppm was assigned from a strong HMBC correlation to H-10 and a weak coupling to H-16. The last two quaternary carbons, C-4 and C-5 were assigned at 136.08 ppm and 146.32 ppm, respectively. Both of these resonances could be assigned to either C-4 or C-5 based on ambiguous HMBC cross-peaks, so chemical-shift prediction was used to assign C-4 as the more upfield and C-5 as the more downfield. All identified HMBC correlations (solid grey lines), as well as NOESY correlations (dotted blue lines), are indicated in Figure 3.6.

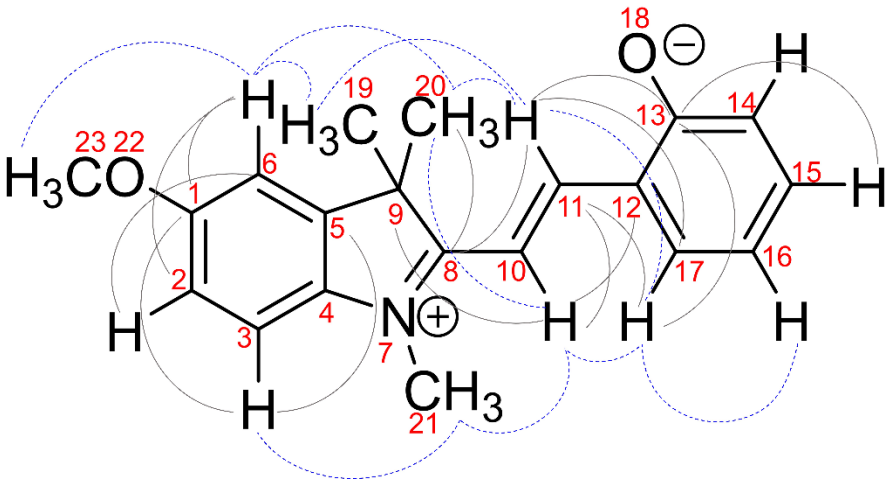

Figure 3.6. *The important correlations obtained from the HMBC (solid grey lines) and NOESY (dotted blue lines) spectra of GSH-stabilized* ***MC-3****.*

3.3.4 Examination of NOESY to determine the most favorable conformation for GSH-stabilized MC-3, MC-7, & MC-9

The high amount of GSH-induced merocyanine species enabled access to complex structural information that can be obtained from 2D NMR experiments such as COSY, HSQC, HMBC, and NOESY. While the closed spiro form locks the olefinic fragment in a cis configuration, computational studies show that the ring-open merocyanine isomer can assume four

different conformations for each of the *trans (TTC, TTT, CTC, CTT),* shown in Figure 3.7A, and *cis* isomers (*CCC, CCT, TCC, TCT*).[15,213,214] 2D NMR revealed that the *trans TTC* and *TTT* were the predominant species for **MC-3, MC-7** and **MC-9**. NOESY showed that the olefinic protons H-10 and H-11 are in *trans* configuration for all MC species due to the presence of NOE cross peaks between H-11 and H-19/20 and cross peaks between H-10 and H-21 (Figure 3.3, Additional Information, Figures 3.20, & 3.21.). These correlations are illustrated using grey dotted lines in Figure 3.7A. Moreover, the absence of NOE cross peaks between H-10 and H-19/20 and cross peaks H-11 and H-21 further supported the *trans TTC* and *TTT* being the two prevalent conformations for all three GSH-stabilized MC species. In order to differentiate between conformation *TTC* and *TTT*, NOE peaks H-10 and H-17 were analyzed against NOE peaks H-11 and H-17 for **MC-3**, **MC-7,** and **MC-9**. These correlations are illustrated using blue dotted lines in Figure 3.7A. Visual inspection of the NOE cross peaks suggest H-10 and H-17 is stronger than the NOE cross peaks H-11 and H-17 for **MC-3** and **MC-7** (Figure 3.7B and 3.7C). This is not completely apparent for **MC-9** (Figure 3.7D). Therefore, NOE intensity values for these cross peaks were examined for all MC species. After analyzing these intensity values for the three MC species it was found that conformation *TTT* was likely to be the thermodynamically favored conformation over *TTC*. This contrasts with the majority of merocyanine structures in the literature that show the *cis* conformation, with the negatively charged oxygen species on the same side as the positively charged indole. It is only possible to observe NOE between H-10 and H-17 when these protons are in *trans* to each other, supporting the *TTT* conformation.

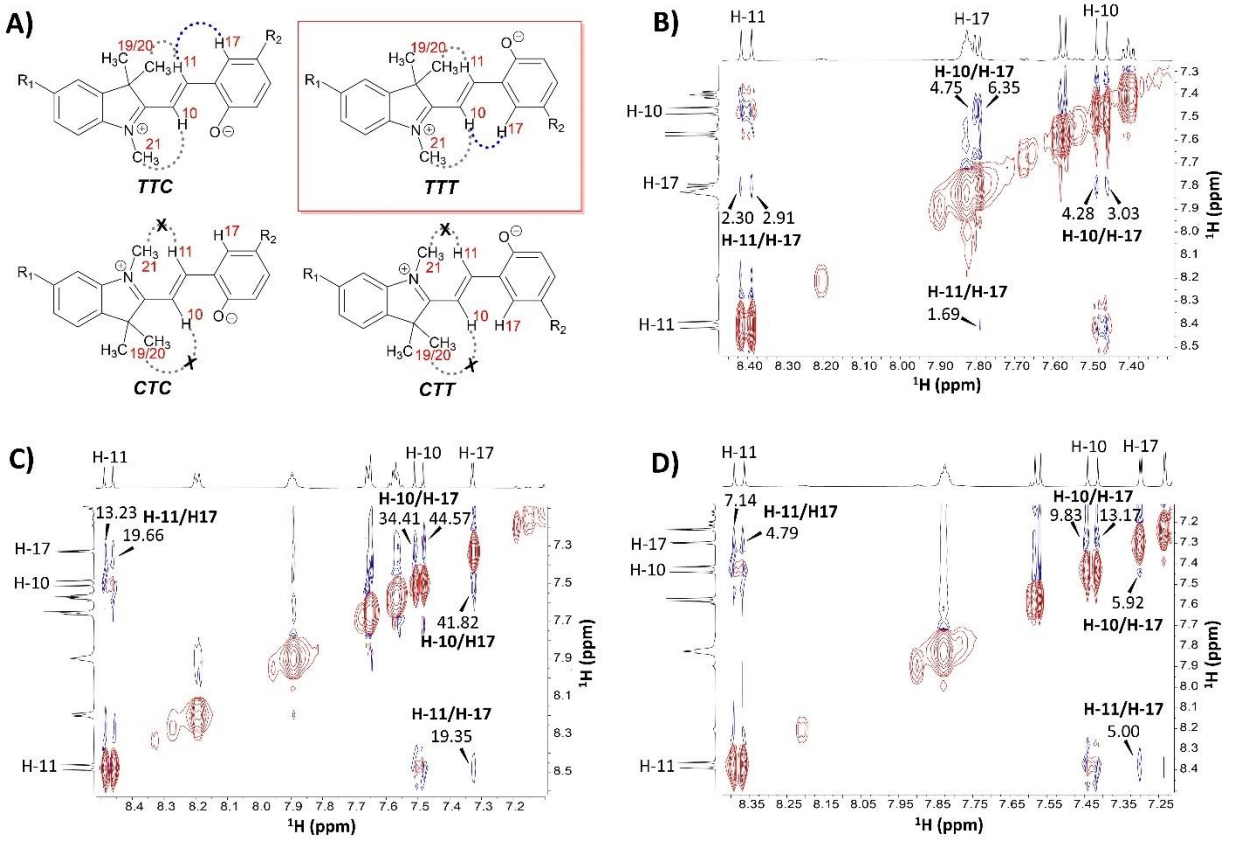

Figure 3.7. *A) The four possible trans conformations (TTC, TTT, CTC, CTT) of the of the GSH-stabilized MC species based on reported computational studies.*[15,213,214] *Experimentally observed NOE correlations (dotted lines) between the protons H-10, H-11, H-17, H-19/20, and H-21. NOE intensity values (blue dotted lines) for proton correlations between H-10 & H-17 and H-11 & H-17, for B)* ***MC-3*** *C)* ***MC-7*** *and D)* ***MC-9****. NOESY data suggest that form TTT (enclosed in red box) is the most favorable conformation of the trans isomer in the presence of GSH.*

3.4 EXPERIMENTAL METHODS

3.4.1 SYNTHESIS AND MASS SPECTROMETRY CHARACTERIZATION

We have previously reported compounds SP-3, SP-7, and SP-9 and their syntheses are described in the literature.[153] All masses were analyzed using a Thermo Q-Exactive High Field Orbitrap. Accurate mass measurements were recorded on positive electrospray ionization mode in CH_3OH.

3.4.2 NMR SAMPLE PREPARATION

Spiropyrans samples with GSH in equimolar concentration (5 mM for SP-1 and SP-3, and 15 mM for SP-2) in deuterated acetonitrile/phosphate buffered saline (PBS, 1X, pH 7.4) (1:1 v/v) were prepared by taking aliquot of appropriate amounts from a stock of spiropyrans (50 mM) in deuterated acetonitrile and a stock solution of GSH (50 mM) in PBS. The combined aliquots were diluted with known volumes of deuterated acetonitrile and PBS to obtain the desired concentrations (5, 10, or 15 mM) and solvent composition (1:1 v/v, pH = 7.4 deuterated acetonitrile/PBS).

3.4.3 NMR EXPERIMENTS

All NMR spectra were collected using a 600 MHz Bruker Avance III spectrometer system (14.1 T; Bruker, Karlsruhe, Germany) at 25 °C, and the chemical shifts were referenced to deuterated acetonitrile. The relaxation delay, pulse width, spectral width, number of data points, and digital resolution in the ^{1}H NMR experiments were 2.47 s, 8.03 µs, 7211.5 Hz, 18028 K, and 0.11 Hz/point, respectively. The same parameters in the ^{13}C NMR experiments were 2 s, 10.75 µs,

36057.7 Hz, 32768 K, and 0.55 Hz/point, respectively. Correlation spectroscopy (COSY) was collected using Bruker cosygpprqf pulse program with a 2 s relaxation delay and acquired with 256 t_1 points with 16 averages per t_1 increment. Heteronuclear single quantum coherence (HSQC) was collected using Bruker hsqcedetgpsp pulse program with a 2 s relaxation delay and acquired with 256 t_1 points with 8 scans per t_1 increment. Heteronuclear bond correlation (HMBC) was collected using Bruker hmbcgpl2ndwg pulse program with a 2 s relaxation delay and acquired with 256 t_1 points with 24 scans per t_1 increment. Nuclear Overhauser spectroscopy (NOESY) was collected using the Bruker noesygpphpr pulse program with a 2 s relaxation delay and acquired with 256 t_1 points. This sequence employs three 90-degree pulses (8.03 µs) with a mixing time of 0.3 s placed between the last 2 pulses. All NMR data were processed with zero-filling and the sine-squared bell window function before Fourier transformation using Topspin 3.2 software on Windows 7 PC Workstation and were analyzed using MestReNova version 14.3.

3.5 CONCLUSION

Complete NMR (^{1}H & ^{13}C) assignments for three GSH-stabilized MC species was achieved by applying 2D NMR techniques such as, HSQC, HMBC, COSY and NOESY. To obtain these stabilized species, GSH was introduced to a sample of the respective spiropyran SP-3, SP-7, or SP-9. This resulted in the isomerization of spiropyran to merocyanine, which ultimately gave rise to the fixed GSH-stabilized **MC-3**, **MC-7,** or **MC-9**. Identification of the methyl environments in the merocyanine forms was the first action taken during spectral analysis. From there, 2D NMR was utilized to locate neighboring environments. Once all NMR assignments were appointed, investigation of the stereochemistry for the three GSH-stabilized MC species was examined.

Presence (H-11 and H-19/20, H-10, and H-21) and absence (H-10 and H-19/20, H-11, and H-21) of NOE peaks supported the *trans* forms *TTC* and *TTT* being the two predominant species. Visual inspection and evaluation of the intensity values for NOE peaks between H-10 and H-17 vs H-11 and H-17 suggest *trans TTT* being the most favorable conformation for **MC-3**, **MC-7,** and **MC-9**. By studying the stereochemistry of these GSH-stabilized MC species we were able to provide a full characterization of the merocyanine forms in hopes of aiding in the structural understanding of new merocyanine species that are stabilized by external chemical stimuli.

3.6 Additional Figures

Table 3.2. ^{1}H and ^{13}C NMR chemical shifts of spiropyran forms **SP-3**, **SP-7**, and **SP-9** in 1:1 CD_3CN/phosphate buffered saline (pH 7.4), and multiplicity and coupling constants (expressed in Hz) are given in parentheses.

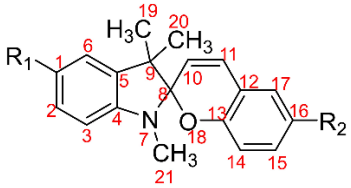

Position	MC-3		MC-7		MC-9	
	^{1}H	^{13}C	^{1}H	^{13}C	^{1}H	^{13}C
1	–	161.95	7.55–7.59 (m)	129.05	–	160.78
2	7.10 (dd; 2.5, 8.8)	115.85	7.55–7.59 (m)	129.31	7.10 (dd; 2.5, 8.9)	114.68
3	7.57 (d, 8.8)	116.74	7.66 (d, 7.0)	114.36	7.57 (d, 8.8)	115.55
4	–	136.08	–	141.38	–	134.90
5	–	146.32	–	142.86	–	145.16
6	7.23 (d, 2.5)	109.29	7.65 (d, 7.2)	122.38	7.23 (d, 2.5)	108.09
8	–	181.35	–	182.24	–	180.00
9	–	52.50	–	51.92	–	51.85
10	7.47 (d, 16.4)	112.66	7.50 (d, 16.4)	111.46	7.43 (d, 16.4)	111.47
11	8.40 (d, 16.4)	148.89	8.47 (d, 16.4)	148.92	8.38 (d, 16.4)	147.11
12	–	122.34	–	121.12	–	121.26
13	–	159.72	–	152.63	–	152.56
14	6.98 (d, 8.5)	117.83	6.95 (d, 9.0)	117.71	6.93 (d, 9.0)	117.77
15	7.40 (td; 8.5, 7.2, 1.6)	121.28	7.07 (dd; 9.0, 3.1)	123.11	7.04 (dd; 3.1, 9.0)	122.57
16	6.96 (t; 7.9, 7.2)	136.20	–	153.21	–	153.16
17	7.80 (dd;7.9, 1.6)	130.71	7.33 (d, 3.1)	111.75	7.30 (s)	111.62
19	1.69 (s)	26.63	1.71 (s)	25.38	1.69 (s)	25.43
20	1.69 (s)	26.58	1.71 (s)	25.36	1.69 (s)	25.38
21	3.91 (s)	34.83	3.96 (s)	33.62	3.92 (s)	33.69
23	3.84 (s)	56.60	–	–	3.84 (s)	55.74
25	–	–	3.78 (s)	55.36	3.77 (s)	55.56

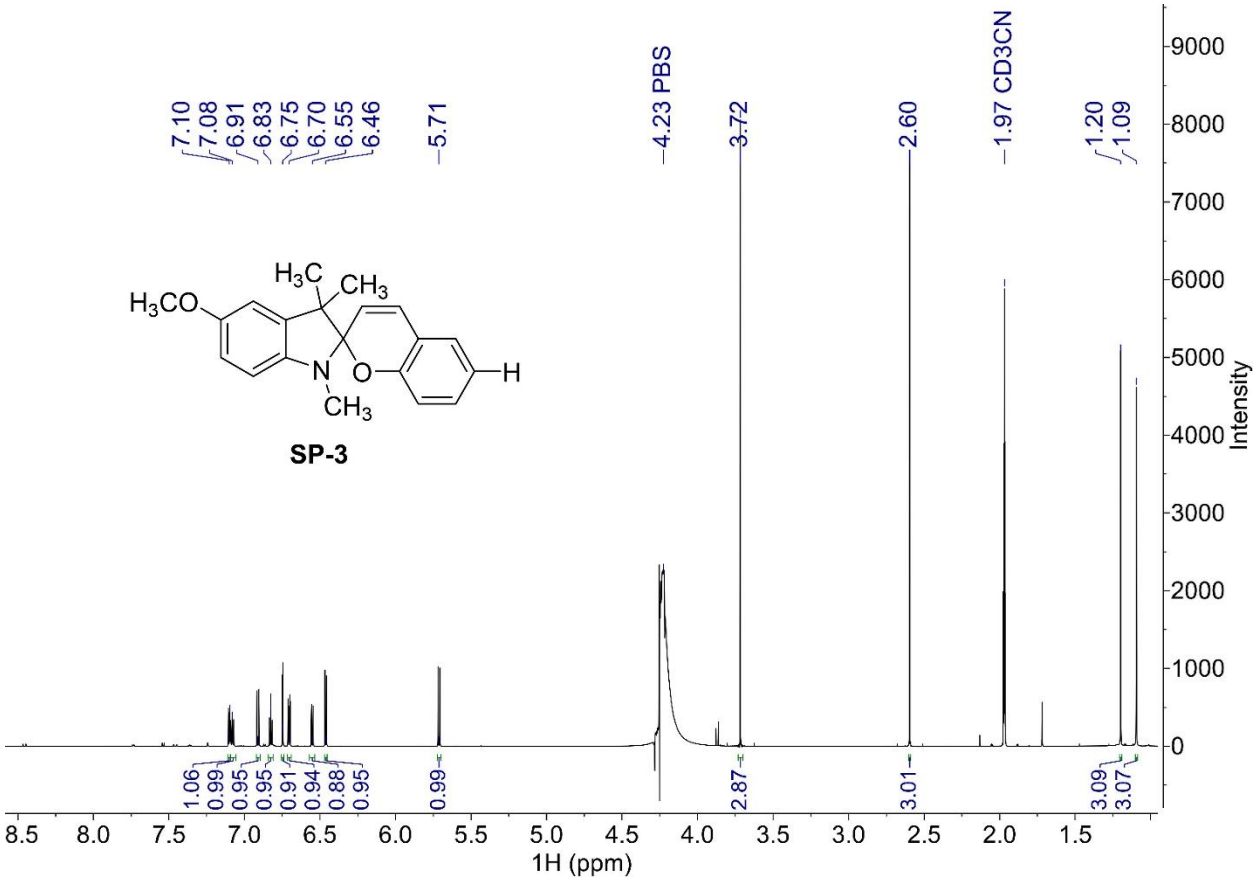

Figure 3.8. *^{1}H NMR of 5 mM SP-3 in deuterated acetonitrile/phosphate buffered saline (PBS, 1X, pH 7.4) (1:1 v/v).*

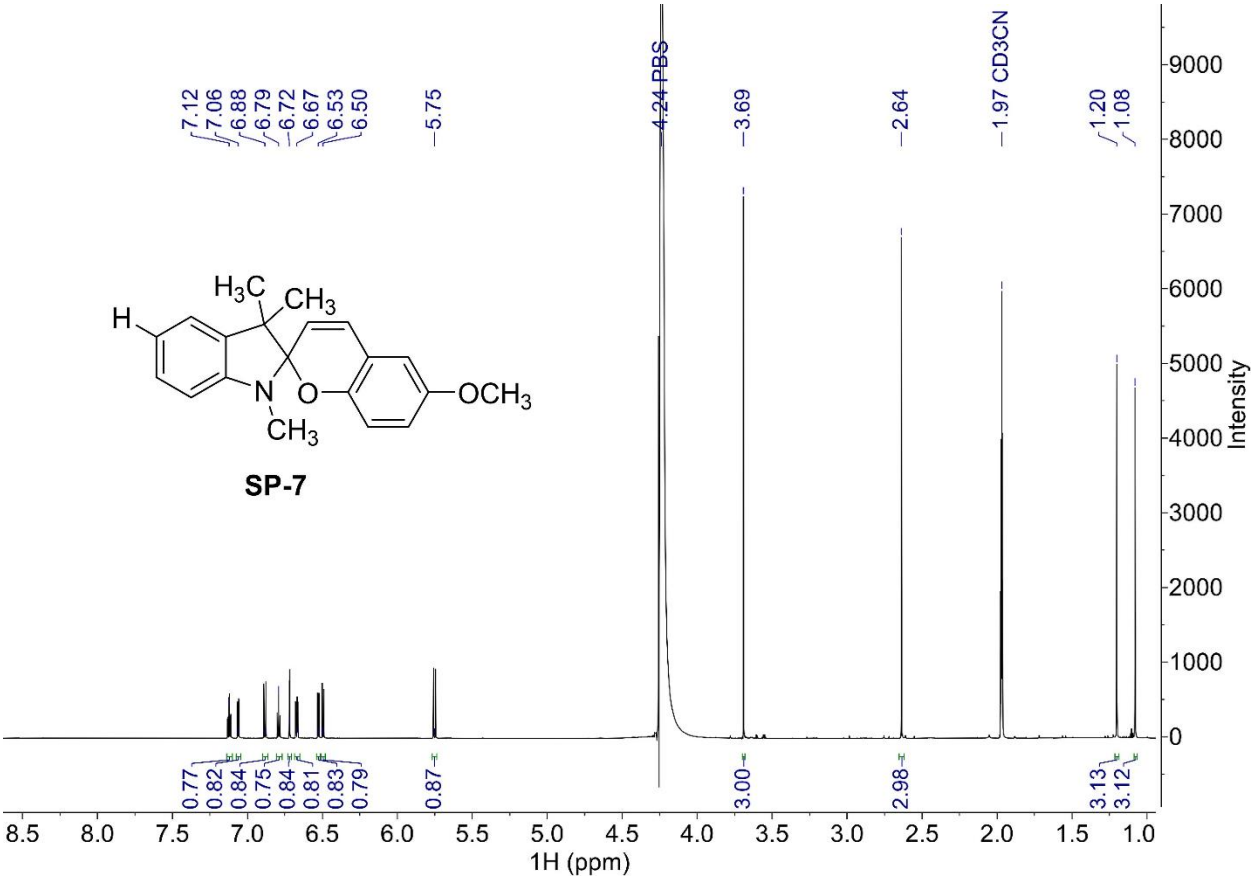

Figure 3.9. *^{1}H NMR of 5 mM SP-7 in deuterated acetonitrile/phosphate buffered saline (PBS, 1X, pH 7.4) (1:1 v/v).*

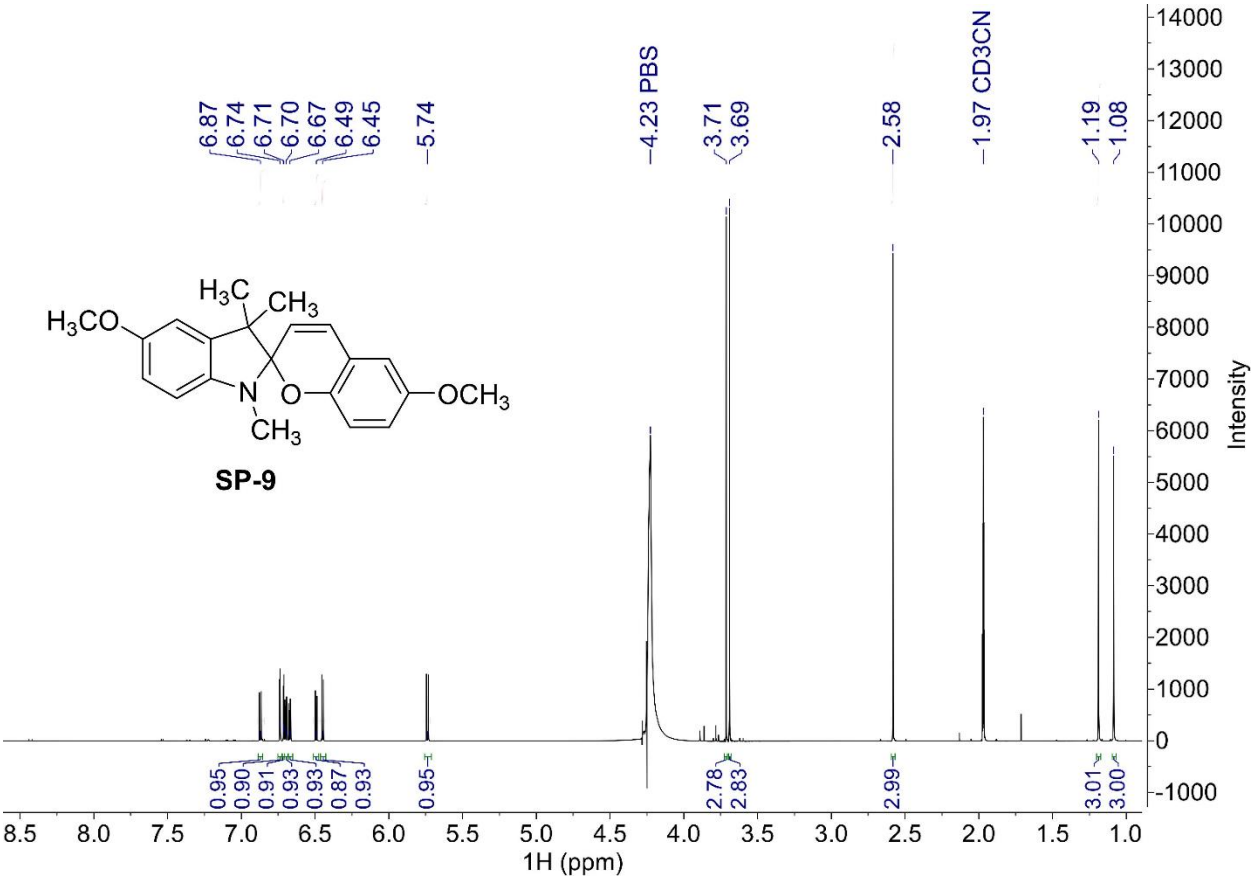

Figure 3.10. *^{1}H NMR of 5 mM SP-9 in deuterated acetonitrile/phosphate buffered saline (PBS, 1X, pH 7.4) (1:1 v/v).*

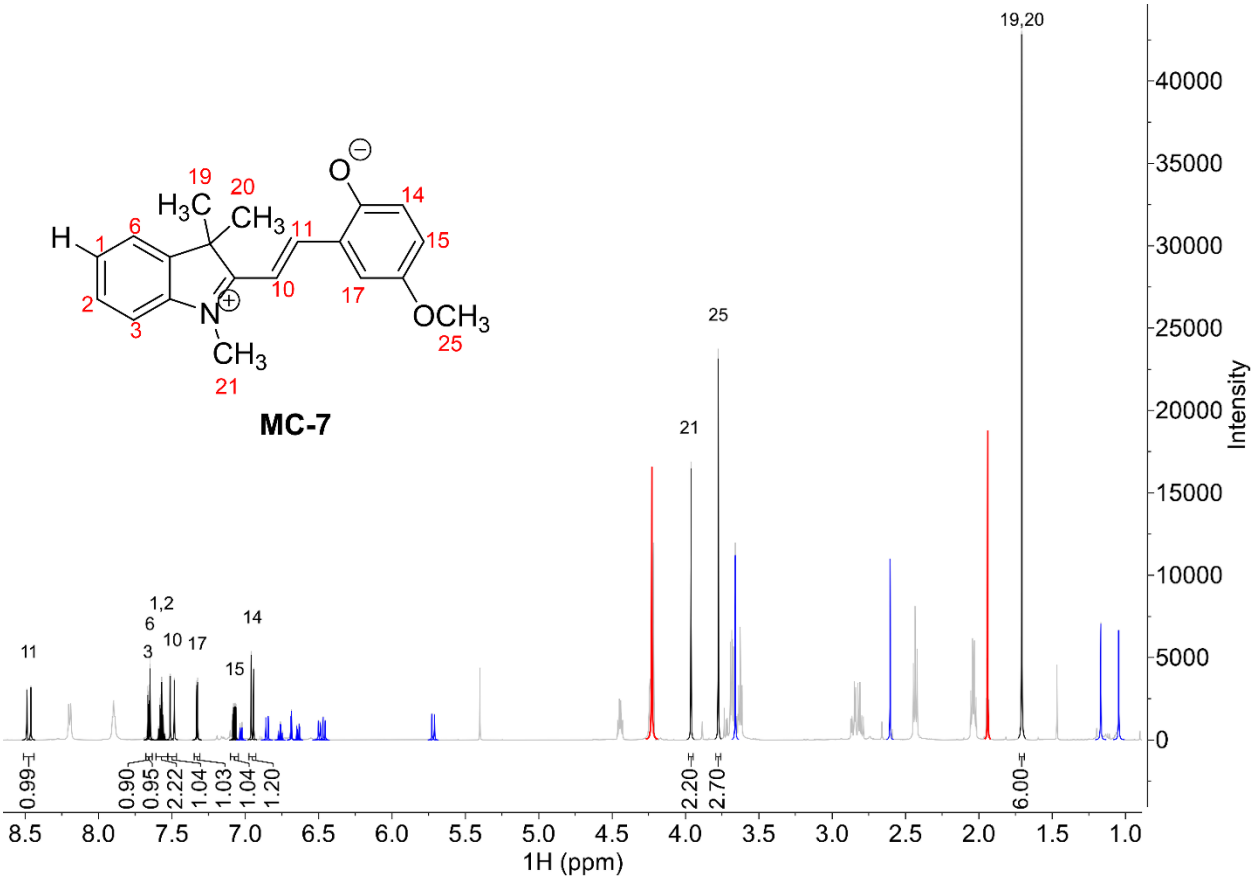

Figure 3.11. *^{1}H NMR spectrum of GSH-stabilized **MC-7**. **MC-7** (black), SP-7 (blue), GSH (grey), CD_3CN reference (red). The **MC-7** species was induced using 15 mM SP-7 and GSH in equimolar concentration in deuterated acetonitrile/phosphate buffered saline (PBS, 1X, pH 7.4) (1:1 v/v).*

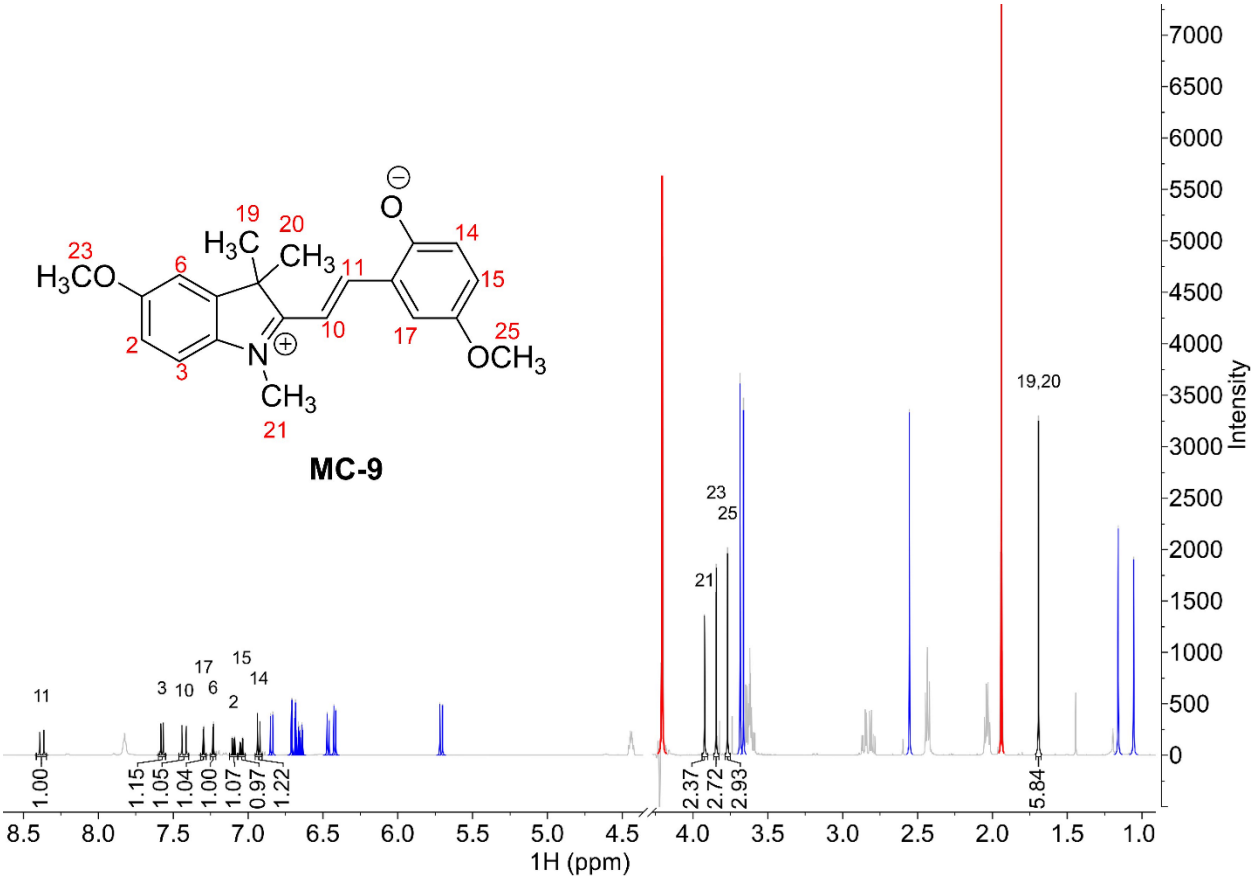

Figure 3.12. *^{1}H NMR spectrum of GSH-stabilized **MC-9**. **MC-9** (black), SP-9 (blue), GSH (grey), CD_3CN reference (red). The **MC-9** species was induced using 5 mM SP-9 and GSH in equimolar concentration in deuterated acetonitrile/phosphate buffered saline (PBS, 1X, pH 7.4) (1:1 v/v).*

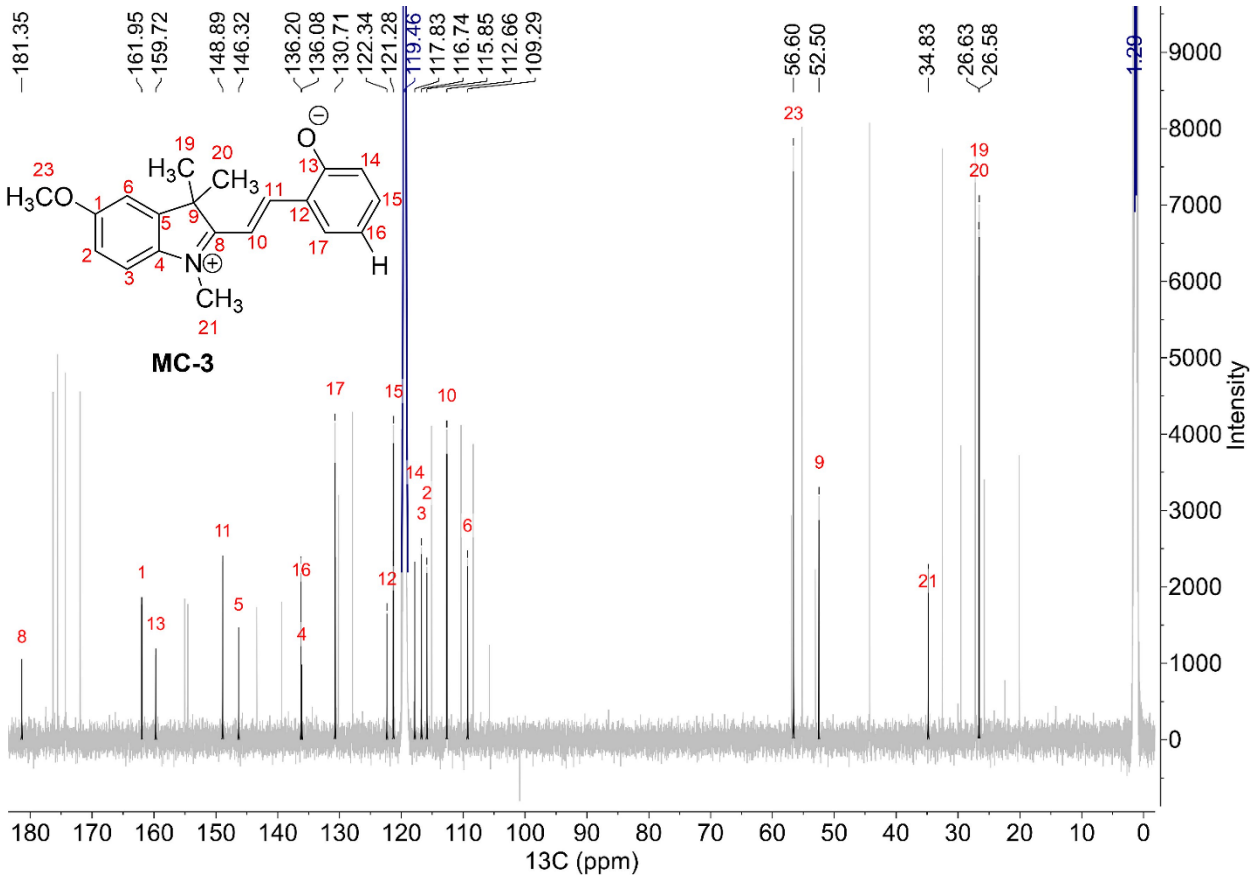

Figure 3.13. *^{13}C NMR of GSH-stabilized **MC-3**. The **MC-3** species was induced using 5 mM SP-3 and GSH in equimolar concentration in deuterated acetonitrile/phosphate buffered saline (PBS, 1X, pH 7.4) (1:1 v/v).*

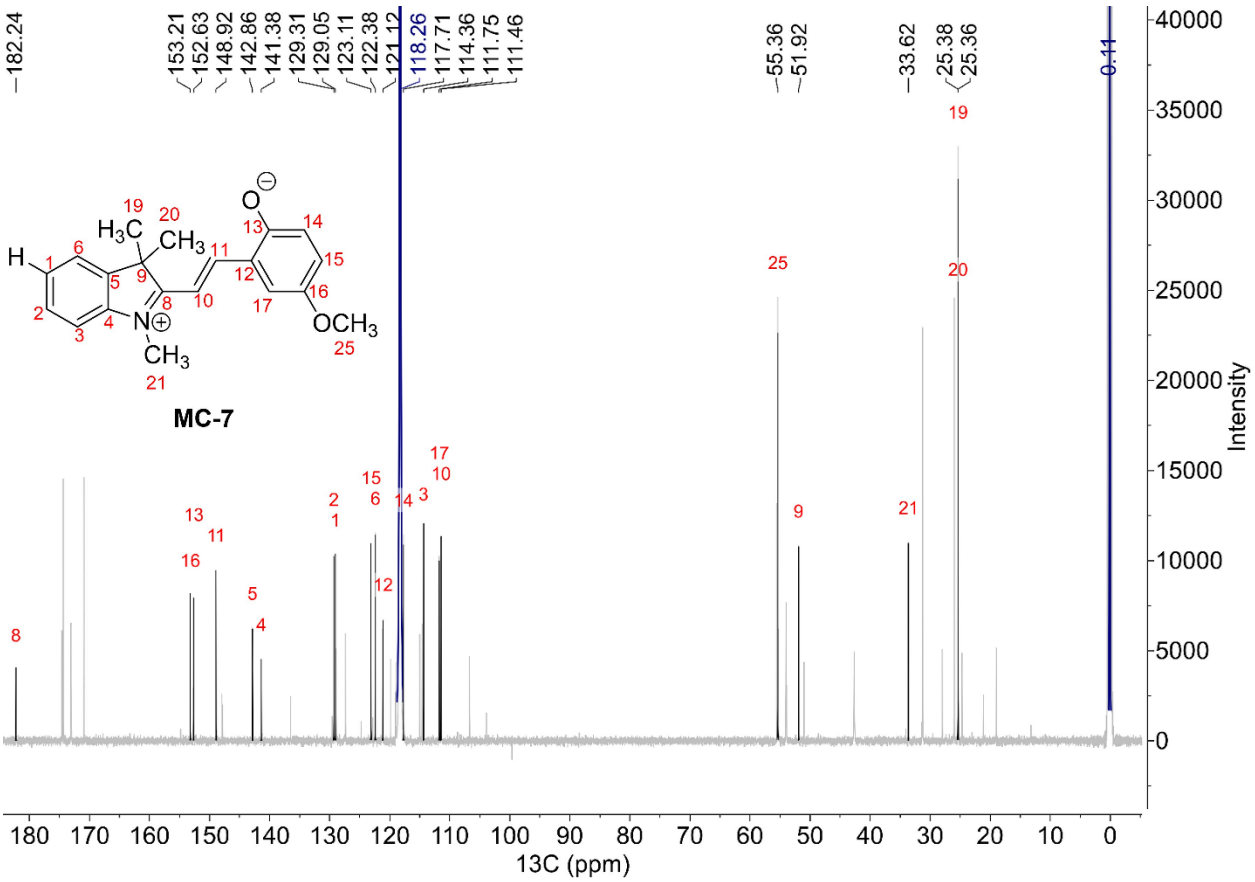

Figure 3.14. *^{13}C NMR of GSH-stabilized **MC-7**. The **MC-7** species was induced using 15 mM SP-7 and GSH in equimolar concentration in deuterated acetonitrile/phosphate buffered saline (PBS, 1X, pH 7.4) (1:1 v/v).*

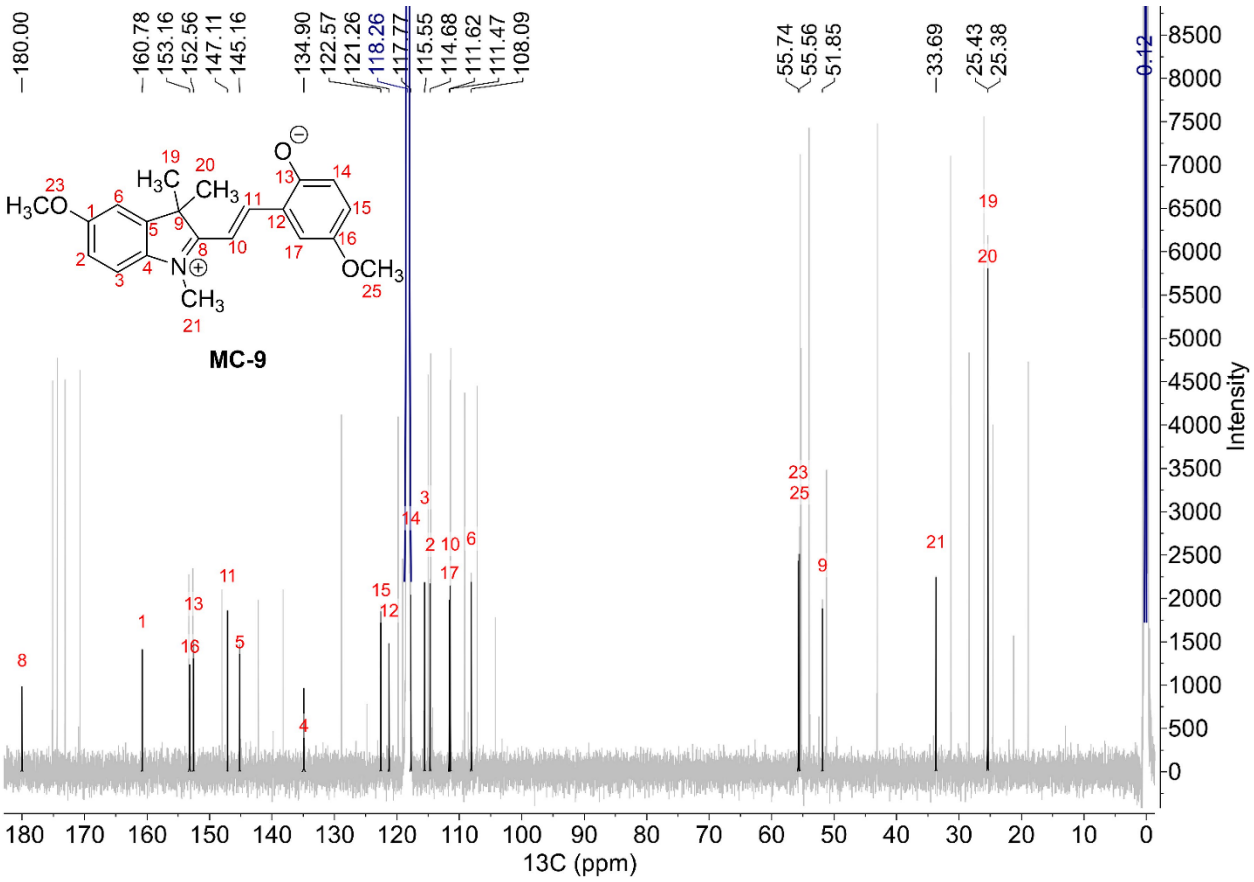

Figure 3.15. *^{13}C NMR of GSH-stabilized **MC-9**. The **MC-9** species was induced using 5 mM SP-9 and GSH in equimolar concentration in deuterated acetonitrile/phosphate buffered saline (PBS, 1X, pH 7.4) (1:1 v/v).*

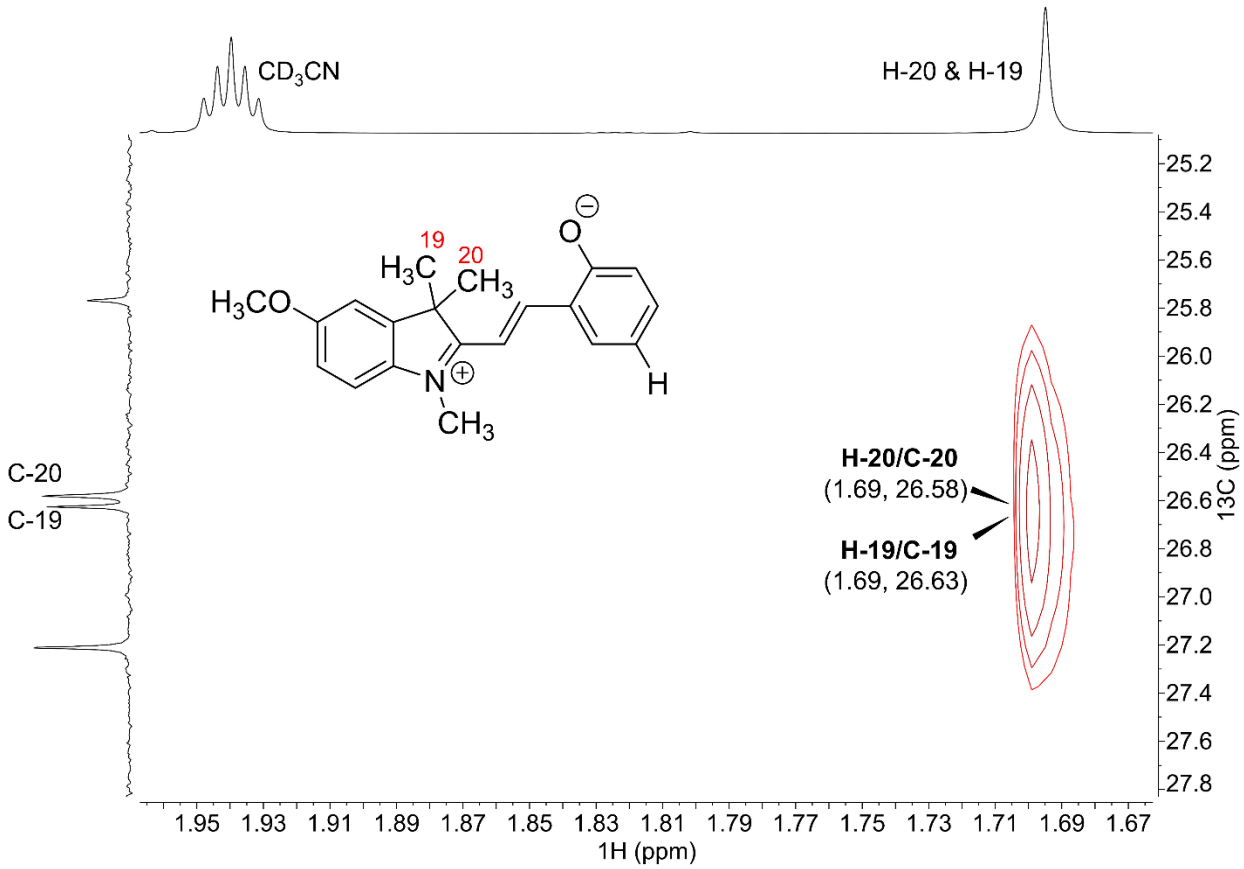

Figure 3.16. *HSQC-NMR spectrum of GSH-stabilized* ***MC-3****. Single-bond correlation of proton H-19 (1.69 ppm) to carbon C-19 (26.63 ppm) and proton H-20 (1.69 ppm) to carbon C-20 (26.58 ppm). X-axis represents* ^{1}H *and y-axis represents* ^{13}C*.*

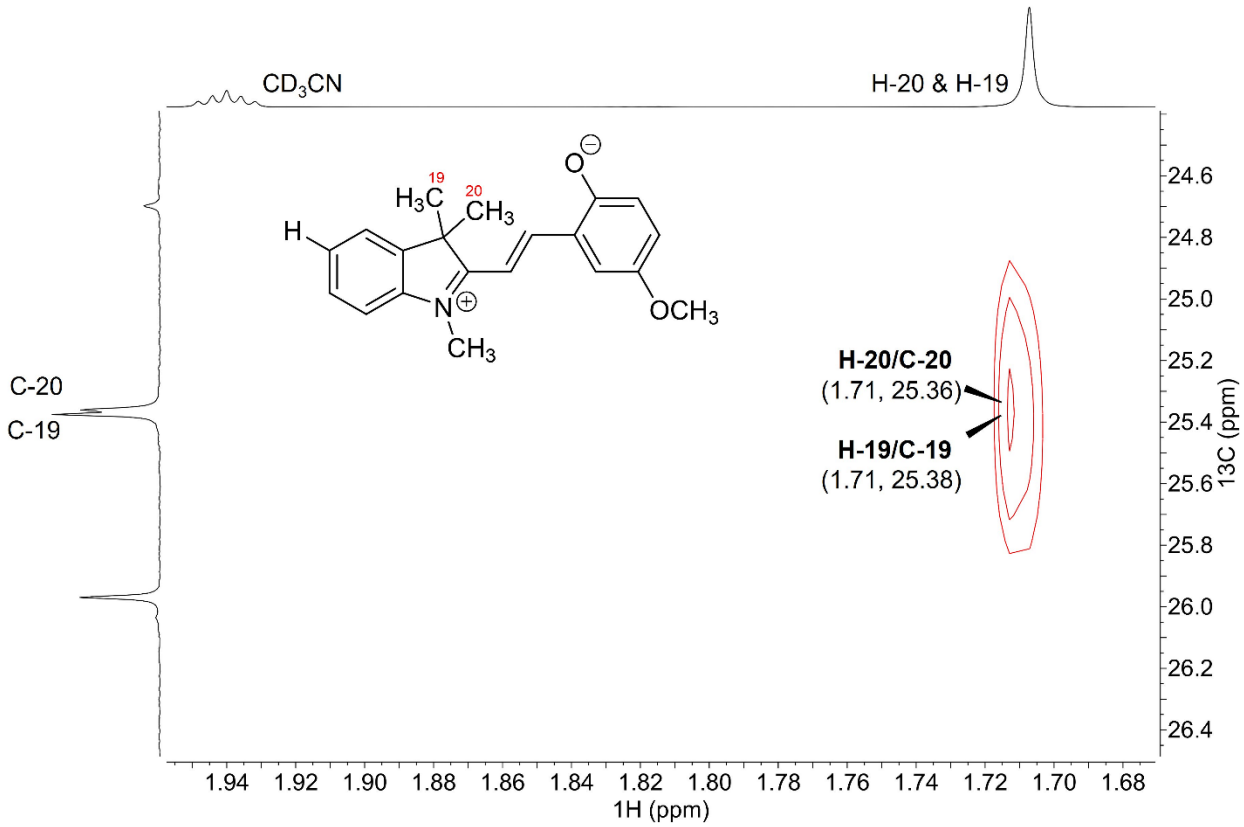

Figure 3.17. *HSQC NMR spectrum of GSH-stabilized* ***MC-7****. Single-bond correlation of proton H-19 (1.71 ppm) to carbon C-19 (25.38 ppm) and proton H-20 (1.71 ppm) to carbon C-20 (25.36 ppm). X-axis represents* ^{1}H *and y-axis represents* ^{13}C*. The* ***MC-7*** *species was induced using 15 mM SP-7 and GSH in equimolar concentration in deuterated acetonitrile/phosphate buffered saline (PBS, 1X, pH 7.4) (1:1 v/v).*

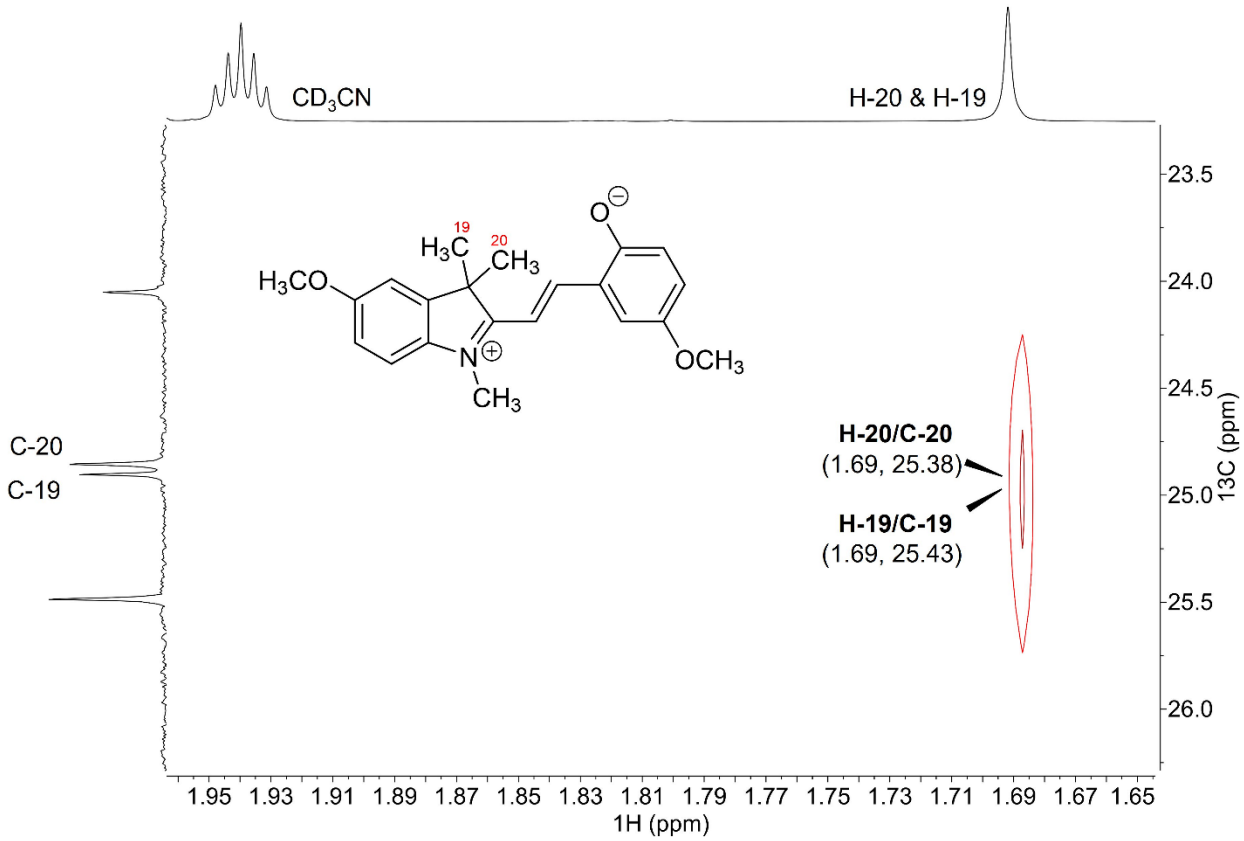

Figure 3.18. *HSQC-NMR spectrum of GSH-stabilized* ***MC-9****. Single-bond correlation of proton H-19 (1.69 ppm) to carbon C-19 (25.43 ppm) and proton H-20 (1.69 ppm) to carbon C-20 (25.38 ppm). X-axis represents* ^{1}H *and y-axis represents* ^{13}C*. The* ***MC-9*** *species was induced using 5 mM SP-9 and GSH in equimolar concentration in deuterated acetonitrile/phosphate buffered saline (PBS, 1X, pH 7.4) (1:1 v/v).*

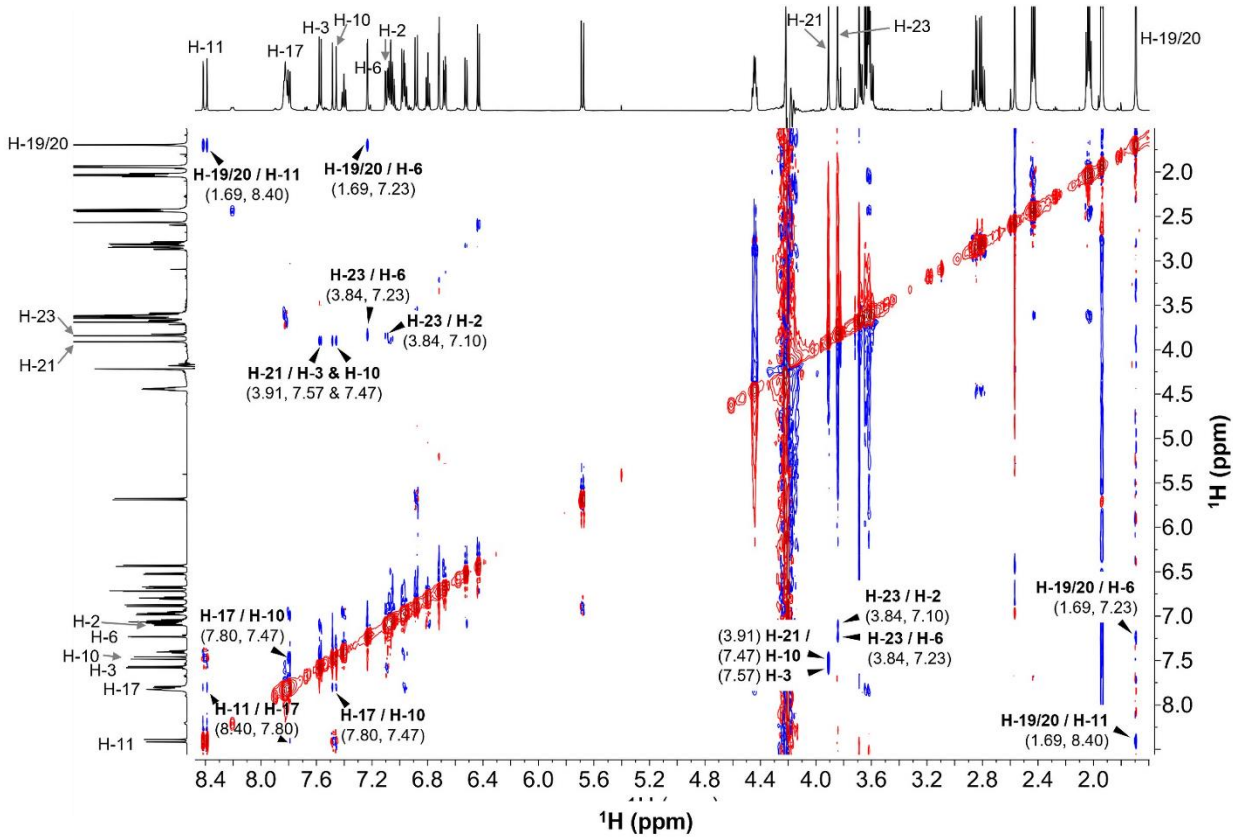

Figure 3.19. *Full NOESY spectrum of GSH-stabilized* ***MC-3***. *The* ***MC-3*** *species was induced using 5 mM SP-3 and GSH in equimolar concentration in deuterated acetonitrile/phosphate buffered saline (PBS, 1X, pH 7.4) (1:1 v/v).*

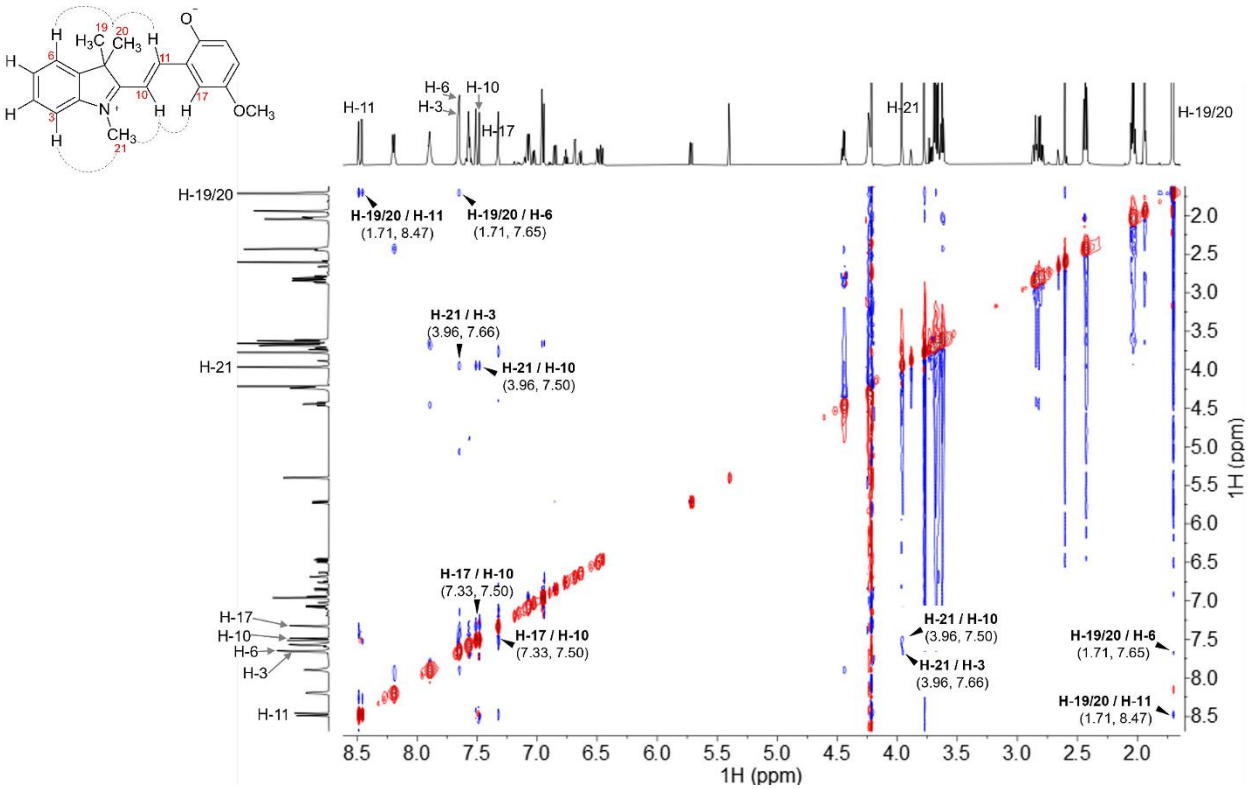

Figure 3.20. *NOE correlations (dashed lines) and NOESY NMR spectrum of GSH-stabilized* ***MC-7****. The* ***MC-7*** *species was induced using 15 mM SP-7 and GSH in equimolar concentration in deuterated acetonitrile/phosphate buffered saline (PBS, 1X, pH 7.4) (1:1 v/v).*

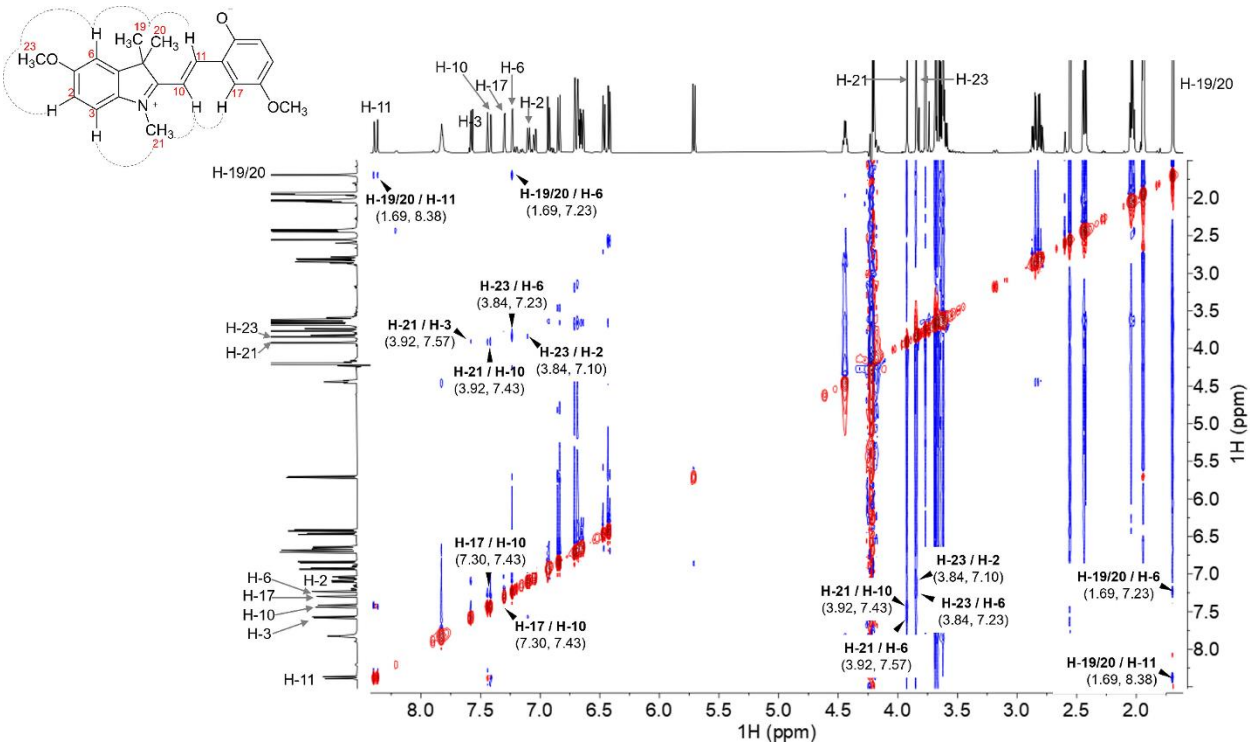

Figure 3.21. *NOE correlations (dashed lines) and NOESY spectrum of GSH-stabilized* ***MC-9****. The* ***MC-9 s****pecies was induced using 5 mM SP-9 and GSH in equimolar concentration in deuterated acetonitrile/phosphate buffered saline (PBS, 1X, pH 7.4) (1:1 v/v).*

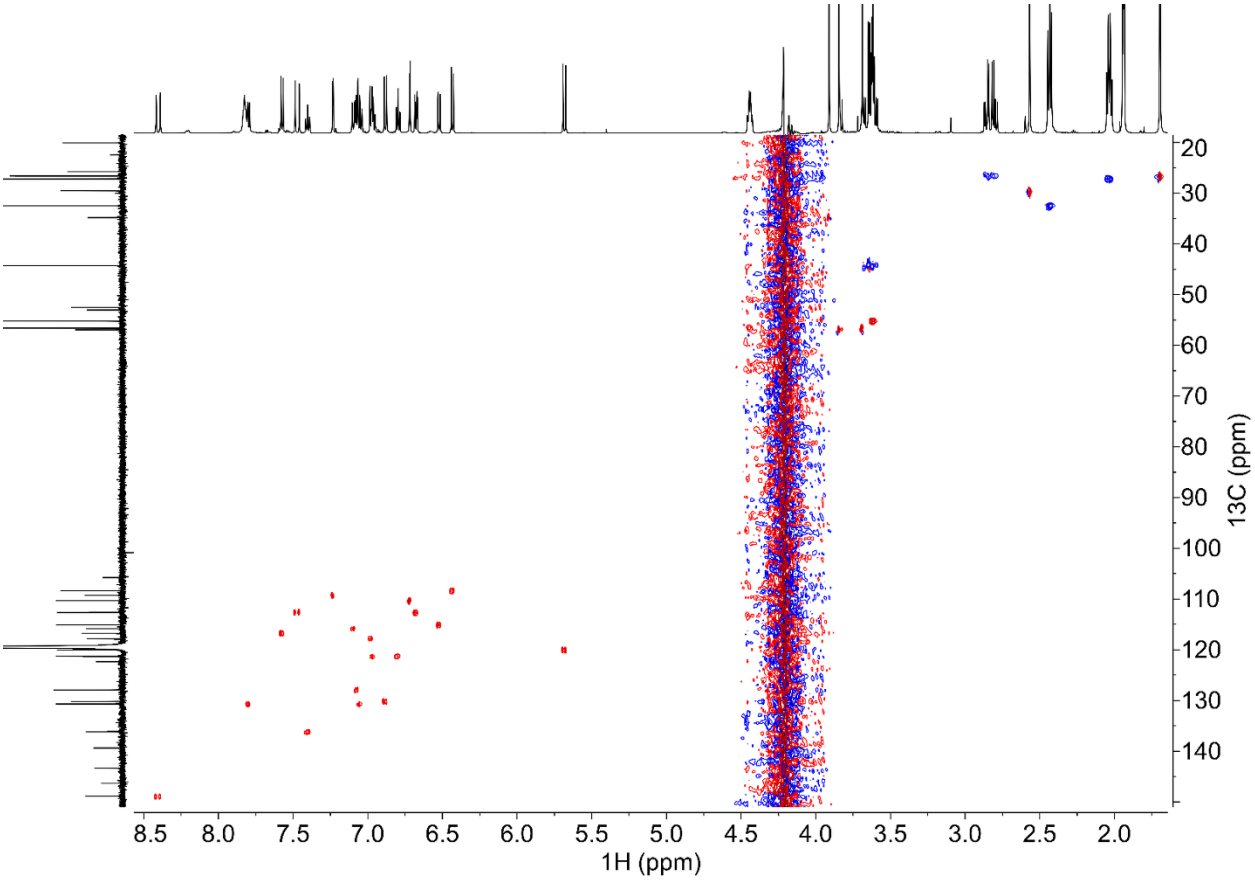

***Figure 3.22**. HSQC spectrum of GSH-stabilized **MC-3**. The **MC-3** species was induced using 5 mM SP-3 and GSH in equimolar concentration in deuterated acetonitrile/phosphate buffered saline (PBS, 1X, pH 7.4) (1:1 v/v).*

CHAPTER 4: SPIROPYRAN AS AN ACTIVATABLE MRI CONTRAST AGENT FOR GLUTATHIONE

4.1 BACKGROUND ON MRI

4.1.1 BASIC PRINCIPLES

Magnetic Resonance Imaging (MRI) is a powerful tool that is non-invasive, non-ionizing and provides the ability to view detailed images and localization of soft tissues in the body. MRI employs similar principles to nuclear magnetic resonance (NMR) and the following simplified description for basic principles, T_1- and T_2-weighted imaging and T_1 contrast agents can be read in further detail.[215–220] In general, the nuclei being studied should contain an odd mass number and spin of $^1/_2$, $^3/_2$, or $^5/_2$ etc. to create a net magnetic moment when applied to an external magnetic field. For example, the hydrogen nuclei has a net charge of 1 and a spin of ½ and will be represented as the sphere in Figure 4.1. When an external magnetic field is applied (B_o), it creates a net magnetic moment (vector μ), to align the hydrogen nuclei to the external magnetic field. Since the net magnetic moment is not completely aligned with the magnetic field due to torque and angular momentum (mass, velocity, and radius),[221–223] the nuclei will precess around Bo with a precessional frequency i.e., Larmor frequency and is governed by the equation $\omega_o = B_o \times \gamma$. Where ω_o = Larmor frequency, B_o = external magnetic field, and γ = gyro-magetic ratio. Furthermore, a frequency must be used, usually a radio frequency (RF), that matches the Larmor frequency for the nuclei of interest to cause absorption of the RF energy resulting in a flip of the net magnetic vector away from the external magnetic field resulting in excitation. The amplitude and duration of the RF pulse dictates the degree of the flip angle of the net magnetic vector, but for simplicity, the flip angle will be defined as a 90° to the external magnetic field. Once the RF pulse is completed, the net magnetic vector will want to re-align back to the external magnetic field, resulting in relaxation (dashed arrow). This creates a free induction decay (FID) of the relaxation over time and a Fourier transform is performed on the FID to generate a spectrum. The main

difference between MRI and NMR is MRI employs magnetic field gradients in the X, Y, and Z plane to selectively modulate the magnetization in a specified area to generate 2D image slices in the transverse, sagittal or coronal plane.

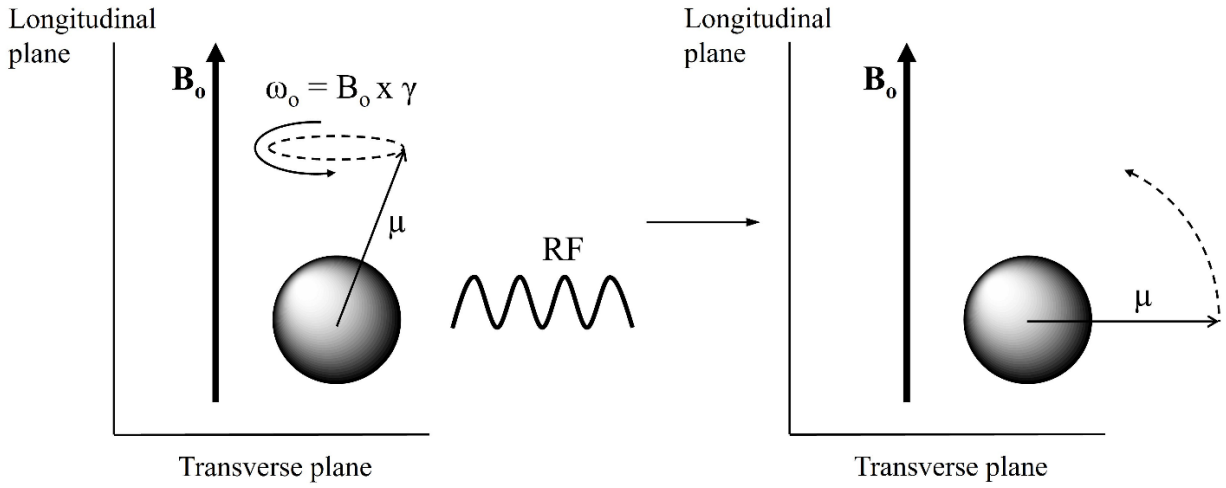

Figure 4.1. *Basic principles on how an NMR spectrum is generated. The net magnetic vector (μ) of the hydrogen nuclei will align when exposed to an external magnetic field (B_0). Due to torque and angular momentum, the hydrogen nuclei it will precess with a frequency termed Larmor frequency (ω_o). When a radiofrequency (RF) is applied that matches the ω_o of the hydrogen nuclei it will induce a spin flip of the μ with an angle of* 90° *to the external magnetic field. When the RF pulse is turned off, the μ will relax back to the B_o, which generates a free induction decay (FID). A Fourier transform is then performed on the FID to generate a spectrum.*

4.1.2 T_1- VS T_2-WEIGHTED IMAGING

Since the abundance of hydrogen in the human body is ~ 88 M,[222] MRI takes advantage of the high proton concentration to provide contrast between different tissues. This is done by observing either the T_1 (longitudinal) relaxation time or the T_2 (transverse) relaxation time in tissues. T_1 relaxation time is described by the time the excited protons recover their longitudinal

magnetization and realigns with the external magnetic field. As shown in Figure 4.1, where the x-axis is the transverse plane and the y-axis is the longitudinal plane, after the RF pulse is concluded and the 90˚ spin flip is achieved, the net magnetic vector is aligned with the transverse plane. A T_1 recovery curve can then be extrapolated from the time it takes for ~63% of the longitudinal magnetization to return to the external magnetic field in the longitudinal plane (Figure 4.2A). Moreover, T_2 relaxation is described by the time the excited protons decay and lose their transverse magnetization due to dephasing from the interactions of adjacent spins or external magnetic field inhomogeneities. A T_2 decay curve can then be extrapolated from the time it takes for ~63% of transverse magnetization to be lost (or to decay to ~37%) in the transverse plane as it realigns to the external magnetic field in the longitudinal plane (Figure 4.2B).

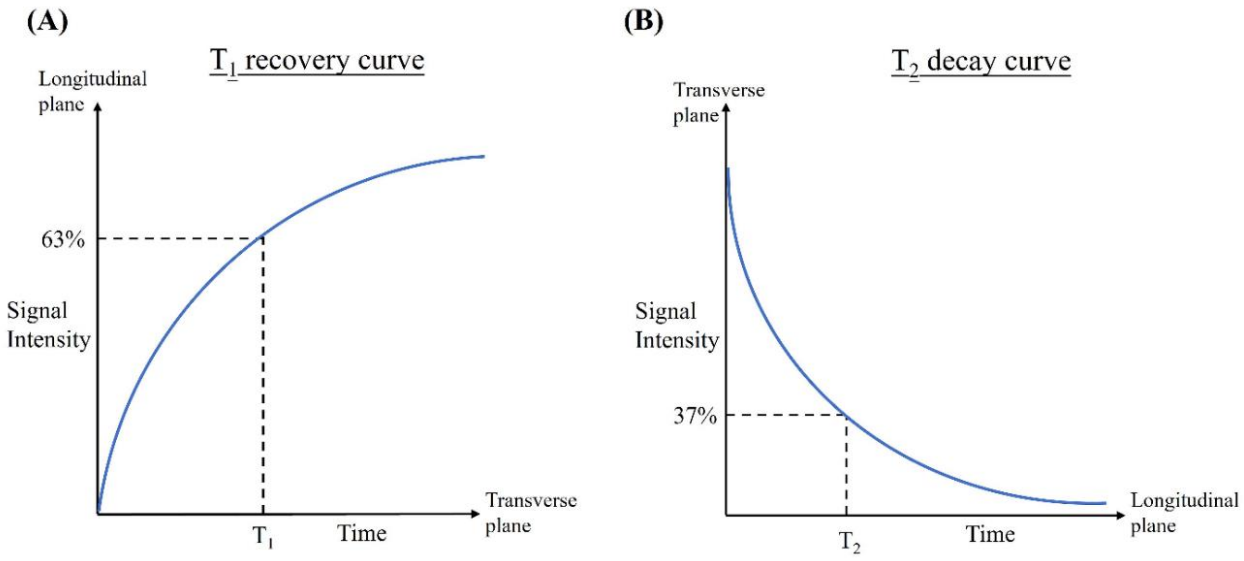

Figure 4.2. *(A) T_1 recovery curve and (B) T_2 decay curve. T_1 relaxation results when ~63% of the longitudinal magnetization has recovered to the external magnetic field (B_o). T_2 relaxation results when ~37% of the transverse magnetization is lost due to dephasing as it decays and realigns to external magnetic field (B_o).*

T_1- and T_2-weighted imaging considers various tissue in the body e.g., cerebral spinal fluid (CSF), cortex (grey matter, GM) and white matter (WM) contain different T_1 and T_2 relaxation times that can be modified by altering the repetition time (TR) and echo times (TE). TR is the time between each RF pulse, while TE is the time between the RF pulse and when the signal is gathered. To enhance T_1-weighted images the TR must be short to ensure full relaxation is not achieved and thus generating "positive" or "bright" contrast in the T_1 domain; The shorter the T_1 the brighter the signal in the image. Additionally, the TE must also be short to diminish the T_2 signal. For T_2-weighted images, enhancement of the T_2 signal is done by utilizing a long TE to provide enough time to ensure relaxation decay is achieved and thus generating "negative" or "dark" contrast in the T_2 domain: The shorter the T_2 the darker the signal in the image. Furthermore, the TR must also be long to diminish the T_1 signal. Once these parameters are established, contrast between tissues such as WM, GM, CSF can be observed in either T_1-weighted or T_2-weighted imagining (Figure 4.3). As shown in Figure 4.3A & B where the chosen contrast is T_1-weighted, WM has a short T_1 time and is light grey in the T_1-weighted image, GM has a medium T_1 time and is grey in the T_1-weighted image, and CSF has a long T_1 time and is dark grey in the T_1-weighted image. In Figure 4.3C & D where the chosen contrast is T_2-weighted, the T_2 times from shortest to longest maintains the same order, (WM = short T_2 time, GM = medium T_2 time, and CSF = long T_2 time), however the contrast is reversed (WM = dark grey, GM = grey, and CSF = bright). The CSF exhibits a dark signal in the T_1-weighted image and bright signal in the T_2-weighted image because water has a long T_1 and T_2 time due to the fast molecular tumbling rate, which hinders the energy exchange (T_1) and spin-spin interaction (T_2) resulting in slower relaxation. As the tissue in the brain gets "fattier", GM to WM, this slows the molecular tumbling time and allows for energy

exchange (T_1) and spin-spin interaction (T_2) resulting in faster relaxation and generation of brighter T_1 signal or darker T_2 signal.

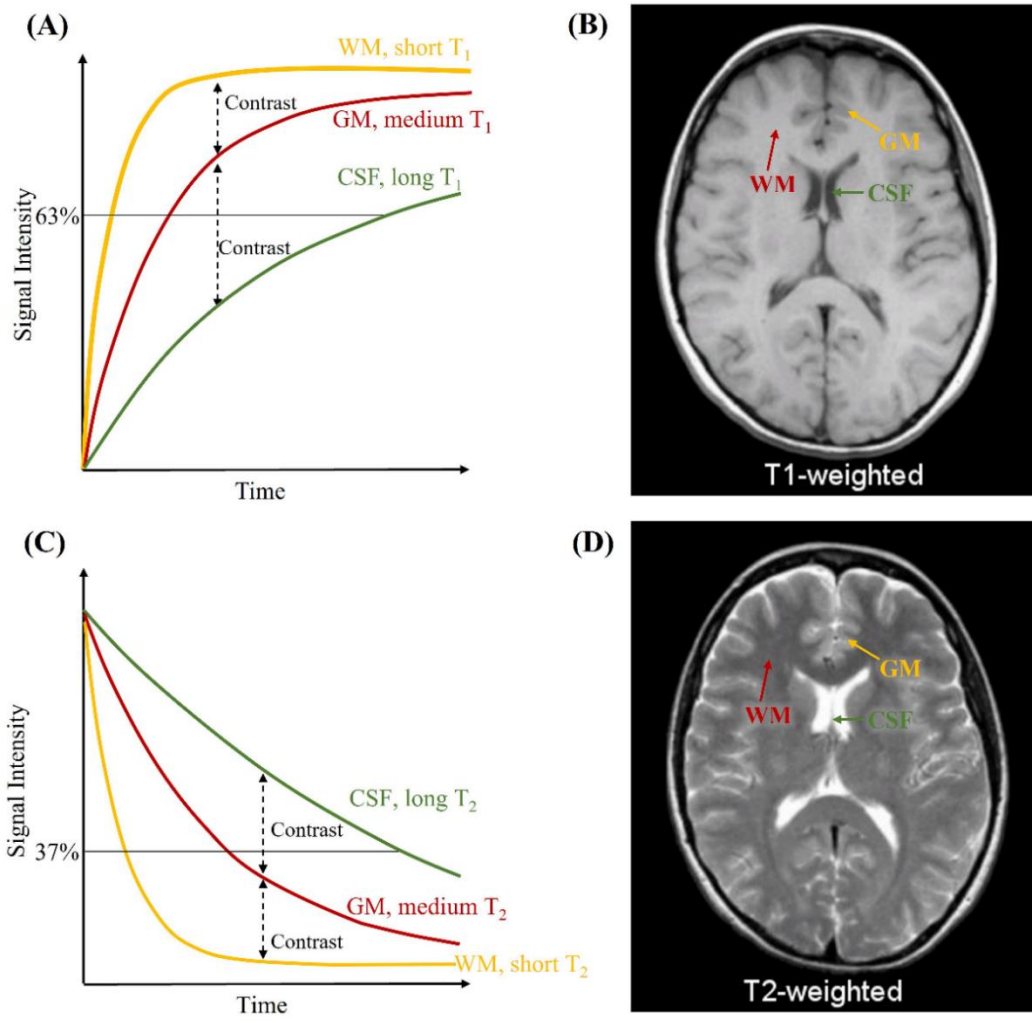

Figure 4.3. *(A) T_1-weighted recovery curve resulting in (B) T_1-weighted image of the human brain in the transverse plane. (C) T_2-weighted decay curve resulting in (D) T_2-weighted image of the human brain in the transverse plane. Translation of T_1 and T_2 times to the T_1 and T_2 signal in the weighted images: White matter (WM) = short T_1 and T_2 time; light grey T_1 signal, and dark grey T_2 signal; grey matter (GM) = medium T_1 and T_2 time; grey T_1 signal and T_2 signal; cerebral spinal fluid (CSF) = long T_1 and T_2 time; dark grey T_1 signal and bright T_2 signal. T_1- and T_2-weighted images taken from MRI basics.*[224]

4.1.3 T_1 CONTRAST AGENTS

Sometimes it is difficult to distinguish contrast between different tissues and therefore the usage of a contrast agent is needed. In general, T_1- contrast agents provide "bright" contrast wherever the agent is localized, and this is due to dipole-dipole interactions between the contrast agent and the nearby water protons to enhance the signal. Clinically employed contrast agents use gadolinium ion (Gd^{3+}) to provide contrast. Gd^{3+} is most commonly used because it contains 7 unpaired electrons and this paramagnetism provides a strong magnetic moment, which induces nearby water protons to relax faster. In addition, the low molecular weight of the Gd^{3+}-based T_1 contrast agents allows them to exist in the extracellular fluid and distribute to tumor lesions,[225,226] to the brain,[227,228] or to the heart[229–231] etc. Figure 4.4 shows an image of the human brain in the transverse plane of a patient with glioblastoma.[232] When a T_1-weighted MR image on the left is conducted with no contrast agent, it is difficult to discern if there are any abnormalities in the brain. When the Gd^{3+} contrast agent (gadoteridol) is administered, figure on the right, is it evident there is a tumor present in the brain by the brightening of the area.

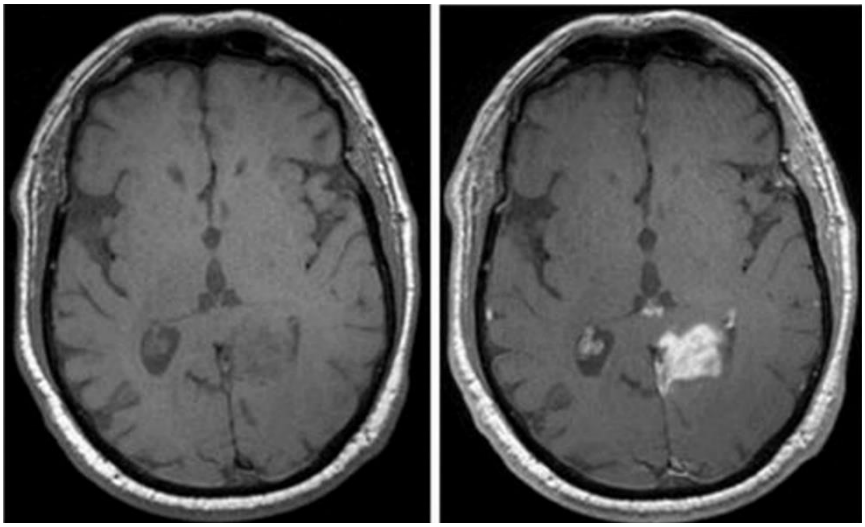

Figure 4.4. *A T_1-weighted MR image in the transverse plane of the human brain before (left) and after (right) administration of a Gd^{3+} contrast agent (gadoteridol), to a patient with glioblastoma.*

Brightening of the area in the right image suggest there is a tumor present. Reproduced with permission from [232]. Copyright 2013 Radiological Society of North America (RSNA®).

In order to compare T_1 contrast agents to each other and to assess their effectiveness in enhancing signal contrast, the relaxivity (r_1) is used to normalize the relaxation rate ($1/T_1$) as a function of concentration of the contrast agent at a specific temperature and field strength. Relaxivity can be calculated by varying the concentration of the contrast agent and determining the T_1 times at each concentration. Inverting the T_1 times at each concentration and fitting it to a linear line generates a slope that reflects the relaxivity in units of [$mM^{-1}s^{-1}$]. The higher the relaxivity results in better signal enhancement. There are three parameters to affect relaxivity in the inner sphere: (1) the water hydration state (q). Increasing the amount of water directly bound to the metal will increase the relaxivity. (2) the molecular tumbling time (τ_R). Increasing the size of the molecule will slow down the tumbling time and allows for better energy exchange, therefore increasing relaxivity. (3) the water exchange rate of the coordinated water ($1/\tau_M$). The faster the exchange rate of water enables more water to be relaxed, resulting in higher relaxivity. Modifying these parameters provide a means to skillfully expand on the field of activatable contrast agents.

4.1.4 ACTIVATABLE CONTRAST AGENTS

While the clinically utilized Gd^{3+} contrast agents work well in generating contrast to discern ambiguous regions, they do not provide specificity for molecular imagining because signal contrast is only achieved in the areas they are located. Therefore, the use of activatable contrast agents are of interest. Activatable contrast agents produce contrast when exposed to a stimulus that consequently alters the agent and converts them to their "active" form. To date, there have been several reported activatable contrast agents responding to light,[233–236] enzymes,[237–239] pH,[240–243]

glutathione,[244–246] metal ions[247–249] etc. An example of a light-activatable contrast agent developed by our group[235] utilized a dinitrospiropyran for its photoswitching capability and conjugated it to a Gd^{3+}-DO3A chelator. In the dark, the dinitrospiropyran is stable in the "open" merocyanine (MC) form and is red in solution with a relaxivity of 2.51 $mM^{-1}s^{-1}$. When MC-Gd^{3+}-DO3A is irradiated with visible light, MC isomerizes to the "closed" spiropyran (SP) form and is pale yellow in solution. The relaxivity decreases to 2.05 $mM^{-1}s^{-1}$ and this 18% decrease in relaxivity is hypothesized to be due the change in the hydration state (q) of Gd^{3+} metal center. Initially, in the MC form, the Gd^{3+} metal center has a q =1.16 determined by ^{17}O NMR. Upon irradiation with visible light, isomerization from "open" to "closed" causes rearrangement and loss of the phenolic oxygen producing an "indoline cap" that prevents access of water by Gd^{3+}, decreasing q = 0.44. Although the limiting factor of light activatable contrast agents is the depth of light penetration, the usage for cell tracking *in vitro* could be a potential application for these agents.

4.2 THE IMPORTANCE OF GLUTATHIONE IN HUMAN DISEASE

4.2.1 GSH VARIANCE IN BENIGN VS MALIGNANT TUMORS

Glutathione (GSH) is a primary intracellular and extracellular antioxidant that plays a vital role in cell homeostasis by scavenging for reactive oxygen species (ROS). GSH is present in the human body with concentrations around 0.5-10 mM intracellularly[166–168] and 2-20 μM extracellularly.[169,170] The antioxidant activity of GSH is largely due to the thiol residue on cysteine that allows GSH to act as an electron donor to be oxidized to glutathione disulfide (GSSG). Reduction of GSSG and regeneration of GSH is possible by means of glutathione reductase.[174] Excess generation of ROS has been shown to induce oxidative stress causing alterations in the levels of GSH, and fluctuations in the concentration of GSH has been directly linked to diseases

such as Alzheimer's,[250–253] diabetes,[254–256] and cancer.[257–260] In Alzheimer's and diabetes depletion of GSH is observed and is thought to be a result of oxidative stress by ROS and reactive nitrogen species (RNS) causing DNA damage and mitochondrial dysfunction[261–263] However, GSH concentrations vary for certain cancers such as breast, ovarian, lung. For example there are higher levels of GSH in breast tumors and lower levels of GSH in brain and liver tumors compared to disease free tissues.[258] Tumor hypoxia and acidosis are a few characteristics that reflect the tumor environment and have shown to affect the redox status in breast tumors with an increased concentration of GSH.[264–266] Furthermore, in regards to GSH in breast cancer, there have been studies showing heterogeneity in GSH levels for malignant tumors while benign tumors displayed a more homogeneous GSH concentration.[267–269] The malignant tumors contained lower GSH concentrations in the core while towards the periphery this concentration increased.[270] This unique GSH variance in benign vs malignant breast tumors could provide the ability to assess tumor aggressiveness.

4.2.2 METHODS TO DETECT GSH

As vital as GSH is, there has been a lack of *in vivo* tools for monitoring GSH levels. Current methods using HPLC have high specificity in detecting GSH in the blood. However, slow sample prep is an issue due to chemical derivatization to prevent unintentional oxidation of GSH.[271,272] In addition, as a result of the extraction of plasma, there is no localization of the diseased area.[273] Magnetic Resonance Spectroscopy (MRS) is a non-invasive method to measure metabolically relevant biological compounds, such as GSH. However, due to the severe spectral overlap with other metabolites, it is difficult to distinguish GSH.[274] An alternative and most employed method to characterize a tumor is through a tissue biopsy, which is highly invasive. Therefore, Magnetic Resonance Imaging (MRI) provides an attractive option because it is non-invasive, non-ionizing

and can image deep tissue. However, MRI has no specificity towards GSH. The application of molecular imaging of GSH would provide a powerful tool by delivering information about tissues at a cellular and molecular level. For this reason, molecular imaging has become an emerging field, and there has been increased effort to build a biosensor for GSH detection. Several sensors have been synthesized[275–279] but very few sensors have been successfully applied *in vivo* in combination with MRI. To date, two MRI agents responsive to GSH have been developed for dual imaging, $MnSiO_3$@Fe_3O_4 for T_1/T_2-weighted MRI[280] and ^{99m}Tc-labeled Fe_3O_4 for T_2-weighted MRI/single photon emission computerized tomography (SPECT)[281] as a theranostic. The use of T_2-weighted imaging could be a limitation due to the dark contrast and could interfere with the T_1-weighted signal. The utilization of MRI as a modality for molecular imaging of GSH is an appealing option because it will allow us to examine the fluctuations in GSH levels. This will have a profound impact on our ability to assess tumor state.

4.3 SPIROPYRAN AS A GLUTATHIONE SENSOR

Molecular switches such as spiropyrans (SP) have shown the ability to sense GSH.[54,179,180,184–188] Using a library of spiropyran photoswitches (SP-1 – SP-9) previously synthesized by others in our group, where the functional groups were altered on the indoline and chromene moieties to reflect diverse electronic effects, such as electron donating (OCH_3), electron withdrawing (NO_2) or neutral (H) groups,[153] it was found that four SP's (SP-1, SP-3, SP-7, and SP-9) were responsive to GSH.[179] These SP's (0.5 mM, EtOH/H_2O, pH = 7.4) isomerized to merocyanine (MC) in the presence of equimolar concentration of GSH and this process was reversible when irradiated with visible light (Scheme 4.1). Interestingly, SP-3, SP-7, and SP-9 all contained at least one methoxy while SP-1 bore the neutral proton on each chromene and indoline end.

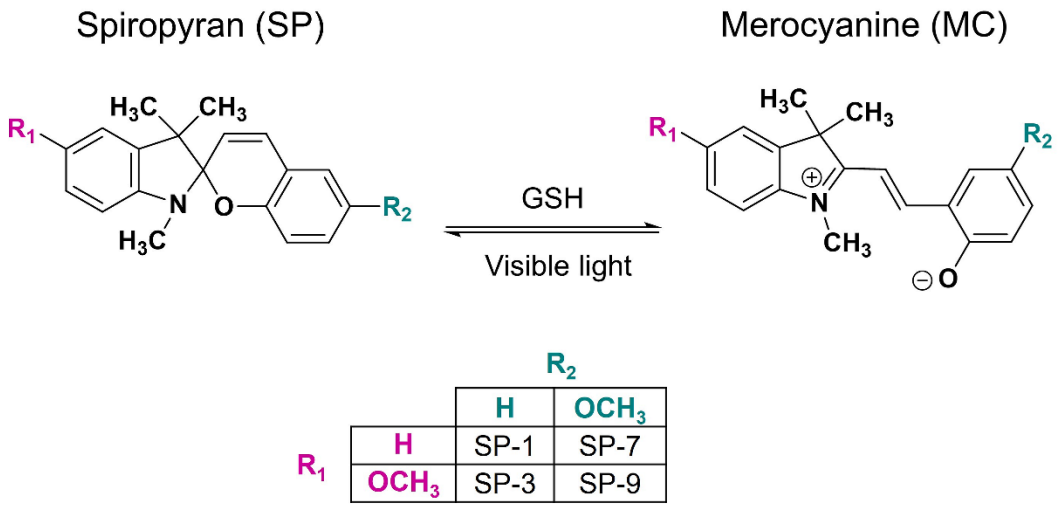

R_1 \ R_2	H	OCH_3
H	SP-1	SP-7
OCH_3	SP-3	SP-9

Scheme 4.1. *Proposed spiropyran isomerization to merocyanine upon exposure to GSH and reversibility when irradiated with visible light.*

As described in the article,[179] a set of UV-vis absorbance measurements were performed on the four SP's to examine the responsiveness to GSH, switching capability, selectively and response to biologically relevant metal ions. Before the absorbance measurements were conducted, all SP's were placed in the dark for 10 minutes prior to exposure to equimolar GSH. An initial absorbance scan was performed, and a subsequent scan was done after GSH introduction. The appearance of the merocyanine λ_{max} was monitored over a range of 300-600 nm. Figure 4.5 investigates the selectivity of SP-1, SP-3, SP-7, and SP-9 to GSH compared to equimolar concentrations of various amino acids and GSSG by examining the change in absorbance at the λ_{max} for the generation of MC. It was observed that SP-1 was more selective for GSSG than GSH and SP-3 exhibited a modest response to all samples except for arginine. Therefore, **SP-7** and **SP-9** were chosen for their selectivity and sensitivity (LOD = 2.4 μM & 2.2 μM, respectively) to construct an activatable MRI contrast agent that is responsive to GSH.

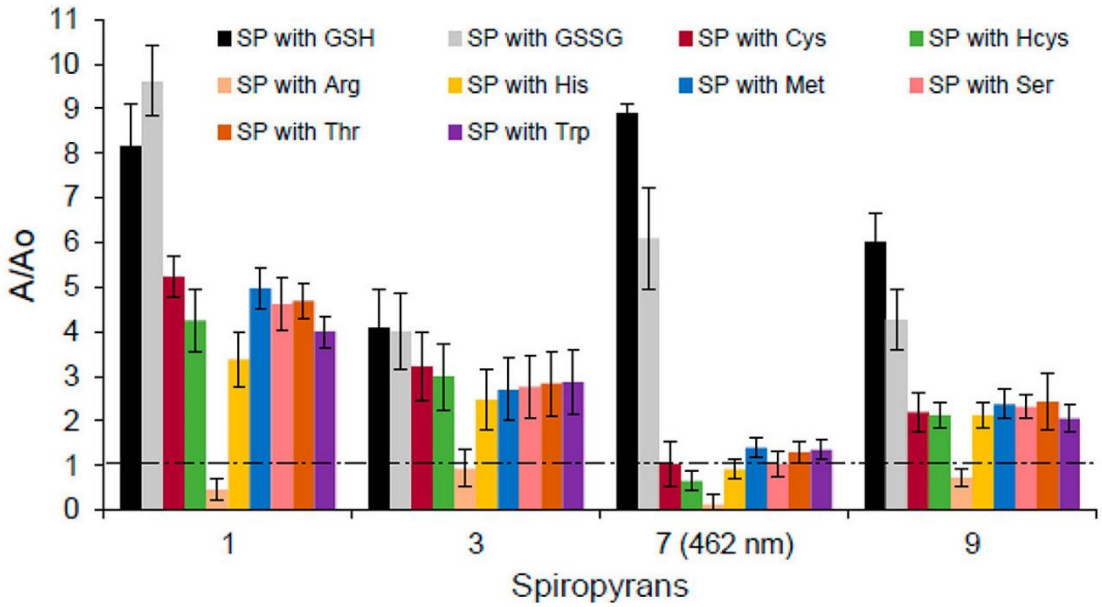

***Figure 4.5**. Spiropyran -1, -3, 7-, -9 (0.5 mM, EtOH/H_2O, pH = 7.4) selectivity to GSH (0.5 mM) over equimolar GSSG and various amino acids. Reprinted with permission from [*179*]. Copyright 2019 American Chemical Society (ACS)*

4.4 The development of a Manganese-based activatable MRI contrast agent responsive to glutathione.

4.4.1 Concept of a GSH sensitive MRI agent

Current, clinically used contrast agents employ gadolinium ion (Gd^{3+}) to provide contrast. The design of a macrocyclic or linear chelator increases the stability, preventing release of free Gd^{3+} in the body. Nevertheless, this process still occurs and can result in side effects such as nephrogenic systemic fibrosis[282–284] and a long-lasting accumulation in the brain.[285,286] Therefore, attention has shifted towards developing non-gadolinium-based contrast agents. This growing need to investigate a less-toxic agent has raised interest in divalent manganese as an alternative to gadolinium. In fact, the safety factor (LD50/effective dose) ,where the higher the number the safer

the product, for Mn-DPDP is 540, is much higher compared to the Gd-DTPA safety factor of 60–100.[287,288] Therefore, to create and activatable contrast agent, Mn^{2+} was chosen as the metal for its safety factor and **SP-7** and **SP-9** were chosen for their GSH responsiveness. A macrocyclic chelator i.e. 1,4-DO2A was chosen for its increased stability over linear chelators. The *cis*-1,4-DO2A di-acetate chelator was chosen over the *trans*-1,7-DO2A because it was found to contain a hydration state q = 0.87 and higher metal ligand stability (log K_{ML} = 16.13) vs *trans*-1,7-DO2A, q = 0 and log K_{ML} =14.54.[289]

Scheme 4.2 depicts the proposed GSH responsive MRI activatable agent where the "closed" SP is initially present in the dark and the 1,4-DO2A chelated Mn^{2+} contains a hydration state q = 0.87. In the presence of GSH, the SP isomerizes to the "open" zwitterionic MC form. This new arrangement produces a phenolic oxygen that could provide an electrostatic interaction or binding coordination between the manganese and the oxygen, thus decreasing the water hydration state of the manganese. This change in hydration state could provide a change in T_1-weighted MRI contrast from bright to dark. The utilization of MRI as a modality for molecular imaging of GSH is an appealing option because of its noninvasive nature and high spatial resolution. This will allow us to examine the fluctuations in GSH levels in real time without disturbing tissue physiology. This study will have a profound impact on our ability to determine tumor state.

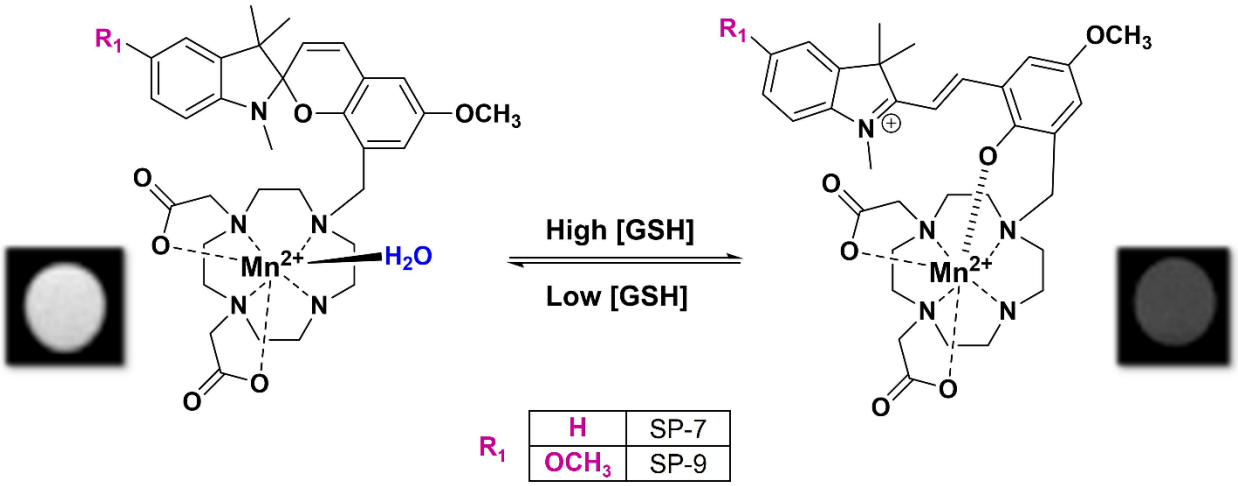

***Scheme 4.2**. Proposed concept in the construction of a manganese-based activatable T_1 contrast agent illustrating the isomerization of Mn(II) SP-1,4-DO2A to Mn(II) MC-1,4-DO2A in the presence of glutathione.*

4.4.2 SYNTHESIS OF THE ACTIVATABLE CONTRAST AGENT

Using a library of spiropyran photoswitches previously synthesized by others in the group,[153] I chose to synthesize **SP-7** and **SP-9** due to their responsiveness to GSH and conjugated them to a 1,4-DO2A chelator that was metalated with Mn^{2+} (Scheme 4.3). In brief, compound **1** was made via bis-hydroxyl methylation using formaldehyde under basic conditions and followed by selective mono-oxidation with manganese dioxide in acetone to afford compound **2**. Condensation with commercially available 1,3,3-trimethyl-2-methyleneindoline with **2** provided SP7-OH (**5a**). For SP9-OH, the indolium iodide was prepared from the methoxyhydrazine through an interrupted Fisher indole synthesis, followed by methylation with iodomethane to produce 5-methoxy-1,2,3,3-tetramethyl-3H-indol-1-ium (**3**). **3** was deprotonated to the methyleneindoline (**4**) and condensation with **2** afforded **5b**. Halogenation of the hydroxyl group with thionyl chloride produced SP7-Cl (**6a)** or SP9-Cl (**6b).** Conjugation of **6** to 1,4-DO2A di-tert-butyl ester (**7**)

afforded **8a** or **8b**. Deprotection with TFA and subsequent metalation with Mn-triflate offered the final products Mn(II)-SP7-1,4-DO2A (**9a**) or Mn(II)-SP9-1,4-DO2A (**9b**).

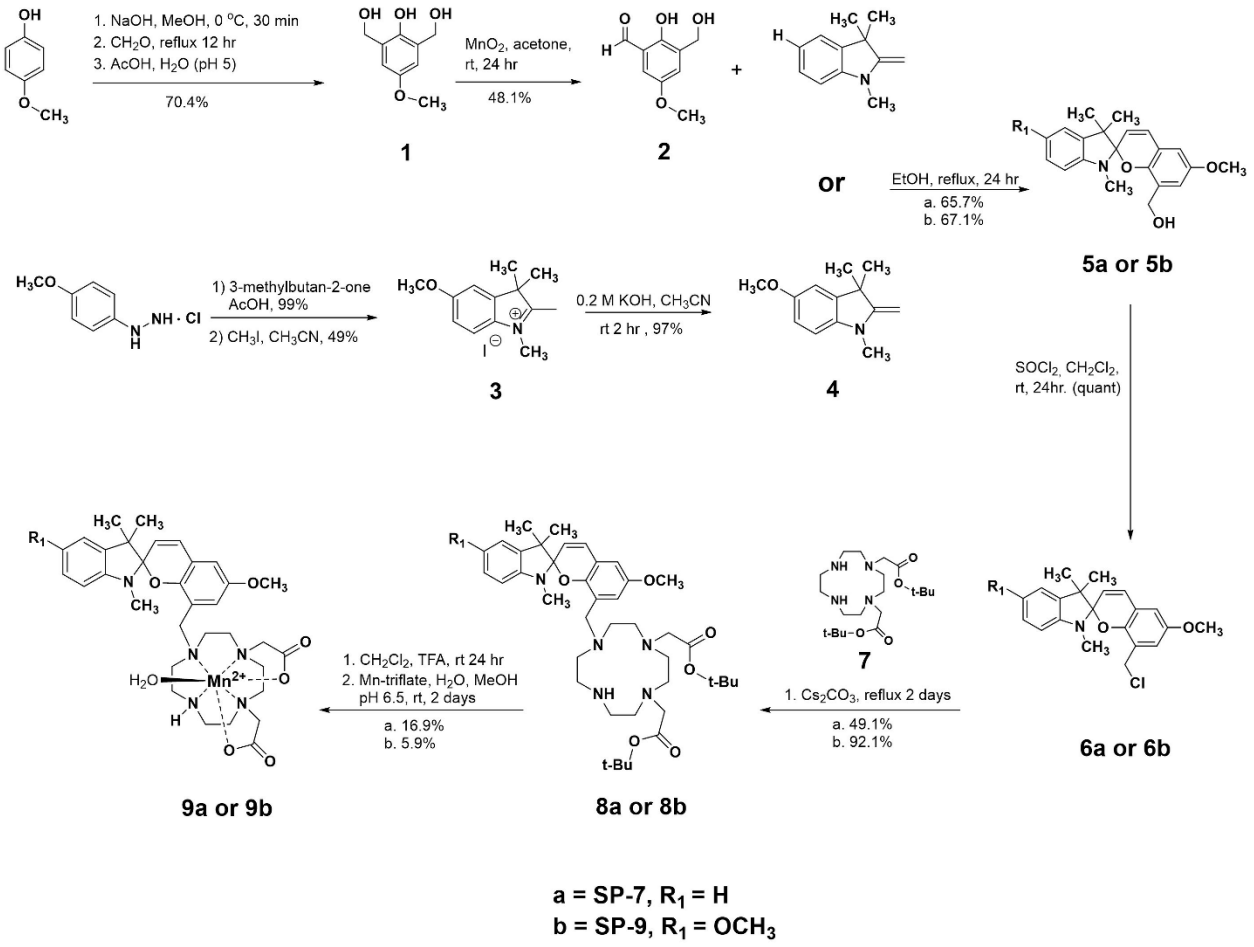

Scheme 4.3. *Synthesis of Mn(II)-**SP7**-1,4-DO2A and Mn(II)-**SP9**-1,4-DO2A.*

4.4.3 (R_1) RELAXIVITY

To test the responsiveness of the two activatable contrast agents, Mn-SP7-DO2A (**9a**) and Mn-SP9-DO2A (**9b**), to GSH, relaxivity studies were performed in the absence and presence of 5

mM GSH. Initially, the assay was performed in DI water (Milli-Q system, 18.2 MΩ-cm) with Mn-SP9-DO2A and the resulting relaxivity percent change was 408.9%, which was suspiciously large. However, after further inspection, it was found that glutathione is an acidic molecule due to the deprotonation of the carboxylic group on the glutamyl moiety (pK_a = 2.12) and the glycinyl carboxylic group (pK_a = 3.55) in water.[290] Therefore, it was hypothesized that the large percent change was a result of the expulsion of Mn^{2+} from the 1,4-DO2A chelator due to the acidic environment. Free Mn^{2+} would significantly decrease the T_1 time resulting in an increased relaxivity because of its high spin and fast water exchange rate. Thus, the responsiveness to GSH was repeated with the same experimental methods using PBS (pH = 7.4) as the solvent instead of Milli-Q water to ensure pH was stabilized (Figure 4.6). There was no change in relaxivity for Mn-SP7-1,4-DO2A (r_1 = 1.11 $mM^{-1}s^{-1}$) in the absence and presence of GSH (Figure 4.6A) Moreover, there was minimal change in relaxivity (1.87%) for Mn-SP9-1,4-DO2A in the absence (r_1 = 1.07 $mM^{-1}s^{-1}$) and presence (r_1 = 1.09 $mM^{-1}s^{-1}$) of GSH (Figure 4.6B).

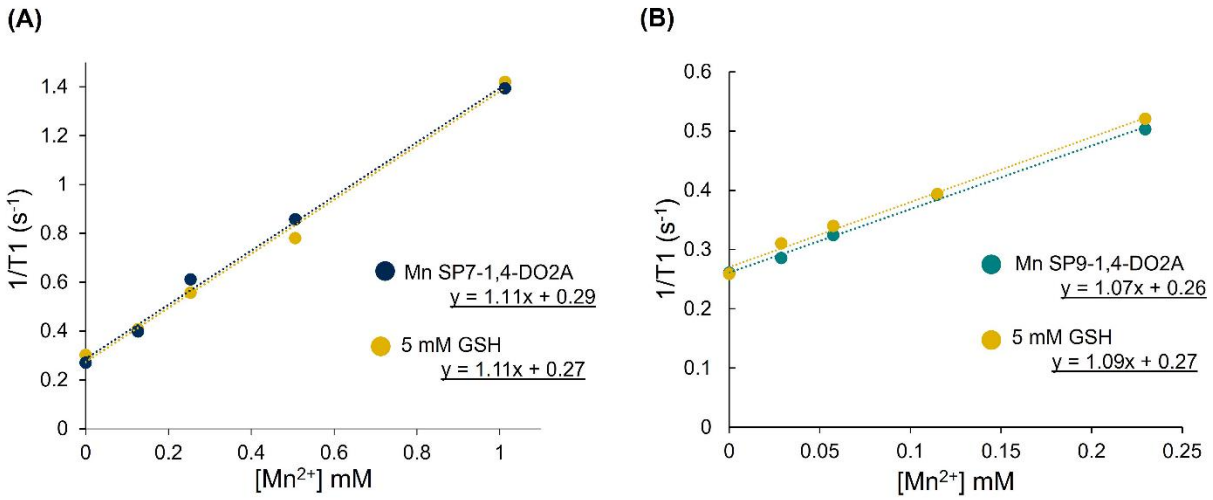

Figure 4.6. *r_1 relaxivity plot for (A) Mn-SP7-1,4-DO2A (navy blue) and (B) Mn-SP9-1,4-DO2A (teal) in the absence and presence (gold) of 5 mM GSH in PBS (pH = 7.4).*

Due to the unresponsiveness to GSH, and the fact that SPs are well-known for their photoactivity in which they isomerize to MC in the presence of UV light, both agents were irradiated with a 374 nm LED for 10 minutes (Figure 4.7). As shown in Figure 4.7A, Mn-**SP7**-1,4-DO2A had a r_1 relaxivity of 1.52 $mM^{-1}s^{-1}$ in the dark and with UV irradiation had a r_1 relaxivity of 1.35 $mM^{-1}s^{-1}$, producing 11.2% change. In Figure 4.7B, Mn-**SP9**-1,4-DO2A, displayed 16.0% change in relaxivity with a r_1 relaxivity of 2.68 $mM^{-1}s^{-1}$ in the dark and a r_1 relaxivity of 2.25 $mM^{-1}s^{-1}$ with UV light irradiation. For both agents, this change in relaxivity shows promise for the utilization as light activatable contrast agents.

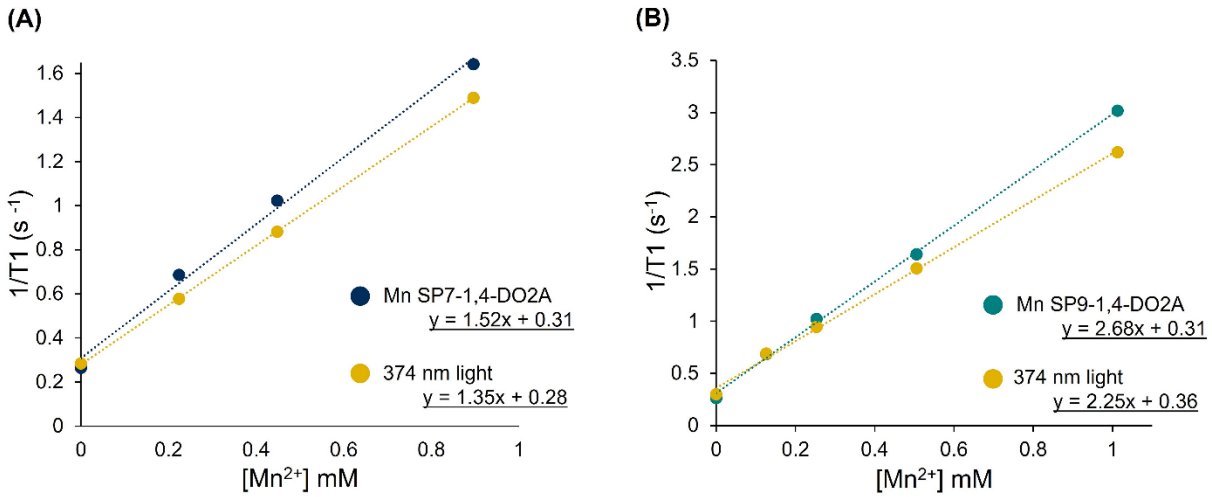

Figure 4.7. *r_1 relaxivity plot for (A) Mn-SP7-1,4-DO2A (navy blue) and (B) Mn-SP9-1,4-DO2A (teal) in the absence and presence (gold) of 374 nm LED irradiation for 10 min in water (pH = 6.1).*

4.5 MATERIALS AND METHODS

4.5.1 MATERIALS

Reagents were obtained from commercial suppliers and used directly, unless otherwise noted. Accurate mass measurements were recorded on positive electrospray ionization (ESI) mode in CH_3OH or CH_3CN on a Thermo Electron LTQ-Orbitrap Hybrid MS (Thermo Fisher Scientific Waltham, MA). ^1H and ^{13}C NMR spectra were measured in the solvent stated at 600 or 800 MHz, respectively (Bruker Avance III 600 or 800 MHz, Bruker LLC, Billerica, MA). Manganese content was determined by microwave plasma – atomic emission spectrometer (4210 MP-AES Agilent, Santa Clara, CA). T_1 relaxation time was measured on a 1.5 T Bruker Minispec relaxometer at 37°C. GSH samples were prepared in PBS (pH = 7.4) and UV-light samples were prepared in DI water (Milli-Q system, 18.2 MΩ-cm, pH = 6.1) from Barnstead Nanopure UV Systems (D502141, Thermo Scientific, Vernon Hills, IL).

4.5.2 SYNTHESIS AND STRUCTURAL CHARACTERIZATIONS

*(2-hydroxy-5-methoxy-1,3-phenylene)dimethanol (**1**).*

A degassed solution of aqueous 0.25 M NaOH (8.75 g, 0.21 mol, 35 mL) was added dropwise over a period of 15 min to a solution of 4-methoxyphenol (5 g, 0.04 mol, 12.5 mL) in methanol. This solution was stirred over ice for 30 min. Formaldehyde (60 mL) was added to the solution and refluxed at 60°C for 12 hr. The reaction was allowed to cool to room temperature and neutralized with glacial acetic acid to pH = 5. The product was extracted with ethyl acetate (100 mL) and H_2O (100 mL). The organic layer was collected, dried with Na_2SO_3, and concentrated. The crude residue was purified by silica gel column chromatography using 1:1 hexane: ethyl acetate (R_f = 0.25) to obtain **1** as a clear oil. (5.22 g, 70.4%) ^1H NMR (800 MH_z CD_3CN): δ 7.74

(s, 1H, OH), 6.70 (s, 2H, CH), 4.65 (d, J = 5.4 Hz, 4H, CH_2), 3.71 (s, 3H, OCH_3), 3.69 (s, 2H, OH). MS, ESI^-: m/z = 183.07 $[M - H]^-$.

*2-hydroxy-3-(hydroxymethyl)-5-methoxybenzaldehyde (**2**).*[291]

Following a modified literature procedure, a solution containing **1** (5 g, 0.27 mol) was dissolved in acetone (500 mL) and activated MnO_2 (11.80 g, 0.14 mol) was added. The reaction was stirred at room temperature for 24 h, followed by filtration of MnO_2 and concentrated. The crude residue was purified by silica gel column chromatography using 5:1 hexane: ethyl acetate (R_f = 0.34) to obtain **2** as a yellow solid (2.4 g, 48.1%) ^1H NMR (800 MHz $CDCl_3$): δ 10.98 (s, 1H, OH), 9.87 (s, 1H, COH), 7.23 (d, J = 3.1 Hz, 1H, CH), 6.96 (d, J = 3.1 Hz, 1H, CH), 4.75 (d, J = 6.2 Hz, 2H, CH_2), 3.83 (s, 3H, OCH_3), 2.31 (t, J = 6.4 Hz, 1H, OH). MS, ESI^-: m/z = 181.05 $[M – H]^-$.

*5-Methoxy-1,2,3,3-tetramethyl-3H-indol-1-ium iodide (**3**).*[160]

Following a modified literature procedure,[161] a solution containing 3-methylbutan-2-one (5.90 mL, 55.2 mmol) in glacial acetic acid (88 mL) was added 4-methoxyphenylhydrazine hydrochloride (4.815 g, 27.57 mmol). The solution was stirred at reflux for 5.5 h, allowed to cool to room temperature and neutralized with KOH pellets. The crude material was extracted with Et_2O (3 × 100 mL), dried over $MgSO_4$, filtered, and concentrated *in vacuo*. The crude product was purified by flash column chromatography (70:30, hexanes/EtOAc) to afford 2,3,3-trimethyl-5-methoxy-3H-indole as a red amorphous solid (5.149 g, 99%). ^1H NMR (600 MHz, $CDCl_3$) δ 7.43 (d, J = 8.3 Hz, 1H), 6.84-6.80 (m, 2H), 3.82 (s, 3H), 2.24 (s, 3H), 1.28 (s, 6H). ^1H NMR is consistent with published data.[162] Following a modified literature procedure,[161] iodomethane (0.048 mL, 0.76 mmol) was added to a solution of 2,3,3-trimethyl-5-methoxy-3H-indole (0.133 g,

0.716 mmol) in anhydrous acetonitrile (14.3 mL). The solution was stirred at reflux for 21 h. The solution was allowed to cool to room temperature, concentrated *in vacuo*, and suspended in $CHCl_3$ (2.5 mL) and hexanes (20 mL). The suspension was sonicated for 30 min and filtered to afford indolium **3** as a pink amorphous solid (0.117 g, 49%). ^{1}H NMR (600 MHz, $CDCl_3$) δ 7.56 (d, *J* = 8.7 Hz, 1H), 7.07-7.01 (m, 2H), 4.23 (s, 3H), 3.90 (s, 3H), 3.04 (s, 3H), 1.65 (s, 6H). ^{1}H NMR is consistent with published data.[160] MS, ESI$^+$: *m/z* = 204.14 $[M+H]^+$.

*5-methoxy-1,3,3-trimethyl-2-methyleneindoline (**4**).*[292]

Following a modified literature procedure, an aqueous solution of 0.3 M KOH (56 mL) was added dropwise to a solution of **3** (1 g, 3 mmol) in CH_3CN (20 mL) and stirred at room temperature for 2 hr. The mixture was washed with CH_2Cl_2 (3 x 30 mL), the organic phase was dried with $MgSO_4$, and concentrated in *in vacuo* to afford a violet solid (0.60 g, 97%). ^{1}H NMR (800 MHz, $CDCl_3$) δ 6.76 (d, *J* = 2.5 Hz, 1H, CH), 6.70 (dd, *J* = 8.4, 2.5 Hz, 1H, CH), 6.45 (d, *J* = 8.4 Hz, 1H, CH), 3.81 (d, *J* = 1.8 Hz, 2H, CH_2), 3.79 (s, 3H, OCH_3) 3.03 (s, 3H), 1.36 (s, 6H). MS, ESI$^+$: *m/z* = 204.33 $[M+H]^+$.

*(6-methoxy-1',3',3'-trimethylspiro[chromene-2,2'-indolin]-8-yl)methanol **SP7-OH** (**5a**).*

Commercially available 1,3,3-trimethyl-2-methyleneindoline (1 g, 5.77 mmol) was dissolved in ethanol (50 mL). To the reaction flask, **2** (0.72 g, 4 mmol) dissolved in ethanol (50 mL) was added and the solution was stirred at reflux for 24 h. The crude residue was purified by silica gel column chromatography using 1:1 hexane: ethyl acetate (R_f = 0.57) to obtain **5a** as a purple solid (0.88 g, 65.7%). ^{1}H NMR (600 MHz, $CDCl_3$) δ 7.13 (td, *J* = 7.6, 1.2 Hz, 1H), 7.05 (dd, 1H), 6.84 – 6.79 (m, 2H), 6.68 (d, *J* = 2.9 Hz, 1H), 6.56 (d, *J* = 3.0 Hz, 1H), 6.48 (d, *J* = 7.7

Hz, 1H), 5.74 (d, *J* = 10.2 Hz, 1H), 4.50 – 4.29 (m, 2H), 3.74 (s, 3H), 2.66 (s, 3H), 1.95 (t, *J* = 6.5 Hz, 1H), 1.29 (s, 3H), 1.17 (s, 3H). MS, ESI^+: *m/z* = 338.17 $[M+H]^+$.

(5',6-dimethoxy-1',3',3'-trimethylspiro[chromene-2,2'-indolin]-8-yl)methanol ***SP9-OH (5b).***

The methyleneindoline, **4** (0.72 g, 3.5 mmol) was dissolved in ethanol (35 mL). To the reaction flask, **2** (0.54 g, 3 mmol) dissolved in ethanol (35 mL) was added and the solution was stirred at reflux for 24 h. The crude residue was purified by silica gel column chromatography using 3:1 hexane: ethyl acetate (R_f = 0.33) to obtain **5b** as a purple solid (0.73 g, 67.1%). ^1H NMR (600 MHz, $CDCl_3$) δ 6.81 (d, *J* = 10.3 Hz, 1H), 6.69 (d, *J* = 2.5 Hz, 1H), 6.68 – 6.63 (m, 2H), 6.55 (d, *J* = 3.1 Hz, 1H), 6.38 (d, *J* = 8.4 Hz, 1H), 5.73 (d, *J* = 10.1 Hz, 1H), 4.54 – 4.25 (m, 2H), 3.77 (s, 3H), 3.74 (s, 3H), 2.61 (s, 3H), 2.01 (s, 1H), 1.27 (s, 3H), 1.18 (s, 3H). MS, ESI^+: *m/z* = 368.18 $[M+H]^+$.

8-(chloromethyl)-6-methoxy-1',3',3'-trimethylspiro[chromene-2,2'-indoline] ***SP7-Cl (6a).***

A solution containing **5a** (0.88 g, 2.6 mmol) was dissolved in dichloromethane (10 mL) and thionyl chloride (0.38 mL, 5.23 mmol) was added. The reaction was stirred at room temperature for 2 h, followed by washing with dichloromethane (3x 50 mL) and concentrated *in vacuo* producing a red solid. ^1H NMR (600 MH_z, CD_3CN): δ 1.85 (s, 6H, CH_3), 3.46 (s, 3H, N-CH_3), 3.87 (s, 3H, OCH_3), 4.65 (s, 2H, CH_2), 7.12 (d, 1H, CH), 7.42 (d, 1H, CH), 7.51 (s, 1H, CH), 7.54 (s, 1H, CH), 7.63-7.74 (m, 4H, CH). ^{13}C NMR (600 MH, CD_3CN): δ 25.52, 52.51, 55.71, 57.96, 60.92, 70.95, 110.37, 111.99, 114.71, 121.80, 122.75, 123.45, 128.91, 129.21, 129.50, 141.96, 143.43, 148.98, 151.67, 153.40. MS, ESI^+: *m/z* = 356.10 $[M + H]^+$.

8-(chloromethyl)-5',6-dimethoxy-1',3',3'-trimethylspiro[chromene-2,2'-indoline] ***SP9-Cl (6b)****.*

A solution containing **5b** (0.73 g, 2.0 mmol) was dissolved in dichloromethane (10 mL) and thionyl chloride (0.3 mL, 4.0 mmol) was added. The reaction was stirred at room temperature for 2 h, followed by washing with dichloromethane (3x 50 mL) and concentrated *in vacuo* producing a red solid. ^{1}H NMR (600 MH_z, CD_3CN): δ 1.81 (s, 6H, CH_3), 3.49 (s, 3H, N-CH_3), 3.87, (s, 3H, OCH_3), 3.94 (s, 3H, OCH_3), 4.68 (s, 2H, CH_2), 7.06 (s, 1H, CH), 7.17 (d, 1H, CH), 7.24 (d, 1H, CH), 7.31 (s, 1H, CH), 7.38 (s, 1H CH), 7.42 (d, 1, CH), 7.63 (d, 1H, CH). ^{13}C NMR (600 MH_z, CD_3CN): δ 25.72, 52.40, 55.75, 55.86, 56.10, 58.12, 71.90, 108.55, 111.01, 112.52, 114.96, 115.99, 121.19, 122.93, 125.14, 127.28, 145.67, 147.49, 151.43, 153.27, 161.47. MS, ESI^+: *m/z* = 386.13 $[M + H]^+$.

di-tert-butyl 2,2'-(1,4,7,10-tetraazacyclododecane-1,4-diyl)diacetate (**7**).[293]

Following a modified literature procedure[293], a solution containing 1,4,7,10-tetraazacyclododecane (cyclen) (0.10 g, 0.58 mmol) in anhydrous chloroform (5 mL) was added triethylamine (0.80 mL, 5.8 mmol). Tert-butyl bromo acetate (0.23 g, 1.2 mmol) dissolved in anhydrous chloroform (6.50 mL) was added to the reaction flask dropwise. The solution was stirred at room temperature for 6 h and concentrated *in vacuo*. The crude was resuspended in H_2O (2.5 mL) and the pH was adjusted to 11-12 by addition of NaOH (40% w/v) followed by extraction with chloroform (4 x 5 mL). The organic layers were collected, dried with $NaSO_4$, and dried *in vacuo*. The crude product was purified by neutral alumina gel column chromatography using 20:1 dichloromethane: methanol to obtain **7**, a white solid. (0.14 g, 60.7%). ^{1}H NMR (600 MHz, $CDCl_3$) δ 3.31 (s, 4H), 2.95 (d, *J* = 7.3 Hz, 8H), 2.86 (d, *J* = 5.6 Hz, 8H), 1.40 (s, 18H). MS, ESI^+: *m/z* = 401.32 $[M + H]^+$.

*tert-butyl 2-(4-((5',6-dimethoxy-1',3',3'-trimethylspiro[chromene-2,2'-indolin]-8-yl)methyl)-10-(3,3-dimethyl-2-oxobutyl)-1,4,7,10-tetraazacyclododecan-1-yl)acetate (**8a**).*

A solution of **5a** (0.08 g, 0.22 mmol) in anhydrous acetonitrile (20 mL) was added dropwise over a period of 15 min to a solution of **7** (0.075 g, 0.19 mmol) and Cs_2CO_3 (0.183 g, 0.56 mmol) in anhydrous acetonitrile. This reaction mixture was refluxed for 2 days in inert atmosphere using argon balloon and was purified by neutral alumina gel column chromatography using 35:1 dichloromethane: methanol to obtain **8a**, a purple solid. (0.088 g, 49.1%). ^{1}H NMR (600 MHz, $CDCl_3$) δ 7.07 – 6.89 (m, 4H), 6.89 – 6.79 (m, 2H), 6.68 (q, *J* = 7.5 Hz, 1H), 6.40 (d, *J* = 7.7 Hz, 1H), 6.33 (d, *J* = 7.3 Hz, 1H), 5.72 (dd, *J* = 10.2, 3.1 Hz, 1H), 3.77 (s, 4H), 3.77 – 3.70 (m, 3H), 3.18 – 3.00 (m, 4H), 2.86 (d, *J* = 17.2 Hz, 2H), 2.66 (s, 4H), 2.64 (s, 3H), 2.60 – 2.50 (m, 4H), 1.41 (s, 18H), 1.16 (d, *J* = 49.1 Hz, 6H). MS, ESI$^+$: *m/z* = 720.47 $[M + H]^+$, 360.74 $[M + H]^{2+}$.

*tert-butyl 2-(4-(3,3-dimethyl-2-oxobutyl)-10-((6-methoxy-1',3',3'-trimethylspiro[chromene-2,2'-indolin]-8-yl)methyl)-1,4,7,10-tetraazacyclododecan-1-yl)acetate (**8b**).*

A solution of **5b** (0.08 g, 0.19 mmol) in anhydrous dichloromethane (20 mL) was added dropwise over a period of 15 min to a solution of **7** (0.075 g, 0.19 mmol) and Cs_2CO_3 (0.183 g, 0.56 mmol) in anhydrous dichloromethane. This reaction mixture was refluxed for 2 days in inert atmosphere using argon balloon and was purified by neutral alumina gel column chromatography using 35:1 dichloromethane: methanol to obtain **8b**, a purple solid. (0.13 g, 92.1 %). ^{1}H NMR (600 MHz, $CDCl_3$) δ 6.92 (d, *J* = 3.1 Hz, 1H), 6.79 (dd, *J* = 10.3, 1.3 Hz, 1H), 6.69 – 6.60 (m, 4H), 6.58 – 6.53 (m, 1H), 6.36 (dd, *J* = 8.3, 1.3 Hz, 1H), 5.71 (dd, *J* = 10.2, 1.2 Hz, 1H), 3.76 (d, *J* = 1.3 Hz, 3H), 3.73 (d, *J* = 1.3 Hz, 3H), 3.58 (d, *J* = 13.3 Hz, 1H), 3.33 (d, *J* = 13.3 Hz, 3H), 3.18 (dd, *J* = 12.9, 1.3 Hz, 1H), 3.07 (s, 2H), 2.85 (d, *J* = 12.2 Hz, 4H), 2.58 (s, 3H), 2.22 (s, 1H), 1.44 (d, *J* =

1.3 Hz, 9H), 1.43 – 1.40 (m, 1H), 1.37 – 1.35 (m, 9H), 1.35 (s, 2H), 1.23 (d, *J* = 4.6 Hz, 4H), 1.21 (s, 3H), 1.15 (s, 3H). MS, ESI^+: *m/z* = 750.48 $[M + H]^+$, 375.74 $[M + H]^{2+}$.

*Mn(II)-**SP7**-1,4-DO2A (**9a**).*

A solution containing **8a** (0.09 g, 0.12 mmol) was dissolved in dichloromethane (1 mL) and trifluoroacetic acid (0.56 mL, 7.4 mmol) was added. The reaction was stirred at room temperature for 24 h, followed by filtering with dichloromethane (3x 10 mL) and concentrated *in vacuo* producing a red-yellow solid. MS, ESI^+: *m/z* = 608.35 $[M + H]^+$, 304.68 $[M + H]^{2+}$. From this stock, the deprotected material (0.07 g, 0.12 mmol) was dissolved in methanol (3 mL) and the pH was adjusted to 6.5 by addition of NH_4OH (10% v/v in methanol). The solvent was removed and the solid was resuspended in H_2O (1.1 mL). Mn^{2+}-triflate (0.09 g, 0.24 mmol) dissolved in H_2O (1.1 mL) was added dropwise over a period of 10 min and the reaction was stirred at room temperature for 48 hr. Chelex 100 (4.2 g, 0.40 meq) was used to remove excess unmetallated Mn^{2+} and was concentrated *in vacuo* to afford **9a** a purple solid. MS, ESI^+: *m/z* = 661.27 $[M + H]^+$, 331.14 $[M + H]^{2+}$. MP-AES of a 5 mg stock solution of **9a** (0.07 mg, 16.9%)

*Mn(II)-**SP9**-1,4-DO2A (**9b**).*

A solution containing **8b** (0.13 g, 0.17 mmol) was dissolved in dichloromethane (1.2 mL) and trifluoroacetic acid (0.397 mL, 5.2 mmol) was added. The reaction was stirred at room temperature for 24 h, followed by filtering with dichloromethane (3x 10 mL) and concentrated *in vacuo* producing a red-yellow solid. MS, ESI^+: *m/z* = 638.36 $[M + H]^+$, 319.68 $[M + H]^{2+}$. From this stock, the deprotected material (0.11 g, 0.17 mmol) was dissolved in methanol (1.75 mL) and the pH was adjusted to 6.5 by addition of NH_4OH (10% v/v in methanol). The solvent was removed and the solid was resuspended in H_2O (1 mL). Mn^{2+}-triflate (0.18 g, 0.52 mmol) dissolved in H_2O

(1 mL) was added dropwise over a period of 10 min and the reaction was stirred at room temperature for 48 hr. Chelex 100 (10 g, 0.40 meq) was used to remove excess unmetallated Mn^{2+} and was concentrated *in vacuo* to afford **9b** a purple solid. MS, ESI^+: *m/z* = 691.28 $[M + H]^+$, 346.14 $[M + H]^{2+}$. MP-AES of a 5 mg stock solution of **9b** (0.08 mg, 5.9%)

4.5.3 RELAXIVITY MEASUREMENTS

Longitudinal (r_1) relaxivity

A series of aqueous solutions (200 μL each) were prepared and the concentrations of compound **9a** or **9b** ranged from 0 to 1.0 mM or 0 to 0.23 mM, respectively. The solutions were stored in the dark. T_1 relaxation times of these solutions were measured before and after addition of 5 mM concentration of GSH in PBS (pH = 7.4). The longitudinal (r1) relaxivity was determined as the slope of the line for plots of $1/T_1$, against increasing manganese concentration. The same method was used for measuring the effect of UV light on the r1 relaxivity of compound **9a** or **9b** in DI water (Milli-Q system, 18.2 MΩ-cm, pH = 6.1). A series of aqueous solutions (200 μL each) were prepared and the concentrations of compound **9a** or **9b** ranged from 0 to 0.90 mM or 0 to 0.10 mM, respectively. The solution was incubated for 10 min at 37°C and simultaneously irradiated with a 374 nm LED before the T_1 relaxation time measurement was taken. T_1 relaxation time was measured on a 1.5 T Bruker Minispec relaxometer at 37°C.

4.6 CONCLUSIONS AND FUTURE DIRECTIONS

Two spiropyran-based molecular sensors, **SP-7** and **SP-9**, were previously found to be responsive to GSH. In the presence of GSH, "closed" SP isomerized to its "open" MC form allowing for differentiation between the two isomers. In this work, **SP-7** or **SP-9** was conjugated to a 1,4-DO2A chelator and metallated with manganese(II) to construct a Mn-based activatable contrast agent for MRI. It was hypothesized that SP responsiveness to GSH would allow for structural rearrangement and conversion to the MC isomer, producing the phenolic oxygen that would bind to manganese and decrease the hydration state from 1 to 0 thus changing the relaxivity which would change the contrast in the MR image. A multi-step synthesis was performed to produce the final products Mn(II)-**SP7**-1,4-DO2A and Mn(II)-**SP9**-1,4-DO2A, as the activatable agents. Unfortunately, when relaxivity studies were conducted in the presence of 5 mM GSH these two agents did not show any significant change in relaxivity (no change and 1.87%, respectively). Since SPs are known to respond to UV light in the conversion to MC, a 374 nm LED was used to investigate their potential application as a light activatable agents. Mn(II)-**SP7**-1,4-DO2A exhibited 11.2% change and Mn(II)-**SP9**-1,4-DO2A produced 16.0% change in the presence of UV light. Further studies could be directed toward maximizing the conversion from SP to the MC isomer to get the optimal change in relaxivity. This can be done by determining the appropriate amount of time for irradiation before thermal degradation. Once this time is established, inspection of the relaxation rate can be conducted to see if there is a difference between the 10 min irradiation and the new optimized time.

REFERENCES

(1) Decker, H.; Felser, H. Über Cyclische Oxoniumsalze Aus Dicumarketon Und Über Spiropyranderivate. *Berichte der deutschen chemischen Gesellschaft* **1908**, *41* (2), 2997–3007. https://doi.org/10.1002/cber.190804102251.

(2) Fischer, E.; Hirshberg, Y. Formation of Coloured Forms of Spirans by Low-Temperature Irradiation. *J. Chem. Soc.* **1952**, No. Nov, 4522–4524.

(3) Wojtyk, J. T. C.; Wasey, A.; Xiao, N.-N.; Kazmaier, P. M.; Hoz, S.; Yu, C.; Lemieux, R. P.; Buncel, E. Elucidating the Mechanisms of Acidochromic Spiropyran-Merocyanine Interconversion. *J. Phys. Chem. A* **2007**, *111* (13), 2511–2516. https://doi.org/10.1021/jp068575r.

(4) Kalisky, Y.; Orlowski, T. E.; Williams, D. J. Dynamics of the Spiropyran-Merocyanine Conversion in Solution. *J. Phys. Chem.* **1983**, *87* (26), 5333–5338. https://doi.org/10.1021/j150644a006.

(5) Chibisov, A. K.; Görner, H. Photoprocesses in Spiropyran-Derived Merocyanines. *J. Phys. Chem. A* **1997**, *101* (24), 4305–4312. https://doi.org/10.1021/jp962569l.

(6) Reeves, D. A.; Wilkinson, F. Photochromism of Spiropyrans. Part 1. Mechanism of Photocolouration. *J. Chem. Soc., Faraday Trans. 2* **1973**, *69* (0), 1381–1390. https://doi.org/10.1039/F29736901381.

(7) Tyer, N. W.; Becker, R. S. Photochromic Spiropyrans. Absorption Spectra and Evaluation of the Electron Orthogonality of the Constituent Halves. *J. Am. Chem. Soc.* **1970**, *92* (5), 1289–1294. https://doi.org/10.1021/ja00708a031.

(8) Favaro, G.; Masetti, F.; Mazzucato, U.; Ottavi, G.; Allegrini, P.; Malatesta, V. Photochromism, Thermochromism and Solvatochromism of Some Spiro[Indolinoxazine]-Photomerocyanine Systems: Effects of Structure and Solvent. *J. Chem. Soc., Faraday Trans.* **1994**, *90* (2), 333–338. https://doi.org/10.1039/FT9949000333.

(9) Moniruzzaman, M.; Sabey, C. J.; Fernando, G. F. Photoresponsive Polymers: An Investigation of Their Photoinduced Temperature Changes during Photoviscosity Measurements. *Polymer* **2007**, *48* (1), 255–263. https://doi.org/10.1016/j.polymer.2006.08.066.

(10) Zhang, Y.; Ng, M.; Hong, E. Y.-H.; Chan, A. K.-W.; Wu, N. M.-W.; Chan, M. H.-Y.; Wu, L.; Yam, V. W.-W. Synthesis and Photoswitchable Amphiphilicity and Self-Assembly Properties of Photochromic Spiropyran Derivatives. *J. Mater. Chem. C* **2020**, *8* (39), 13676–13685. https://doi.org/10.1039/D0TC03301D.

(11) Heiligman-Rim, R.; Hirshberg, Y.; Fischer, E. Photochromism in Spiropyrans. Part V. on the Mechanism of Phototransformation. *J. Phys. Chem.* **1962**, *66* (12), 2470–2477. https://doi.org/10.1021/j100818a036.

(12) Kovalenko, O.; Reguero, M. Why Thermal Isomerization of the Chromic Switch Spiropyran-Merocyanine Is Enhance in Polar Protic Solvents. A Computational Study of the Reaction Mechanism. *Phys. Scr.* **2020**, *95* (5), 055402. https://doi.org/10.1088/1402-4896/ab5ff2.

(13) Mandal, M.; Banik, D.; Karak, A.; Manna, S. K.; Mahapatra, A. K. Spiropyran–Merocyanine Based Photochromic Fluorescent Probes: Design, Synthesis, and Applications. *ACS Omega* **2022**, *7* (42), 36988–37007. https://doi.org/10.1021/acsomega.2c04969.

(14) Berkovic, G.; Krongauz, V.; Weiss, V. Spiropyrans and Spirooxazines for Memories and Switches. *Chem. Rev.* **2000**, *100* (5), 1741–1754. https://doi.org/10.1021/cr9800715.
(15) Keyvan Rad, J.; Balzade, Z.; Mahdavian, A. R. Spiropyran-Based Advanced Photoswitchable Materials: A Fascinating Pathway to the Future Stimuli-Responsive Devices. *J. Photochem. Photobiol* **2022**, *51*, 100487. https://doi.org/10.1016/j.jphotochemrev.2022.100487.
(16) Breslin, V. M.; Garcia-Garibay, M. A. Transmission Spectroscopy and Kinetics in Crystalline Solids Using Aqueous Nanocrystalline Suspensions: The Spiropyran-Merocyanine Photochromic System. *Cryst. Growth Des.* **2017**, *17* (2), 637–642. https://doi.org/10.1021/acs.cgd.6b01476.
(17) Katsonis, N.; Lubomska, M.; Pollard, M. M.; Feringa, B. L.; Rudolf, P. Synthetic Light-Activated Molecular Switches and Motors on Surfaces. *Prog. Surf. Sci.* **2007**, *82* (7), 407–434. https://doi.org/10.1016/j.progsurf.2007.03.011.
(18) Dattler, D.; Fuks, G.; Heiser, J.; Moulin, E.; Perrot, A.; Yao, X.; Giuseppone, N. Design of Collective Motions from Synthetic Molecular Switches, Rotors, and Motors. *Chem. Rev.* **2020**, *120* (1), 310–433. https://doi.org/10.1021/acs.chemrev.9b00288.
(19) Li, M.; Zhang, Q.; Zhou, Y.-N.; Zhu, S. Let Spiropyran Help Polymers Feel Force! *Prog. Polym. Sci.* **2018**, *79*, 26–39. https://doi.org/10.1016/j.progpolymsci.2017.11.001.
(20) Stoychev, G.; Kirillova, A.; Ionov, L. Light-Responsive Shape-Changing Polymers. *Adv. Opt. Mater.* **2019**, *7* (16), 1900067. https://doi.org/10.1002/adom.201900067.
(21) Erbas-Cakmak, S.; Kolemen, S.; C. Sedgwick, A.; Gunnlaugsson, T.; D. James, T.; Yoon, J.; U. Akkaya, E. Molecular Logic Gates: The Past, Present and Future. *Chem Soc Rev* **2018**, *47* (7), 2228–2248. https://doi.org/10.1039/C7CS00491E.
(22) Meuter, N.; Spinnen, S.; Tausch, M. W. Light Makes Smart - Photoactive Molecular Switches for Logic Gates. *World J. Chem. Educ.* **2021**, *9* (4), 96–103. https://doi.org/10.12691/wjce-9-4-1.
(23) Ali, A. A.; Kharbash, R.; Kim, Y. Chemo- and Biosensing Applications of Spiropyran and Its Derivatives - A Review. *Anal. Chim. Acta* **2020**, *1110*, 199–223. https://doi.org/10.1016/j.aca.2020.01.057.
(24) Kumar, A.; Kumar, S. Light-Controlled Receptors for Environmentally and Biologically Relevant Anions. *J. Chem. Eng.* **2023**, *474*, 145493. https://doi.org/10.1016/j.cej.2023.145493.
(25) Kozlenko, A. S.; Ozhogin, I. V.; Pugachev, A. D.; Lukyanova, M. B.; El-Sewify, I. M.; Lukyanov, B. S. A Modern Look at Spiropyrans: From Single Molecules to Smart Materials. *Top Curr Chem* **2023**, *381* (1), 8. https://doi.org/10.1007/s41061-022-00417-2.
(26) Shymborska, Y.; Budkowski, A.; Raczkowska, J.; Donchak, V.; Melnyk, Y.; Vasiichuk, V.; Stetsyshyn, Y. Switching It Up: The Promise of Stimuli-Responsive Polymer Systems in Biomedical Science. *Chem. Rec. n/a* (n/a), e202300217. https://doi.org/10.1002/tcr.202300217.
(27) Zhu, H.; Fan, J.; Wang, B.; Peng, X. Fluorescent, MRI, and Colorimetric Chemical Sensors for the First-Row d-Block Metal Ions. *Chem. Soc. Rev.* **2015**, *44* (13), 4337–4366. https://doi.org/10.1039/C4CS00285G.
(28) Carter, K. P.; Young, A. M.; Palmer, A. E. Fluorescent Sensors for Measuring Metal Ions in Living Systems. *Chem. Rev.* **2014**, *114* (8), 4564–4601. https://doi.org/10.1021/cr400546e.

(29) Thompson, K. H.; Orvig, C. Boon and Bane of Metal Ions in Medicine. *Science* **2003**, *300* (5621), 936–939. https://doi.org/10.1126/science.1083004.
(30) Verwilst, P.; Sunwoo, K.; Kim, J. S. The Role of Copper Ions in Pathophysiology and Fluorescent Sensors for the Detection Thereof. *Chem. Commun.* **2015**, *51* (26), 5556–5571. https://doi.org/10.1039/C4CC10366A.
(31) Tapiero, H.; Townsend, D. M.; Tew, K. D. Trace Elements in Human Physiology and Pathology. Copper. *Biomed. Pharmacother.* **2003**, *57* (9), 386–398. https://doi.org/10.1016/S0753-3322(03)00012-X.
(32) The Metabolic Basis of Inherited Disease. 6th Edition. *Jap J Human Genet* **1989**, *34* (3), 253–253. https://doi.org/10.1007/BF01900731.
(33) Harris, E. D. Copper Transport: An Overview. *Proc. Soc. Exp. Biol. Med.* **1991**, *196* (2), 130–140. https://doi.org/10.3181/00379727-196-43171B.
(34) Tiffany-Castiglioni, E.; Qian, Y. Astroglia as Metal Depots: Molecular Mechanisms for Metal Accumulation, Storage and Release. *NeuroToxicology* **2001**, *22* (5), 577–592. https://doi.org/10.1016/S0161-813X(01)00050-X.
(35) Brewer, G. J. Copper Excess, Zinc Deficiency, and Cognition Loss in Alzheimer's Disease. *BioFactors* **2012**, *38* (2), 107–113. https://doi.org/10.1002/biof.1005.
(36) Brewer, G. J. Copper-2 Ingestion, Plus Increased Meat Eating Leading to Increased Copper Absorption, Are Major Factors Behind the Current Epidemic of Alzheimer's Disease. *Nutrients* **2015**, *7* (12), 10053–10064. https://doi.org/10.3390/nu7125513.
(37) Barnham, K. J.; Bush, A. I. Biological Metals and Metal-Targeting Compounds in Major Neurodegenerative Diseases. *Chem. Soc. Rev.* **2014**, *43* (19), 6727–6749. https://doi.org/10.1039/C4CS00138A.
(38) Gaggelli, E.; Kozlowski, H.; Valensin, D.; Valensin, G. Copper Homeostasis and Neurodegenerative Disorders (Alzheimer's, Prion, and Parkinson's Diseases and Amyotrophic Lateral Sclerosis). *Chem. Rev.* **2006**, *106* (6), 1995–2044. https://doi.org/10.1021/cr040410w.
(39) Pall, H. S.; Blake, D. R.; Gutteridge, J. M.; Williams, A. C.; Lunec, J.; Hall, M.; Taylor, A. Raised Cerebrospinal-Fluid Copper Concentration in Parkinson's Disease. *The Lancet* **1987**, *330* (8553), 238–241. https://doi.org/10.1016/S0140-6736(87)90827-0.
(40) Bull, P. C.; Thomas, G. R.; Rommens, J. M.; Forbes, J. R.; Cox, D. W. The Wilson Disease Gene Is a Putative Copper Transporting P–Type ATPase Similar to the Menkes Gene. *Nat Genet* **1993**, *5* (4), 327–337. https://doi.org/10.1038/ng1293-327.
(41) Ahuja, A.; Dev, K.; Tanwar, R. S.; Selwal, K. K.; Tyagi, P. K. Copper Mediated Neurological Disorder: Visions into Amyotrophic Lateral Sclerosis, Alzheimer and Menkes Disease. *J. Trace Elem. Med. Biol.* **2015**, *29*, 11–23. https://doi.org/10.1016/j.jtemb.2014.05.003.
(42) Valentine, J. S.; Doucette, P. A.; Zittin Potter, S. Copper-Zinc Superoxide Dismutase and Amyotrophic Lateral Sclerosis. *Annu. Rev. Biochem.* **2005**, *74* (1), 563–593. https://doi.org/10.1146/annurev.biochem.72.121801.161647.
(43) Bourassa, M. W.; Brown, H. H.; Borchelt, D. R.; Vogt, S.; Miller, L. M. Metal-Deficient Aggregates and Diminished Copper Found in Cells Expressing SOD1 Mutations That Cause ALS. *Front Aging Neurosci* **2014**, *6*, 110. https://doi.org/10.3389/fnagi.2014.00110.
(44) Elkhatat, A. M.; Soliman, M.; Ismail, R.; Ahmed, S.; Abounahia, N.; Mubashir, S.; Fouladi, S.; Khraisheh, M. Recent Trends of Copper Detection in Water Samples. *Bull. Natl. Res. Cent.* **2021**, *45* (1), 218. https://doi.org/10.1186/s42269-021-00677-w.

(45) Guidelines for Drinking-Water Quality: Fourth Edition Incorporating the First Addendum. Geneva: World Health Organization; 2017. License: CC BY-NC-SA 3.0 IGO.
(46) United States Environmental Protection Agency. Office of the Federal Register. National Archives and Records Administration. National Primary Drinking Water Regulations. Govinfo. (July 1, 2020). Https://Www.Govinfo.Gov/App/Details/CFR-2020-Title40-Vol25/CFR-2020-Title40-Vol25-Part141.
(47) Becker, J. S.; Zoriy, M. V.; Pickhardt, C.; Palomero-Gallagher, N.; Zilles, K. Imaging of Copper, Zinc, and Other Elements in Thin Section of Human Brain Samples (Hippocampus) by Laser Ablation Inductively Coupled Plasma Mass Spectrometry. *Anal. Chem.* **2005**, *77* (10), 3208–3216. https://doi.org/10.1021/ac040184q.
(48) Stadler, N.; Lindner, R. A.; Davies, M. J. Direct Detection and Quantification of Transition Metal Ions in Human Atherosclerotic Plaques: Evidence for the Presence of Elevated Levels of Iron and Copper. *Arterioscler Thromb Vasc Biol* **2004**, *24* (5), 949–954. https://doi.org/10.1161/01.ATV.0000124892.90999.cb.
(49) Kazi, T. G.; Afridi, H. I.; Kazi, N.; Jamali, M. K.; Arain, M. B.; Jalbani, N.; Kandhro, G. A. Copper, Chromium, Manganese, Iron, Nickel, and Zinc Levels in Biological Samples of Diabetes Mellitus Patients. *Biol Trace Elem Res* **2008**, *122* (1), 1–18. https://doi.org/10.1007/s12011-007-8062-y.
(50) Ghaedi, M.; Ahmadi, F.; Shokrollahi, A. Simultaneous Preconcentration and Determination of Copper, Nickel, Cobalt and Lead Ions Content by Flame Atomic Absorption Spectrometry. *J. Hazard. Mater.* **2007**, *142* (1), 272–278. https://doi.org/10.1016/j.jhazmat.2006.08.012.
(51) Shokrollahi, A.; Ghaedi, M.; Hossaini, O.; Khanjari, N.; Soylak, M. Cloud Point Extraction and Flame Atomic Absorption Spectrometry Combination for Copper(II) Ion in Environmental and Biological Samples. *J. Hazard. Mater.* **2008**, *160* (2), 435–440. https://doi.org/10.1016/j.jhazmat.2008.03.016.
(52) Kim, K. B.; Kim, H.; Song, E. J.; Kim, S.; Noh, I.; Kim, C. A Cap-Type Schiff Base Acting as a Fluorescence Sensor for Zinc(II) and a Colorimetric Sensor for Iron(II), Copper(II), and Zinc(II) in Aqueous Media. *Dalton Trans.* **2013**, *42* (47), 16569. https://doi.org/10.1039/c3dt51916c.
(53) Park, G. J.; Hwang, I. H.; Song, E. J.; Kim, H.; Kim, C. A Colorimetric and Fluorescent Sensor for Sequential Detection of Copper Ion and Cyanide. *Tetrahedron* **2014**, *70* (17), 2822–2828. https://doi.org/10.1016/j.tet.2014.02.055.
(54) Tautges, B.; Or, V.; Garcia, J.; Shaw, J. T.; Louie, A. Y. Preparation of a Conjugation-Ready Thiol Responsive Molecular Switch. *Tetrahedron Lett* **2015**, *56* (47), 6569–6573. https://doi.org/10.1016/j.tetlet.2015.10.019.
(55) Zeng, L.; Miller, E. W.; Pralle, A.; Isacoff, E. Y.; Chang, C. J. A Selective Turn-On Fluorescent Sensor for Imaging Copper in Living Cells. *J. Am. Chem. Soc.* **2006**, *128* (1), 10–11. https://doi.org/10.1021/ja055064u.
(56) Krämer, R. Fluorescent Chemosensors for Cu2+ Ions: Fast, Selective, and Highly Sensitive. *Angew. Chem. Int. Ed.* **1998**, *37* (6), 772–773. https://doi.org/10.1002/(SICI)1521-3773(19980403)37:6<772::AID-ANIE772>3.0.CO;2-Z.
(57) Wan, F.; Sun, H.; Fan, S. Design of a portable UV-Vis spectrophotometer. *Guang Pu Xue Yu Guang Pu Fen Xi* **2006**, *26* (4), 779–783.

(58) Teixeira Alves Duarte, L. G.; Coelho, F. L.; Germino, J. C.; Gamino da Costa, G.; Berbigier, J. F.; Rodembusch, F. S.; Zambon Atvars, T. D. A Selective Proton Transfer Optical Sensor for Copper II Based on Chelation Enhancement Quenching Effect (CHEQ). *Dyes Pigm.* **2020**, *181*, 108566. https://doi.org/10.1016/j.dyepig.2020.108566.
(59) Sharma, P.; Singh, P. A Perylene Diimide-Based near-IR Ratiometric Sensor for Detection of Cu2+ Ions: Ensemble for Discrimination of CN− and S2− Ions. *Anal. Methods* **2020**, *12* (6), 758–767. https://doi.org/10.1039/C9AY02726B.
(60) Anbu Durai, W.; Ramu, A. Hydrazone Based Dual – Responsive Colorimetric and Ratiometric Chemosensor for the Detection of Cu2+/ F- Ions: DNA Tracking, Practical Performance in Environmental Samples and Tooth Paste. *J. Fluoresc.* **2020**, *30* (2), 275–289. https://doi.org/10.1007/s10895-020-02488-0.
(61) Tavallali, H.; Deilamy-Rad, G.; Karimi, M. A.; Rahimy, E. A Novel Dye-Based Colorimetric Chemosensors for Sequential Detection of Cu2+ and Cysteine in Aqueous Solution. *Anal. Biochem.* **2019**, *583*, 113376. https://doi.org/10.1016/j.ab.2019.113376.
(62) Xie, D.-H.; Wang, X.-J.; Sun, C.; Han, J. Calix[4]Arene Based 1,3,4-Oxadiazole as a Fluorescent Chemosensor for Copper(II) Ion Detection. *Tetrahedron Lett.* **2016**, *57* (51), 5834–5836. https://doi.org/10.1016/j.tetlet.2016.11.051.
(63) Hsieh, Y.-C.; Chir, J.-L.; Yang, S.-T.; Chen, S.-J.; Hu, C.-H.; Wu, A.-T. A Sugar-Aza-Crown Ether-Based Fluorescent Sensor for Cu2+ and Hg2+ Ions. *Carbohydr. Res.* **2011**, *346* (7), 978–981. https://doi.org/10.1016/j.carres.2011.03.010.
(64) Ho, F.-C.; Huang, Y.-J.; Weng, C.-C.; Wu, C.-H.; Li, Y.-K.; Wu, J. I.; Lin, H.-C. Efficient FRET Approaches toward Copper(II) and Cyanide Detections via Host–Guest Interactions of Photo-Switchable [2]Pseudo-Rotaxane Polymers Containing Naphthalimide and Merocyanine Moieties. *ACS Appl. Mater. Interfaces* **2020**, *12* (47), 53257–53273. https://doi.org/10.1021/acsami.0c15049.
(65) Bhatt, K. D.; Gupte, H. S.; Makwana, B. A.; Vyas, D. J.; Maity, D.; Jain, V. K. Calix Receptor Edifice; Scrupulous Turn Off Fluorescent Sensor for Fe(III), Co(II) and Cu(II). *J Fluoresc* **2012**, *22* (6), 1493–1500. https://doi.org/10.1007/s10895-012-1086-5.
(66) Costa, A. I.; Barata, P. D.; Fialho, C. B.; Prata, J. V. Highly Sensitive and Selective Fluorescent Probes for Cu(II) Detection Based on Calix[4]Arene-Oxacyclophane Architectures. *Molecules* **2020**, *25* (10), 2456. https://doi.org/10.3390/molecules25102456.
(67) Ding, H.; Liang, C.; Sun, K.; Wang, H.; Hiltunen, J. K.; Chen, Z.; Shen, J. Dithiothreitol-Capped Fluorescent Gold Nanoclusters: An Efficient Probe for Detection of Copper(II) Ions in Aqueous Solution. *Biosens. Bioelectron.* **2014**, *59*, 216–220. https://doi.org/10.1016/j.bios.2014.03.045.
(68) Ding, L.; Zhao, Z.; Li, D.; Wang, X.; Chen, J. An “off-on” Fluorescent Sensor for Copper Ion Using Graphene Quantum Dots Based on Oxidation of l-Cysteine. *Spectrochim. Acta A* **2019**, *214*, 320–325. https://doi.org/10.1016/j.saa.2019.02.048.
(69) Shi, Y.; Liu, Q.; Yuan, W.; Xue, M.; Feng, W.; Li, F. Dye-Assembled Upconversion Nanocomposite for Luminescence Ratiometric in Vivo Bioimaging of Copper Ions. *ACS Appl. Mater. Interfaces* **2019**, *11* (1), 430–436. https://doi.org/10.1021/acsami.8b19961.
(70) Ngamdee, K.; Chaiendoo, K.; Saiyasombat, C.; Busayaporn, W.; Ittisanronnachai, S.; Promarak, V.; Ngeontae, W. Highly Selective Circular Dichroism Sensor Based on D-Penicillamine/Cysteamine-cadmium Sulfide Quantum Dots for Copper (II) Ion Detection. *Spectrochim. Acta A* **2019**, *211*, 313–321. https://doi.org/10.1016/j.saa.2018.12.027.

(71) Wang, Q.; Yu, X.; Zhan, G.; Li, C. Fluorescent Sensor for Selective Determination of Copper Ion Based on N-Acetyl-l-Cysteine Capped CdHgSe Quantum Dots. *Biosens. Bioelectron.* **2014**, *54*, 311–316. https://doi.org/10.1016/j.bios.2013.11.008.
(72) Liu, H.; Jia, L.; Wang, Y.; Wang, M.; Gao, Z.; Ren, X. Ratiometric Fluorescent Sensor for Visual Determination of Copper Ions and Alkaline Phosphatase Based on Carbon Quantum Dots and Gold Nanoclusters. *Anal Bioanal Chem* **2019**, *411* (12), 2531–2543. https://doi.org/10.1007/s00216-019-01693-6.
(73) Wang, Y.; Zhang, C.; Chen, X.; Yang, B.; Yang, L.; Jiang, C.; Zhang, Z. Ratiometric Fluorescent Paper Sensor Utilizing Hybrid Carbon Dots–Quantum Dots for the Visual Determination of Copper Ions. *Nanoscale* **2016**, *8* (11), 5977–5984. https://doi.org/10.1039/C6NR00430J.
(74) Sivaraman, G.; Iniya, M.; Anand, T.; Kotla, N. G.; Sunnapu, O.; Singaravadivel, S.; Gulyani, A.; Chellappa, D. Chemically Diverse Small Molecule Fluorescent Chemosensors for Copper Ion. *Coord Chem Rev* **2018**, *357*, 50–104. https://doi.org/10.1016/j.ccr.2017.11.020.
(75) Liu, S.; Wang, Y.-M.; Han, J. Fluorescent Chemosensors for Copper(II) Ion: Structure, Mechanism and Application. *J. Photochem. Photobiol. C* **2017**, *32*, 78–103. https://doi.org/10.1016/j.jphotochemrev.2017.06.002.
(76) Kumar, N.; Bhalla, V.; Kumar, M. Resonance Energy Transfer-Based Fluorescent Probes for Hg2+, Cu2+ and Fe2+/Fe3+ Ions. *Analyst* **2013**, *139* (3), 543–558. https://doi.org/10.1039/C3AN01896B.
(77) Saleem, M.; Rafiq, M.; Hanif, M.; Shaheen, M. A.; Seo, S.-Y. A Brief Review on Fluorescent Copper Sensor Based on Conjugated Organic Dyes. *J Fluoresc* **2018**, *28* (1), 97–165. https://doi.org/10.1007/s10895-017-2178-z.
(78) Sharma, S.; Ghosh, K. S. Recent Advances (2017–20) Inthe Detection of Copper Ion by Using Fluorescence Sensors Working through Transfer of Photo-Induced Electron (PET), Excited-State Intramolecular Proton (ESIPT) and Förster Resonance Energy (FRET). *Spectrochim. Acta A* **2021**, *254*, 119610. https://doi.org/10.1016/j.saa.2021.119610.
(79) Chowdhury, S.; Rooj, B.; Dutta, A.; Mandal, U. Review on Recent Advances in Metal Ions Sensing Using Different Fluorescent Probes. *J Fluoresc* **2018**, *28* (4), 999–1021. https://doi.org/10.1007/s10895-018-2263-y.
(80) Chopra, T.; Sasan, S.; Devi, L.; Parkesh, R.; Kapoor, K. K. A Comprehensive Review on Recent Advances in Copper Sensors. *Coord. Chem. Rev.* **2022**, *470*, 214704. https://doi.org/10.1016/j.ccr.2022.214704.
(81) Liu, B.; Zhuang, J.; Wei, G. Recent Advances in the Design of Colorimetric Sensors for Environmental Monitoring. *Environ. Sci.: Nano* **2020**, *7* (8), 2195–2213. https://doi.org/10.1039/D0EN00449A.
(82) Gerdan, Z.; Saylan, Y.; Denizli, A. Recent Advances of Optical Sensors for Copper Ion Detection. *Micromachines* **2022**, *13* (8), 1298. https://doi.org/10.3390/mi13081298.
(83) Hazarika, S. I.; Atta, A. K. Carbohydrate-Based Fluorometric and Colorimetric Sensors for Cu2+ Ion Recognition. *C R Chim* **2019**, *22* (8), 599–613. https://doi.org/10.1016/j.crci.2019.07.003.
(84) Kowser, Z.; Rayhan, U.; Akther, T.; Redshaw, C.; Yamato, T. A Brief Review on Novel Pyrene Based Fluorometric and Colorimetric Chemosensors for the Detection of Cu2+. *Mater. Chem. Front.* **2021**, *5* (5), 2173–2200. https://doi.org/10.1039/D0QM01008A.

(85) Udhayakumari, D.; Naha, S.; Velmathi, S. Colorimetric and Fluorescent Chemosensors for Cu2+. A Comprehensive Review from the Years 2013–15. *Anal. Methods* **2017**, *9* (4), 552–578. https://doi.org/10.1039/C6AY02416E.
(86) Upadhyay, S.; Singh, A.; Sinha, R.; Omer, S.; Negi, K. Colorimetric Chemosensors for D-Metal Ions: A Review in the Past, Present and Future Prospect. *J. Mol. Struct* **2019**, *1193*, 89–102. https://doi.org/10.1016/j.molstruc.2019.05.007.
(87) Kaur, B.; Kaur, N.; Kumar, S. Colorimetric Metal Ion Sensors – A Comprehensive Review of the Years 2011–2016. *Coord. Chem. Rev.* **2018**, *358*, 13–69. https://doi.org/10.1016/j.ccr.2017.12.002.
(88) Rasheed, T.; Li, C.; Bilal, M.; Yu, C.; Iqbal, H. M. N. Potentially Toxic Elements and Environmentally-Related Pollutants Recognition Using Colorimetric and Ratiometric Fluorescent Probes. *Sci. Total Environ.* **2018**, *640–641*, 174–193. https://doi.org/10.1016/j.scitotenv.2018.05.232.
(89) Choudhury, N.; De, P. Recent Progress in Pendant Rhodamine-Based Polymeric Sensors for the Detection of Copper, Mercury and Iron Ions. *J. Macromol. Sci. A* **2021**, *58* (12), 835–848. https://doi.org/10.1080/10601325.2021.1960172.
(90) Trevino, K. M.; Wagner, C. R.; Tamura, E. K.; Garcia, J.; Louie, A. Y. Small Molecule Sensors for the Colorimetric Detection of Copper(II): A Review of the Literature from 2010 to 2022. *Dyes Pigm* **2022**, 110881. https://doi.org/10.1016/j.dyepig.2022.110881.
(91) Liu, Y.; Sun, Y.; Du, J.; Lv, X.; Zhao, Y.; Chen, M.; Wang, P.; Guo, W. Highly Sensitive and Selective Turn-on Fluorescent and Chromogenic Probe for Cu2+ and ClO− Based on a N-Picolinyl Rhodamine B-Hydrazide Derivative. *Org. Biomol. Chem.* **2011**, *9* (2), 432–437. https://doi.org/10.1039/C0OB00411A.
(92) Mi, Y.-S.; Cao, Z.; Chen, Y.-T.; Xie, Q.-F.; Xu, Y.-Y.; Luo, Y.-F.; Shi, J.-J.; Xiang, J.-N. Determination of Trace Amount of Cu2+ with a Multi-Responsive Colorimetric and Reversible Chemosensor. *Analyst* **2013**, *138* (18), 5274. https://doi.org/10.1039/c3an00741c.
(93) Liu, A.; Yang, L.; Zhang, Z.; Zhang, Z.; Xu, D. A Novel Rhodamine-Based Colorimetric and Fluorescent Sensor for the Dual-Channel Detection of Cu2+ and Fe3+ in Aqueous Solutions. *Dyes Pigm.* **2013**, *99* (2), 472–479. https://doi.org/10.1016/j.dyepig.2013.06.007.
(94) Xie, P.; Zhu, Y.; Huang, X.; Gao, G.; Wei, F.; Guo, F.; Jiang, S.; Wang, C. A Novel Probe Based on Rhodamine 101 Spirolactam and 2-(2′-Hydroxy-5′-Methylphenyl)Benzothiazole Moieties for Three-in-One Detection of Paramagnetic Cu2+, Co2+ and Ni2+. *Spectrochim. Acta A* **2019**, *222*, 117171. https://doi.org/10.1016/j.saa.2019.117171.
(95) Nair, R. R.; Raju, M.; Patel, N. P.; Raval, I. H.; Suresh, E.; Haldar, S.; Chatterjee, P. B. Naked Eye Instant Reversible Sensing of Cu2+ and Its in Situ Imaging in Live Brine Shrimp Artemia. *Analyst* **2015**, *140* (16), 5464–5468. https://doi.org/10.1039/C5AN00957J.
(96) Deepa, A.; Srinivasadesikan, V.; Lee, S.-L.; Padmini, V. Highly Selective and Sensitive Colorimetric and Fluorimetric Sensor for Cu2+. *J Fluoresc* **2020**, *30* (1), 3–10. https://doi.org/10.1007/s10895-019-02450-9.
(97) Long, C.; Hu, J.-H.; Fu, Q.-Q.; Ni, P.-W. A New Colorimetric and Fluorescent Probe Based on Rhodamine B Hydrazone Derivatives for Cyanide and Cu2+ in Aqueous Media and Its Application in Real Life. *Spectrochim. Acta A* **2019**, *219*, 297–306. https://doi.org/10.1016/j.saa.2019.04.052.

(98) Gupta, V. K.; Mergu, N.; Kumawat, L. K. A New Multifunctional Rhodamine-Derived Probe for Colorimetric Sensing of Cu(II) and Al(III) and Fluorometric Sensing of Fe(III) in Aqueous Media. *Sens. Actuators B Chem.* **2016**, *223*, 101–113. https://doi.org/10.1016/j.snb.2015.09.060.
(99) Wang, Y.; Wu, H.; Wu, W.-N.; Mao, X.-J.; Zhao, X.-L.; Xu, Z.-Q.; Xu, Z.-H.; Fan, Y.-C. Novel Rhodamine-Based Colorimetric and Fluorescent Sensor for the Dual-Channel Detection of Cu2+ and Co2+/Trivalent Metal Ions and Its AIRE Activities. *Spectrochim. Acta A* **2019**, *212*, 1–9. https://doi.org/10.1016/j.saa.2018.12.017.
(100) Chan, W. C.; Saad, H. M.; Sim, K. S.; Lee, V. S.; Ang, C. W.; Yeong, K. Y.; Tan, K. W. A Rhodamine Based Chemosensor for Solvent Dependent Chromogenic Sensing of Cobalt (II) and Copper (II) Ions with Good Selectivity and Sensitivity: Synthesis, Filter Paper Test Strip, DFT Calculations and Cytotoxicity. *Spectrochim. Acta A* **2021**, *262*, 120099. https://doi.org/10.1016/j.saa.2021.120099.
(101) Wang, Z.-G.; Wang, Y.; Ding, X.-J.; Sun, Y.-X.; Liu, H.-B.; Xie, C.-Z.; Qian, J.; Li, Q.-Z.; Xu, J.-Y. A Highly Selective Colorimetric and Fluorescent Probe for Quantitative Detection of Cu2+/Co2+: The Unique on-off-on Fluorimetric Detection Strategy and Applications in Living Cells/Zebrafish. *Spectrochim. Acta A* **2020**, *228*, 117763. https://doi.org/10.1016/j.saa.2019.117763.
(102) Fang, H.; Huang, P.-C.; Wu, F.-Y. A Novel Jointly Colorimetric and Fluorescent Sensor for Cu2+ Recognition and Its Complex for Sensing S2− by a Cu2+ Displacement Approach in Aqueous Media. *Spectrochim. Acta A* **2018**, *204*, 568–575. https://doi.org/10.1016/j.saa.2018.06.068.
(103) Su, J.-X.; Wang, X.-T.; Chang, J.; Wu, G.-Y.; Wang, H.-M.; Yao, H.; Lin, Q.; Zhang, Y.-M.; Wei, T.-B. Colorimetric and Fluorescent Chemosensor for Highly Selective and Sensitive Relay Detection of Cu2+ and H2PO4− in Aqueous Media. *Spectrochim. Acta A* **2017**, *182*, 67–72. https://doi.org/10.1016/j.saa.2017.03.071.
(104) Zhang, X.; Shen, L.-Y.; Zhang, Q.-L.; Yang, X.-J.; Huang, Y.-L.; Redshaw, C.; Xu, H. A Simple Turn-off Schiff Base Fluorescent Sensor for Copper (II) Ion and Its Application in Water Analysis. *Molecules* **2021**, *26* (5), 1233. https://doi.org/10.3390/molecules26051233.
(105) Fu, Y.; Fan, C.; Liu, G.; Pu, S. A Colorimetric and Fluorescent Sensor for Cu2+ and F− Based on a Diarylethene with a 1,8-Naphthalimide Schiff Base Unit. *Sens. Actuators B Chem.* **2017**, *239*, 295–303. https://doi.org/10.1016/j.snb.2016.08.020.
(106) Yeh, J.-T.; Chen, W.-C.; Liu, S.-R.; Wu, S.-P. A Coumarin-Based Sensitive and Selective Fluorescent Sensor for Copper(II) Ions. *NJC* **2014**, *38* (9), 4434–4439. https://doi.org/10.1039/C4NJ00695J.
(107) Manna, A. K.; Mondal, J.; Rout, K.; Patra, G. K. A Benzohydrazide Based Two-in-One Ni2+/Cu2+ Fluorescent Colorimetric Chemosensor and Its Applications in Real Sample Analysis and Molecular Logic Gate. *Sens. Actuators B Chem.* **2018**, *275*, 350–358. https://doi.org/10.1016/j.snb.2018.08.060.
(108) Kim, M. S.; Lee, S. Y.; Jung, J. M.; Kim, C. A New Schiff-Base Chemosensor for Selective Detection of Cu2+ and Co2+ and Its Copper Complex for Colorimetric Sensing of S2- in Aqueous Solution. *Photochem. Photobiol. Sci.* **2017**, *16* (11), 1677–1689. https://doi.org/10.1039/C7PP00229G.
(109) Peralta-Domínguez, D.; Rodriguez, M.; Ramos-Ortiz, G.; Maldonado, J. L.; Luna-Moreno, D.; Ortiz-Gutierrez, M.; Barba, V. A Schiff Base Derivative Used as Sensor of

Copper through Colorimetric and Surface Plasmon Resonance Techniques. *Sens. Actuators B Chem.* **2016**, *225*, 221–227. https://doi.org/10.1016/j.snb.2015.11.013.
(110) Mathivanan, M.; Tharmalingam, B.; Mani, K. S.; Thiagarajan, V.; Murugesapandian, B. Simple C3-Symmetric Triaminoguanidine-Triphenylamine Conjugate as an Efficient Colorimetric Sensor for Cu(II) and Fluorescent Sensor for Fe(III) Ions. *Spectrochim. Acta A* **2020**, *234*, 118235. https://doi.org/10.1016/j.saa.2020.118235.
(111) Kumar, R.; Jain, H.; Gahlyan, P.; Joshi, A.; Ramachandran, C. N. A Highly Sensitive Pyridine-Dicarbohydrazide Based Chemosensor for Colorimetric Recognition of Cu2+ , AMP2−, F− and AcO− Ions. *NJC* **2018**, *42* (11), 8567–8576. https://doi.org/10.1039/C8NJ00918J.
(112) Liu, Y.-L.; Yang, L.; Li, P.; Li, S.-J.; Li, L.; Pang, X.-X.; Ye, F.; Fu, Y. A Novel Colorimetric and "Turn-off" Fluorescent Probe Based on Catalyzed Hydrolysis Reaction for Detection of Cu2+ in Real Water and in Living Cells. *Spectrochim. Acta A* **2020**, *227*, 117540. https://doi.org/10.1016/j.saa.2019.117540.
(113) Guo, Z.; Niu, Q.; Li, T.; Sun, T.; Chi, H. A Fast, Highly Selective and Sensitive Colorimetric and Fluorescent Sensor for Cu2+ and Its Application in Real Water and Food Samples. *Spectrochim. Acta A* **2019**, *213*, 97–103. https://doi.org/10.1016/j.saa.2019.01.044.
(114) Mani, K. S.; Rajamanikandan, R.; Murugesapandian, B.; Shankar, R.; Sivaraman, G.; Ilanchelian, M.; Rajendran, S. P. Coumarin Based Hydrazone as an ICT-Based Fluorescence Chemosensor for the Detection of Cu2+ Ions and the Application in HeLa Cells. *Spectrochim. Acta A* **2019**, *214*, 170–176. https://doi.org/10.1016/j.saa.2019.02.020.
(115) Hanmeng, O.; Chailek, N.; Charoenpanich, A.; Phuekvilai, P.; Yookongkaew, N.; Sanmanee, N.; Sirirak, J.; Swanglap, P.; Wanichacheva, N. Cu2+-Selective NIR Fluorescence Sensor Based on Heptamethine Cyanine in Aqueous Media and Its Application. *Spectrochim. Acta A* **2020**, *240*, 118606. https://doi.org/10.1016/j.saa.2020.118606.
(116) Mohammadi, A.; Ghasemi, Z. A Simple Pyrimidine Based Colorimetric and Fluorescent Chemosensor for Sequential Detection of Copper (II) and Cyanide Ions and Its Application in Real Samples. *Spectrochim. Acta A* **2020**, *228*, 117730. https://doi.org/10.1016/j.saa.2019.117730.
(117) Lin, W.-C.; Wu, C.-Y.; Liu, Z.-H.; Lin, C.-Y.; Yen, Y.-P. A New Selective Colorimetric and Fluorescent Sensor for Hg2+ and Cu2+ Based on a Thiourea Featuring a Pyrene Unit. *Talanta* **2010**, *81* (4–5), 1209–1215. https://doi.org/10.1016/j.talanta.2010.02.012.
(118) Jung, J. Y.; Kang, M.; Chun, J.; Lee, J.; Kim, J.; Kim, J.; Kim, Y.; Kim, S.-J.; Lee, C.; Yoon, J. A Thiazolothiazole Based Cu2+ Selective Colorimetric and Fluorescent Sensor via Unique Radical Formation. *Chem. Commun.* **2013**, *49* (2), 176–178. https://doi.org/10.1039/C2CC36626F.
(119) Bayindir, S.; Toprak, M. A Novel Pyrene-Based Selective Colorimetric and Ratiometric Turn-on Sensing for Copper. *Spectrochim. Acta A* **2019**, *213*, 6–11. https://doi.org/10.1016/j.saa.2019.01.053.
(120) Lin, Q.; Chen, P.; Liu, J.; Fu, Y.-P.; Zhang, Y.-M.; Wei, T.-B. Colorimetric Chemosensor and Test Kit for Detection Copper(II) Cations in Aqueous Solution with Specific Selectivity and High Sensitivity. *Dyes Pigm.* **2013**, *98* (1), 100–105. https://doi.org/10.1016/j.dyepig.2013.01.024.

(121) Na, S.; Jin, J. Y.; Wang, H.; Zhang, Y.; Yang, R. H.; Chan, W. H. Tunable Photochromism of Spirobenzopyran via Selective Metal Ion Coordination: An Efficient Visual and Ratioing Fluorescent Probe for Divalent Copper Ion. *Anal. Chem.* **2008**, *80* (9), 3466–3475. https://doi.org/10.1021/ac800072y.
(122) Wang, Y.; Xu, Z.; Dai, X.; Li, H.; Yu, S.; Meng, W. A New Spiropyran-Based Sensor for Colorimetric and Fluorescent Detection of Divalent Cu2+ and Hg2+ Ions and Trivalent Ce3+, Cr3+ and Al3+ Ions. *J Fluoresc* **2019**, *29* (3), 569–575. https://doi.org/10.1007/s10895-019-02372-6.
(123) Kumbhar, H. S.; Gadilohar, B. L.; Shankarling, G. S. A Highly Selective Quinaldine–Indole Based Spiropyran with Intramolecular H-Bonding for Visual Detection of Cu(II) Ions. *Sens. Actuators B Chem.* **2016**, *222*, 35–42. https://doi.org/10.1016/j.snb.2015.08.025.
(124) Kumar, A.; Kumar, S. A Benzothiazolinic Spiropyran for Highly Selective, Sensitive and Visible Light Controlled Detection of Copper Ions in Aqueous Solution. *J. Photochem. Photobiol., A* **2020**, *390*, 112265. https://doi.org/10.1016/j.jphotochem.2019.112265.
(125) Shiraishi, Y.; Tanaka, K.; Hirai, T. Colorimetric Sensing of Cu(II) in Aqueous Media with a Spiropyran Derivative via a Oxidative Dehydrogenation Mechanism. *ACS Appl. Mater. Interfaces* **2013**, *5* (8), 3456–3463. https://doi.org/10.1021/am4005804.
(126) Kim, I.; Jeong, D.-C.; Lee, M.; Khaleel, Z. H.; Satheeshkumar, C.; Song, C. Triazole-Conjugated Spiropyran: Synthesis, Selectivity toward Cu(II), and Binding Study. *Tetrahedron Lett* **2015**, *56* (44), 6080–6084. https://doi.org/10.1016/j.tetlet.2015.09.055.
(127) Xue, Y.; Gong, P.; Tian, J. Specific Recognition of Cu2+ by Simple Spiropyran via Forming a Ternary Complex of Spiropyran-Cu2+-DMF. *Colloids Surf, A Physicochem Eng Asp* **2018**, *541*, 165–174. https://doi.org/10.1016/j.colsurfa.2018.01.017.
(128) Guo, Z.-Q.; Chen, W.-Q.; Duan, X.-M. Highly Selective Visual Detection of Cu(II) Utilizing Intramolecular Hydrogen Bond-Stabilized Merocyanine in Aqueous Buffer Solution. *Org. Lett.* **2010**, *12* (10), 2202–2205. https://doi.org/10.1021/ol100381g.
(129) Parr, R. G.; Pearson, R. G. Absolute Hardness: Companion Parameter to Absolute Electronegativity. *J. Am. Chem. Soc.* **1983**, *105* (26), 7512–7516. https://doi.org/10.1021/ja00364a005.
(130) Hancock, R. D.; Martell, A. E. Lewis Acid–Base Behavior in Aqueous Solution: Some Implications for Metal Ions in Biology. In *Advances in Inorganic Chemistry*; Sykes, A. G., Ed.; Academic Press, 1995; Vol. 42, pp 89–146. https://doi.org/10.1016/S0898-8838(08)60052-5.
(131) Sinn, E.; Harris, C. M. Schiff Base Metal Complexes as Ligands. *Coord Chem Rev* **1969**, *4* (4), 391–422. https://doi.org/10.1016/S0010-8545(00)80080-6.
(132) Yamada, S. Advancement in Stereochemical Aspects of Schiff Base Metal Complexes. *Coord Chem Rev* **1999**, *190–192*, 537–555. https://doi.org/10.1016/S0010-8545(99)00099-5.
(133) Cozzi, P. G.; Dolci, L. S.; Garelli, A.; Montalti, M.; Prodi, L.; Zaccheroni, N. Photophysical Poperties of Schiff-Base Metal Complexes. *NJC* **2003**, *27* (4), 692–697. https://doi.org/10.1039/B209396K.
(134) Hameed, A.; al-Rashida, M.; Uroos, M.; Abid Ali, S.; Khan, K. M. Schiff Bases in Medicinal Chemistry: A Patent Review (2010-2015). *Expert Opin. Ther. Pat.* **2017**, *27* (1), 63–79. https://doi.org/10.1080/13543776.2017.1252752.

(135) Dash, A. C.; Dash, B.; Praharaj, S. Hydrolysis of Imines: Kinetics and Mechanism of Spontaneous Acid-, Base-, and Metal Ion-Induced Hydrolysis of N-Salicylidene-2-Aminothiazole. *J. Chem. Soc., Dalton Trans.* **1981**, No. 10, 2063–2069. https://doi.org/10.1039/DT9810002063.
(136) Chattopadhyay, S.; Chakraborty, P.; Drew, M. G. B.; Ghosh, A. Nickel(II) Complexes of Terdentate or Symmetrical Tetradentate Schiff Bases: Evidence of the Influence of the Counter Anions in the Hydrolysis of the Imine Bond in Schiff Base Complexes. *Inorg. Chim. Acta* **2009**, *362* (2), 502–508. https://doi.org/10.1016/j.ica.2008.05.004.
(137) Cano, J.; Benito, A.; Martínez-Máñez, R.; Soto, J.; Payá, J.; Lloret, F.; Julve, M.; Dolores Marcos, M.; Sinn, E. Ferrocene Containing Chelating Ligands 3. Synthesis, Spectroscopic Characterization, Electrochemical Behaviour and Interaction with Metal Ions of New Ligands Obtained by Condensation of Ferrocenecarboxaldehyde with 2-Amino-Benzoic Acid Derivatives. Crystal Structures of 2-Ferrocenylmethylamino-5-Methyl-Benzoic Acid and 2-Bis(Ferrocenylmethyl)Ammonium-5-Methyl-Benzoic Acid Perchlorate. *Inorg. Chim. Acta* **1995**, *231* (1), 45–56. https://doi.org/10.1016/0020-1693(94)04318-P.
(138) An, R.; Zhang, D.; Chen, Y.; Cui, Y. A "Turn-on" Fluorescent and Colorimetric Sensor for Selective Detection of Cu2+ in Aqueous Media and Living Cells. *Sens. Actuators B Chem.* **2016**, *222*, 48–54. https://doi.org/10.1016/j.snb.2015.08.035.
(139) Hu, Y.; Chen, A.; Kong, Z.; Sun, D. A Reversible Colorimetric and Fluorescence "Turn-Off" Chemosensor for Detection of Cu2+ and Its Application in Living Cell Imaging. *Molecules* **2019**, *24* (23), 4283. https://doi.org/10.3390/molecules24234283.
(140) Wang, H.-H.; Xue, L.; Fang, Z.-J.; Li, G.-P.; Jiang, H. A Colorimetric and Fluorescent Chemosensor for Copper Ions in Aqueous Media and Its Application in Living Cells. *NJC* **2010**, *34* (7), 1239. https://doi.org/10.1039/c0nj00168f.
(141) Maity, D.; Manna, A. K.; Karthigeyan, D.; Kundu, T. K.; Pati, S. K.; Govindaraju, T. Visible-Near-Infrared and Fluorescent Copper Sensors Based on Julolidine Conjugates: Selective Detection and Fluorescence Imaging in Living Cells. *Chem. Eur. J.* **2011**, *17* (40), 11152–11161. https://doi.org/10.1002/chem.201101906.
(142) Gouanvé, F.; Schuster, T.; Allard, E.; Méallet-Renault, R.; Larpent, C. Fluorescence Quenching upon Binding of Copper Ions in Dye-Doped and Ligand-Capped Polymer Nanoparticles: A Simple Way to Probe the Dye Accessibility in Nano-Sized Templates. *Adv. Funct. Mater.* **2007**, *17* (15), 2746–2756. https://doi.org/10.1002/adfm.200601056.
(143) Herten, D.-P.; Haderspeck, A.; Braun, F.; Wadepohl, H. Copper(II)-Induced Fluorescence Quenching of a BODIPY Fluorophore. *J. Inorg. and Gen. Chem.* **2018**, *644* (14), 735–739. https://doi.org/10.1002/zaac.201800154.
(144) Paul, A.; Anbu, S.; Sharma, G.; Kuznetsov, M. L.; Guedes da Silva, M. F. C.; Koch, B.; Pombeiro, A. J. L. Intracellular Detection of Cu2+ and S2- Ions through a Quinazoline Functionalized Benzimidazole-Based New Fluorogenic Differential Chemosensor. *Dalton Trans.* **2015**, *44* (38), 16953–16964. https://doi.org/10.1039/C5DT02662H.
(145) Kaur, M.; Ahn, Y.-H.; Choi, K.; Cho, M. J.; Choi, D. H. A Bifunctional Colorimetric Fluorescent Probe for Hg2+ and Cu2+ Based on a Carbazole–Pyrimidine Conjugate: Chromogenic and Fluorogenic Recognition on TLC, Silica-Gel and Filter Paper. *Org. Biomol. Chem.* **2015**, *13* (26), 7149–7153. https://doi.org/10.1039/C5OB00907C.
(146) Zhou, Z.; Chen, S.; Huang, Y.; Gu, B.; Li, J.; Wu, C.; Yin, P.; Zhang, Y.; Li, H. Simultaneous Visualization and Quantification of Copper (II) Ions in Alzheimer's Disease

by a near-Infrared Fluorescence Probe. *Biosens. Bioelectron.* **2022**, *198*, 113858. https://doi.org/10.1016/j.bios.2021.113858.
(147) Gao, Q.; Ji, L.; Wang, Q.; Yin, K.; Li, J.; Chen, L. Colorimetric Sensor for Highly Sensitive and Selective Detection of Copper Ion. *Anal. Methods* **2017**, *9* (35), 5094–5100. https://doi.org/10.1039/C7AY01335C.
(148) Mohammadi, A.; Khalili, B.; Haghayegh, A. S. A Novel Chromone Based Colorimetric Sensor for Highly Selective Detection of Copper Ions: Synthesis, Optical Properties and DFT Calculations. *Spectrochim. Acta A* **2019**, *222*, 117193. https://doi.org/10.1016/j.saa.2019.117193.
(149) Ciarrocchi, C.; Tumino, A.; Sacchi, D.; Orbelli Biroli, A.; Licchelli, M. Detection of Copper(II) in Water by Methylene Blue Derivatives. *Chem Phys Chem* **2020**, *21* (21), 2432–2440. https://doi.org/10.1002/cphc.202000676.
(150) Aydin, Z.; Keles, M. Colorimetric Detection of Copper(II) Ions Using Schiff-Base Derivatives. *ChemistrySelect* **2020**, *5* (25), 7375–7381. https://doi.org/10.1002/slct.202001041.
(151) Milindanuth, P.; Pisitsak, P. A Novel Colorimetric Sensor Based on Rhodamine-B Derivative and Bacterial Cellulose for the Detection of Cu(II) Ions in Water. *Mater. Chem. Phys.* **2018**, *216*, 325–331. https://doi.org/10.1016/j.matchemphys.2018.06.003.
(152) Trevino, K. M.; Tautges, B. K.; Kapre, R.; Franco Jr, F. C.; Or, V. W.; Balmond, E. I.; Shaw, J. T.; Garcia, J.; Louie, A. Y. Highly Sensitive and Selective Spiropyran-Based Sensor for Copper(II) Quantification. *ACS Omega* **2021**, *6* (16), 10776–10789. https://doi.org/10.1021/acsomega.1c00392.
(153) Balmond, E. I.; Tautges, B. K.; Faulkner, A. L.; Or, V. W.; Hodur, B. M.; Shaw, J. T.; Louie, A. Y. Comparative Evaluation of Substituent Effect on the Photochromic Properties of Spiropyrans and Spirooxazines. *J. Org. Chem.* **2016**, *81* (19), 8744–8758. https://doi.org/10.1021/acs.joc.6b01193.
(154) Shao, N.; Zhang, Y.; Cheung, S.; Yang, R.; Chan, W.; Mo, T.; Li, K.; Liu, F. Copper Ion-Selective Fluorescent Sensor Based on the Inner Filter Effect Using a Spiropyran Derivative. *Anal. Chem.* **2005**, *77* (22), 7294–7303. https://doi.org/10.1021/ac051010r.
(155) Natali, M.; Soldi, L.; Giordani, S. A Photoswitchable Zn (II) Selective Spiropyran-Based Sensor. *Tetrahedron* **2010**, *66* (38), 7612–7617. https://doi.org/10.1016/j.tet.2010.07.035.
(156) Ford, E. S. Serum Copper Concentration and Coronary Heart Disease among US Adults. *Am. J. Epidemiol.* **2000**, *151* (12), 1182–1188. https://doi.org/10.1093/oxfordjournals.aje.a010168.
(157) Pieper, K. J.; Martin, R.; Tang, M.; Walters, L.; Parks, J.; Roy, S.; Devine, C.; Edwards, M. A. Evaluating Water Lead Levels During the Flint Water Crisis. *Environ. Sci. Technol.* **2018**, *52* (15), 8124–8132. https://doi.org/10.1021/acs.est.8b00791.
(158) Singha, D.; Das, T.; Satyanarayana, L.; Roy, P.; Nandi, M. Rhodamine Functionalized Mesoporous Silica as a Chemosensor for the Efficient Sensing of Al3+, Cr3+ and Fe3+ Ions and Their Removal from Aqueous Media. *New J. Chem.* **2019**, *43* (39), 15563–15574. https://doi.org/10.1039/C9NJ03010G.
(159) Kim, H. N.; Ren, W. X.; Kim, J. S.; Yoon, J. Fluorescent and Colorimetric Sensors for Detection of Lead, Cadmium, and Mercury Ions. *Chem. Soc. Rev.* **2012**, *41* (8), 3210–3244. https://doi.org/10.1039/C1CS15245A.
(160) Jones, J. B.; Dodds, D. R. Enzymes in Organic Synthesis. Preparation and Characterization of Potential Decalindione Substrates of Horse Liver Alcohol

Dehydrogenase. *Can. J. Chem.* **1987**, *65* (10), 2397–2404. https://doi.org/10.1139/v87-400.
(161) Tatay, S.; Haque, S. A.; O'Regan, B.; Durrant, J. R.; Verhees, W. J. H.; Kroon, J. M.; Vidal-Ferran, A.; Gaviña, P.; Palomares, E. Kinetic Competition in Liquid Electrolyte and Solid-State Cyanine Dye Sensitized Solar Cells. *J. Mater. Chem.* **2007**, *17* (29), 3037–3044. https://doi.org/10.1039/B703750C.
(162) Potisek, S. L.; Davis, D. A.; Sottos, N. R.; White, S. R.; Moore, J. S. Mechanophore-Linked Addition Polymers. *J. Am. Chem. Soc.* **2007**, *129* (45), 13808–13809. https://doi.org/10.1021/ja076189x.
(163) De Almeida, M. V.; Figueiredo, R. M.; Dos Santos, H. F.; Da Silva, A. D.; De Almeida, W. B. Synthesis and Theoretical Study of Azido and Amino Inositol Derivatives from L-Quebrachitol. *Tetrahedron Lett.* **2001**, *42* (15), 2767–2769. https://doi.org/10.1016/S0040-4039(01)00326-4.
(164) Cassella, R. J.; Brum, D. M.; Lima, C. F.; Fonseca, T. C. O. Direct Determination of Cu and Fe in Jet Fuel by Electrothermal Atomic Absorption Spectrometry with Injection of Sample as Detergent Emulsions. *Fuel* **2011**, *90* (3), 1215–1220. https://doi.org/10.1016/j.fuel.2010.12.008.
(165) Heng, S.; Reineck, P.; Vidanapathirana, A. K.; Pullen, B. J.; Drumm, D. W.; Ritter, L. J.; Schwarz, N.; Bonder, C. S.; Psaltis, P. J.; Thompson, J. G.; Gibson, B. C.; Nicholls, S. J.; Abell, A. D. Rationally Designed Probe for Reversible Sensing of Zinc and Application in Cells. *ACS Omega* **2017**, *2* (9), 6201–6210. https://doi.org/10.1021/acsomega.7b00923.
(166) Wu, G.; Lupton, J. R.; Turner, N. D.; Fang, Y.-Z.; Yang, S. Glutathione Metabolism and Its Implications for Health. *J Nutr* **2004**, *134* (3), 489–492. https://doi.org/10.1093/jn/134.3.489.
(167) Montero, D.; Tachibana, C.; Rahr Winther, J.; Appenzeller-Herzog, C. Intracellular Glutathione Pools Are Heterogeneously Concentrated. *Redox Biol* **2013**, *1* (1), 508–513. https://doi.org/10.1016/j.redox.2013.10.005.
(168) Forman, H. J.; Zhang, H.; Rinna, A. Glutathione: Overview of Its Protective Roles, Measurement, and Biosynthesis. *Mol Aspects Med* **2009**, *30* (1–2), 1–12. https://doi.org/10.1016/j.mam.2008.08.006.
(169) Jones, D. P. Redox Potential of GSH/GSSG Couple: Assay and Biological Significance. In *Methods in Enzymology*; Sies, H., Packer, L., Eds.; Protein Sensors and Reactive Oxygen Species - Part B: Thiol Enzymes and Proteins; Academic Press, 2002; Vol. 348, pp 93–112. https://doi.org/10.1016/S0076-6879(02)48630-2.
(170) Griffith, O. W. Biologic and Pharmacologic Regulation of Mammalian Glutathione Synthesis. *Free Radic. Biol. Med.* **1999**, *27* (9), 922–935. https://doi.org/10.1016/S0891-5849(99)00176-8.
(171) Requejo, R.; Hurd, T. R.; Costa, N. J.; Murphy, M. P. Cysteine Residues Exposed on Protein Surfaces Are the Dominant Intramitochondrial Thiol and May Protect against Oxidative Damage. *FEBS J* **2010**, *277* (6), 1465–1480. https://doi.org/10.1111/j.1742-4658.2010.07576.x.
(172) McBean, G. J. Cysteine, Glutathione, and Thiol Redox Balance in Astrocytes. *Antioxidants* **2017**, *6* (3), 62. https://doi.org/10.3390/antiox6030062.
(173) Petri, L.; Ábrányi-Balogh, P.; Varga, P. R.; Imre, T.; Keserű, G. M. Comparative Reactivity Analysis of Small-Molecule Thiol Surrogates. *Bioorg. Med. Chem.* **2020**, *28* (7), 115357. https://doi.org/10.1016/j.bmc.2020.115357.

(174) Owen, J. B.; Butterfield, D. A. Measurement of Oxidized/Reduced Glutathione Ratio. In *Protein Misfolding and Cellular Stress in Disease and Aging: Concepts and Protocols*; Bross, P., Gregersen, N., Eds.; Methods in Molecular Biology; Humana Press: Totowa, NJ, 2010; pp 269–277. https://doi.org/10.1007/978-1-60761-756-3_18.
(175) Pizzino, G.; Irrera, N.; Cucinotta, M.; Pallio, G.; Mannino, F.; Arcoraci, V.; Squadrito, F.; Altavilla, D.; Bitto, A. Oxidative Stress: Harms and Benefits for Human Health. *Oxid Med Cell Longev* **2017**, *2017*, 8416763. https://doi.org/10.1155/2017/8416763.
(176) Christen, Y. Oxidative Stress and Alzheimer Disease. *Am. J. Clin. Nutr.* **2000**, *71* (2), 621S-629S. https://doi.org/10.1093/ajcn/71.2.621s.
(177) Halliwell, B. Role of Free Radicals in the Neurodegenerative Diseases. *Drugs & Aging* **2001**, *18* (9), 685–716. https://doi.org/10.2165/00002512-200118090-00004.
(178) Liguori, I.; Russo, G.; Curcio, F.; Bulli, G.; Aran, L.; Della-Morte, D.; Gargiulo, G.; Testa, G.; Cacciatore, F.; Bonaduce, D.; Abete, P. Oxidative Stress, Aging, and Diseases. *Clin Interv Aging* **2018**, *13*, 757–772. https://doi.org/10.2147/CIA.S158513.
(179) Garcia, J.; Addison, J. B.; Liu, S. Z.; Lu, S.; Faulkner, A. L.; Hodur, B. M.; Balmond, E. I.; Or, V. W.; Yun, J. H.; Trevino, K.; Shen, B.; Shaw, J. T.; Frank, N. L.; Louie, A. Y. Antioxidant Sensing by Spiropyrans: Substituent Effects and NMR Spectroscopic Studies. *J. Phys. Chem. B* **2019**, *123* (31), 6799–6809. https://doi.org/10.1021/acs.jpcb.9b03424.
(180) Trevino, K. M.; Addison, B.; Louie, A. Y.; Garcia, J. Investigating the Interaction between Merocyanine and Glutathione through a Comprehensive NMR Analysis of Three GSH-Stabilized Merocyanine Species. *Magn. Reson. Chem.* **2023**, *61* (8), 487–496. https://doi.org/10.1002/mrc.5369.
(181) Ballatori, N.; Krance, S. M.; Notenboom, S.; Shi, S.; Tieu, K.; Hammond, C. L. Glutathione Dysregulation and the Etiology and Progression of Human Diseases. *Biol Chem* **2009**, *390* (3), 191–214. https://doi.org/10.1515/BC.2009.033.
(182) Schulz, J. B.; Lindenau, J.; Seyfried, J.; Dichgans, J. Glutathione, Oxidative Stress and Neurodegeneration. *Eur. J. Biochem.* **2000**, *267* (16), 4904–4911. https://doi.org/10.1046/j.1432-1327.2000.01595.x.
(183) Mandal, P. K.; Roy, R. G.; Samkaria, A. Oxidative Stress: Glutathione and Its Potential to Protect Methionine-35 of Aβ Peptide from Oxidation. *ACS Omega* **2022**, *7* (31), 27052–27061. https://doi.org/10.1021/acsomega.2c02760.
(184) Shao, N.; Jin, J.; Wang, H.; Zheng, J.; Yang, R.; Chan, W.; Abliz, Z. Design of Bis-Spiropyran Ligands as Dipolar Molecule Receptors and Application to in Vivo Glutathione Fluorescent Probes. *J. Am. Chem. Soc.* **2010**, *132* (2), 725–736. https://doi.org/10.1021/ja908215t.
(185) Li, Y.; Duan, Y.; Li, J.; Zheng, J.; Yu, H.; Yang, R. Simultaneous Nucleophilic-Substituted and Electrostatic Interactions for Thermal Switching of Spiropyran: A New Approach for Rapid and Selective Colorimetric Detection of Thiol-Containing Amino Acids. *Anal. Chem.* **2012**, *84* (11), 4732–4738. https://doi.org/10.1021/ac203494e.
(186) Shao, N.; Jin, J. Y.; Cheung, S. M.; Yang, R. H.; Chan, W. H.; Mo, T. A Spiropyran-Based Ensemble for Visual Recognition and Quantification of Cysteine and Homocysteine at Physiological Levels. *Angew. Chem., Int. Ed. Engl.* **2006**, *45* (30), 4944–4948. https://doi.org/10.1002/anie.200600112.
(187) Heng, S.; Zhang, X.; Pei, J.; Abell, A. D. A Rationally Designed Reversible 'Turn-Off' Sensor for Glutathione. *Biosensors* **2017**, *7* (3), 36. https://doi.org/10.3390/bios7030036.

(188) Shcherbatykh, A. A.; Chernov'yants, M. S.; Voloshin, N. A.; Chernyshev, A. V. Spiropyran 5,6′-Dichloro-1,3,3-Trimethylspiro[Indoline-2,2′-2H-Pyrano[3,2-h]Quinoline] Application as a Spectorphotometric and Fluorescent Probe for Glutathione and Cysteine Sensing. *Chem. Pap.* **2022**, *76* (9), 5541–5550. https://doi.org/10.1007/s11696-022-02259-0.
(189) Delbaere, S.; Vermeersch, G. NMR Spectroscopy Applied to Photochromism Investigations. *J. Photochem. Photobiol. C: Photochem. Rev.* **2008**, *9* (2), 61–80. https://doi.org/10.1016/j.jphotochemrev.2008.04.003.
(190) Su, P.; Wen, L.; Yan, J.; Zheng, K.; Zhang, N. Baso-Chromic Spiropyrrolizine: The Spiromerocyanine Isomerization and Alkaline Detection. *J. Mol. Struct.* **2022**, *1250*, 131631. https://doi.org/10.1016/j.molstruc.2021.131631.
(191) Kießwetter, R.; Pustet, N.; Brandl, F.; Mannschreck, A. 1′,3′,3′-Trimethyl-6-Nitrospiro[2H-1-Benzopyran-2,2′-Indoline]: Its Thermal Enantiomerization and the Equilibration with Its Merocyanine. *Tetrahedron: Asymmetry* **1999**, *10* (24), 4677–4687. https://doi.org/10.1016/S0957-4166(99)00538-8.
(192) Özçoban, C.; Halbritter, T.; Steinwand, S.; Herzig, L.-M.; Kohl-Landgraf, J.; Askari, N.; Groher, F.; Fürtig, B.; Richter, C.; Schwalbe, H.; Suess, B.; Wachtveitl, J.; Heckel, A. Water-Soluble Py-BIPS Spiropyrans as Photoswitches for Biological Applications. *Org. Lett.* **2015**, *17* (6), 1517–1520. https://doi.org/10.1021/acs.orglett.5b00397.
(193) Raymo, F. M.; Giordani, S.; White, A. J. P.; Williams, D. J. Digital Processing with a Three-State Molecular Switch. *J. Org. Chem.* **2003**, *68* (11), 4158–4169. https://doi.org/10.1021/jo0340455.
(194) Moriuchi, A.; Uchida, K.; Inagaki, A.; Akita, M. Photochromic Behavior and Diastereomeric Isomerism in [(H6-Spirobenzopyran)RuCp*]PF6. *Organometallics* **2005**, *24* (26), 6382–6392. https://doi.org/10.1021/om0506771.
(195) Keum, S.-R.; Roh, H.-J.; Choi, Y.-K.; Lim, S.-S.; Kim, S.-H.; Koh, K. Complete 1H and 13C NMR Spectral Assignment of Symmetric and Asymmetric Bis-Spiropyran Derivatives. *Magn Reson Chem* **2005**, *43* (10), 873–876. https://doi.org/10.1002/mrc.1640.
(196) Ozhogin, I. V.; Zolotukhin, P. V.; Tkachev, V. V.; Pugachev, A. D.; Kozlenko, A. S.; Belanova, A. A.; Aldoshin, S. M.; Lukyanov, B. S. Synthesis and Study of New Indoline Spiropyran and Its Derivative with α-Lipoic Acid Exhibiting Low Cytotoxicity. *Russ Chem Bull* **2021**, *70* (7), 1388–1393. https://doi.org/10.1007/s11172-021-3228-x.
(197) Ahmadi, S.; Nasiri, M.; Pourrajab Miandoab, A. Synthesis and Characterization of a pH and Photoresponsive Copolymer of Acrylamide and Spiropyran. *Polym. Adv. Technol.* **2020**, *31* (11), 2545–2551. https://doi.org/10.1002/pat.4981.
(198) Keum, S.-R.; Ahn, S.-M.; Roh, S.-J.; Park, S.-J.; Kim, S.-H.; Koh, K. Dicondensed Indolinobenzospiropyrans as Precursors of Thermo- and Photochromic Spiropyrans. Part II: Assignment of 1H and 13C NMR Spectra. *Magn Reson Chem* **2006**, *44* (1), 90–94. https://doi.org/10.1002/mrc.1718.
(199) Inouye, M.; Ueno, M.; Kitao, T.; Tsuchiya, K. Alkali Metal Recognition Induced Isomerization of Spiropyrans. *J. Am. Chem. Soc.* **1990**, *112* (24), 8977–8979. https://doi.org/10.1021/ja00180a051.
(200) Miguez, F. B.; Moreira, O. B. O.; de Oliveira, M. A. L.; Denadai, Â. M. L.; de Oliveira, L. F. C.; De Sousa, F. B. Reversible Electrospun Fibers Containing Spiropyran for Acid and Base Vapor Sensing. *J. Mater. Res.* **2023**, *38* (2), 547–556. https://doi.org/10.1557/s43578-022-00842-5.

(201) Hobley, J.; Malatesta, V. Energy Barrier to TTC–TTT Isomerisation for the Merocyanine of a Photochromic Spiropyran. *Phys. Chem. Chem. Phys.* **2000**, *2* (1), 57–59. https://doi.org/10.1039/A908360J.
(202) Kozlenko, A. S.; Makarova, N. I.; Ozhogin, I. V.; Pugachev, A. D.; Lukyanova, M. B.; Rostovtseva, I. A.; Borodkin, G. S.; Stankevich, N. V.; Metelitsa, A. V.; Lukyanov, B. S. New Indoline Spiropyrans with Highly Stable Merocyanine Forms. *Mendeleev Commun.* **2021**, *31* (3), 403–406. https://doi.org/10.1016/j.mencom.2021.04.040.
(203) Hobley, J.; Malatesta, V.; Millini, R.; Montanari, L.; Parker, W. O. N.; Vincenzo Malatesta, R. M. Proton Exchange and Isomerisation Reactions of Photochromic and Reverse Photochromic Spiro-Pyrans and Their Merocyanine Forms. *Phys. Chem. Chem. Phys.* **1999**, *1* (14), 3259–3267. https://doi.org/10.1039/A902379H.
(204) Hirano, M.; Miyashita, A.; Shitara, H.; Nohira, H. Synthesis and Photochemical Properties of Novel Spirobenzoselenazolinobenzopyrans. *Chem. Lett.* **1991**, *20* (11), 1873–1876. https://doi.org/10.1246/cl.1991.1873.
(205) Komber, H.; Müllers, S.; Lombeck, F.; Held, A.; Walter, M.; Sommer, M. Soluble and Stable Alternating Main-Chain Merocyanine Copolymers through Quantitative Spiropyran–Merocyanine Conversion. *Polym. Chem.* **2014**, *5* (2), 443–453. https://doi.org/10.1039/C3PY00853C.
(206) Feuerstein, T. J.; Müller, R.; Barner-Kowollik, C.; Roesky, P. W. Investigating the Photochemistry of Spiropyran Metal Complexes with Online LED-NMR. *Inorg. Chem.* **2019**, *58* (22), 15479–15486. https://doi.org/10.1021/acs.inorgchem.9b02547.
(207) Berton, C.; Busiello, D. M.; Zamuner, S.; Solari, E.; Scopelliti, R.; Fadaei-Tirani, F.; Severin, K.; Pezzato, C. Thermodynamics and Kinetics of Protonated Merocyanine Photoacids in Water. *Chem. Sci.* **2020**, *11* (32), 8457–8468. https://doi.org/10.1039/D0SC03152F.
(208) Kathuria, I.; Datta, A.; Kumar, S. A Substituted Benzothiazolinic Merocyanine Derivative as a Reversible, Selective, Colorimetric and Fluorescent Probe for HSO4− in Aqueous Solution. *J. Mol. Struct.* **2022**, *1255*, 132471. https://doi.org/10.1016/j.molstruc.2022.132471.
(209) Pugachev, A. D.; Ozhogin, I. V.; Lukyanova, M. B.; Lukyanov, B. S.; Kozlenko, A. S.; Rostovtseva, I. A.; Makarova, N. I.; Tkachev, V. V.; Aldoshin, S. M.; Metelitsa, A. V. Synthesis, Structure and Photochromic Properties of Indoline Spiropyrans with Electron-Withdrawing Substituents. *J. Mol. Struct.* **2021**, *1229*, 129615. https://doi.org/10.1016/j.molstruc.2020.129615.
(210) Kozlenko, A. S.; Ozhogin, I. V.; Pugachev, A. D.; Rostovtseva, I. A.; Makarova, N. I.; Demidova, N. V.; Tkachev, V. V.; Borodkin, G. S.; Metelitsa, A. V.; El-Sewify, I. M.; Lukyanov, B. S. New Cationic Spiropyrans with Photoswitchable NIR Fluorescence. *Spectrochim. Acta A Mol. Biomol.* **2023**, *297*, 122712. https://doi.org/10.1016/j.saa.2023.122712.
(211) Sharma, D.; Rao, D.; Saha, B. A Photonic Artificial Synapse with a Reversible Multifaceted Photochromic Compound. *Nanoscale Horiz.* **2023**, *8* (4), 543–549. https://doi.org/10.1039/D2NH00532H.
(212) Wolff, C.; Kind, J.; Schenderlein, H.; Bartling, H.; Feldmeier, C.; Gschwind, R. M.; Biesalski, M.; Thiele, C. M. Studies of a Photochromic Model System Using NMR with Ex-Situ and in-Situ Irradiation Devices. *Magn Reson Chem* **2016**, *54* (6), 485–491. https://doi.org/10.1002/mrc.4403.

(213) Kortekaas, L.; R. Browne, W. The Evolution of Spiropyran: Fundamentals and Progress of an Extraordinarily Versatile Photochrome. *Chem Soc Rev* **2019**, *48* (12), 3406–3424. https://doi.org/10.1039/C9CS00203K.
(214) Cottone, G.; Noto, R.; La Manna, G. Theoretical Study of Spiropyran–Merocyanine Thermal Isomerization. *Chem. Phys. Lett.* **2004**, *388* (1), 218–222. https://doi.org/10.1016/j.cplett.2004.03.016.
(215) Plewes, D. B.; Kucharczyk, W. Physics of MRI: A Primer. *J. Magn. Reson. Imaging* **2012**, *35* (5), 1038–1054. https://doi.org/10.1002/jmri.23642.
(216) Westbrook, C.; Kaut, C. *MRI in Practice*, 2nd ed.; Wiley, 1998.
(217) Brown, R. W.; Cheng, Y. N.; Haacke, M. E.; Thompson, M. R.; Venkatesan, R. *Magnetic Resonance Imaging: Physical Principles and Sequence Design*, 1st ed.; John Wiley & Sons, Ltd, 2014. https://doi.org/10.1002/9781118633953.
(218) Sodickson, A. D.; Sodickson, D. K. Introductory Magnetic Resonance Imaging Physics. Ch. 18. In *Handbook of Neuro-Oncology Neuroimaging (Second Edition)*; Newton, H. B., Ed.; Academic Press: San Diego, 2016; pp 157–166. https://doi.org/10.1016/B978-0-12-800945-1.00018-5.
(219) Tu, C.; Osborne, E. A.; Louie, A. Y. Activatable T1 and T2 Magnetic Resonance Imaging Contrast Agents. *Ann Biomed Eng* **2011**, *39* (4), 1335–1348. https://doi.org/10.1007/s10439-011-0270-0.
(220) Wahsner, J.; Gale, E. M.; Rodríguez-Rodríguez, A.; Caravan, P. Chemistry of MRI Contrast Agents: Current Challenges and New Frontiers. *Chem Rev* **2019**, *119* (2), 957–1057. https://doi.org/10.1021/acs.chemrev.8b00363.
(221) *Precession of Top*. http://hyperphysics.phy-astr.gsu.edu/hbase/top.html (accessed 2023-07-24).
(222) Brown, R. W.; Cheng, Y. N.; Haacke, M. E.; Thompson, M. R.; Venkatesan, R. Classical Response of a Single Nucleus to a Magnetic Field. In *Magnetic Resonance Imaging: Physical Principles and Sequence Design*; John Wiley & Sons, Ltd, 2014; pp 19–36. https://doi.org/10.1002/9781118633953.ch2.
(223) *Nuclear precession*. Questions and Answers in MRI. http://mriquestions.com/why-precession.html (accessed 2023-07-24).
(224) Preston, D. C. *MRI Basics*. https://case.edu/med/neurology/NR/MRI%20Basics.htm (accessed 2023-07-19).
(225) Turnbull, L. W. Dynamic Contrast-Enhanced MRI in the Diagnosis and Management of Breast Cancer. *NMR Biomed.* **2009**, *22* (1), 28–39. https://doi.org/10.1002/nbm.1273.
(226) van Zelst, J. C. M.; Vreemann, S.; Witt, H.-J.; Gubern-Merida, A.; Dorrius, M. D.; Duvivier, K.; Lardenoije-Broker, S.; Lobbes, M. B. I.; Loo, C.; Veldhuis, W.; Veltman, J.; Drieling, D.; Karssemeijer, N.; Mann, R. M. Multireader Study on the Diagnostic Accuracy of Ultrafast Breast Magnetic Resonance Imaging for Breast Cancer Screening. *Invest. Radiol.* **2018**, *53* (10), 579. https://doi.org/10.1097/RLI.0000000000000494.
(227) Heye, A. K.; Culling, R. D.; Valdés Hernández, M. del C.; Thrippleton, M. J.; Wardlaw, J. M. Assessment of Blood–Brain Barrier Disruption Using Dynamic Contrast-Enhanced MRI. A Systematic Review. *NeuroImage Clin.* **2014**, *6*, 262–274. https://doi.org/10.1016/j.nicl.2014.09.002.
(228) Deike-Hofmann, K.; Reuter, J.; Haase, R.; Paech, D.; Gnirs, R.; Bickelhaupt, S.; Forsting, M.; Heußel, C. P.; Schlemmer, H.-P.; Radbruch, A. Glymphatic Pathway of Gadolinium-

Based Contrast Agents Through the Brain: Overlooked and Misinterpreted. *Invest. Radiol.* **2019**, *54* (4), 229. https://doi.org/10.1097/RLI.0000000000000533.
(229) *Cardiovascular Magnetic Resonance Imaging*; Kwong, R. Y., Ed.; Humana Press: Totowa, NJ, 2008. https://doi.org/10.1007/978-1-59745-306-6.
(230) Gupta, A.; Baradaran, H.; Al-Dasuqi, K.; Knight-Greenfield, A.; Giambrone, A. E.; Delgado, D.; Wright, D.; Teng, Z.; Min, J. K.; Navi, B. B.; Iadecola, C.; Kamel, H. Gadolinium Enhancement in Intracranial Atherosclerotic Plaque and Ischemic Stroke: A Systematic Review and Meta-Analysis. *J Am Heart Assoc* **2016**, *5* (8), e003816. https://doi.org/10.1161/JAHA.116.003816.
(231) Lee, E.; Ibrahim, E.-S. H.; Parwani, P.; Bhave, N.; Stojanovska, J. Practical Guide to Evaluating Myocardial Disease by Cardiac MRI. *Am J Roentgenol* **2020**, *214* (3), 546–556. https://doi.org/10.2214/AJR.19.22076.
(232) Gahramanov, S.; Muldoon, L. L.; Varallyay, C. G.; Li, X.; Kraemer, D. F.; Fu, R.; Hamilton, B. E.; Rooney, W. D.; Neuwelt, E. A. Figure 2: Pseudoprogression of Glioblastoma after Chemo- and Radiation Therapy: Diagnosis by Using Dynamic Susceptibility-Weighted Contrast-Enhanced Perfusion MR Imaging with Ferumoxytol versus Gadoteridol and Correlation with Survival. *Radiology* **2013**, *266* (3), 842–852. https://doi.org/10.1148/radiol.12111472.
(233) Reeßing, F.; Huijsse, S. E. M.; Dierckx, R. A. J. O.; Feringa, B. L.; Borra, R. J. H.; Szymański, W. A Photocleavable Contrast Agent for Light-Responsive MRI. *Pharmaceuticals* **2020**, *13* (10), 296. https://doi.org/10.3390/ph13100296.
(234) Dommaschk, M.; Peters, M.; Gutzeit, F.; Schütt, C.; Näther, C.; Sönnichsen, F. D.; Tiwari, S.; Riedel, C.; Boretius, S.; Herges, R. Photoswitchable Magnetic Resonance Imaging Contrast by Improved Light-Driven Coordination-Induced Spin State Switch. *J. Am. Chem. Soc.* **2015**, *137* (24), 7552–7555. https://doi.org/10.1021/jacs.5b00929.
(235) Tu, C.; Osborne, E. A.; Louie, A. Y. Synthesis and Characterization of a Redox- and Light-Sensitive MRI Contrast Agent. *Tetrahedron* **2009**, *65* (7), 1241. https://doi.org/10.1016/j.tet.2008.12.020.
(236) Tu, C.; Louie, A. Y. Photochromically-Controlled, Reversibly-Activated MRI and Optical Contrast Agent. *Chem Commun* **2007**, No. 13, 1331–1333. https://doi.org/10.1039/b616991k.
(237) Hingorani, D. V.; Yoo, B.; Bernstein, A. S.; Pagel, M. D. Detecting Enzyme Activities with Exogenous MRI Contrast Agents. *Chem. Eur. J.* **2014**, *20* (32), 9840–9850. https://doi.org/10.1002/chem.201402474.
(238) Haedicke, I. E.; Li, T.; Zhu, Y. L. K.; Martinez, F.; Hamilton, A. M.; Murrell, D. H.; Nofiele, J. T.; Cheng, H.-L. M.; Scholl, T. J.; Foster, P. J.; Zhang, X. An Enzyme-Activatable and Cell-Permeable MnIII-Porphyrin as a Highly Efficient T1 MRI Contrast Agent for Cell Labeling. *Chem. Sci.* **2016**, *7* (7), 4308–4317. https://doi.org/10.1039/C5SC04252F.
(239) Nivorozhkin, A. L.; Kolodziej, A. F.; Caravan, P.; Greenfield, M. T.; Lauffer, R. B.; McMurry, T. J. Enzyme-Activated Gd3+ Magnetic Resonance Imaging Contrast Agents with a Prominent Receptor-Induced Magnetization Enhancement. *Angew. Chem. Int. Ed.* **2001**, *40* (15), 2903–2906. https://doi.org/10.1002/1521-3773(20010803)40:15<2903::AID-ANIE2903>3.0.CO;2-N.
(240) Kim, T.; Cho, E.-J.; Chae, Y.; Kim, M.; Oh, A.; Jin, J.; Lee, E.-S.; Baik, H.; Haam, S.; Suh, J.-S.; Huh, Y.-M.; Lee, K. Urchin-Shaped Manganese Oxide Nanoparticles as pH-

Responsive Activatable T1 Contrast Agents for Magnetic Resonance Imaging. *Angew. Chem.* **2011**, *123* (45), 10777–10781. https://doi.org/10.1002/ange.201103108.
(241) Zhu, X.; Xiong, H.; Zhou, Q.; Zhao, Z.; Zhang, Y.; Li, Y.; Wang, S.; Shi, S. A pH-Activatable MnCO3 Nanoparticle for Improved Magnetic Resonance Imaging of Tumor Malignancy and Metastasis. *ACS Appl. Mater. Interfaces* **2021**, *13* (16), 18462–18471. https://doi.org/10.1021/acsami.0c22624.
(242) Li, J.; Jiang, X.; Shang, L.; Li, Z.; Yang, C.; Luo, Y.; Hu, D.; Shen, Y.; Zhang, Z. L-EGCG-Mn Nanoparticles as a pH-Sensitive MRI Contrast Agent. *Drug Deliv.* **2021**, *28* (1), 126–135. https://doi.org/10.1080/10717544.2020.1862363.
(243) Lu, H.; Chen, A.; Zhang, X.; Wei, Z.; Cao, R.; Zhu, Y.; Lu, J.; Wang, Z.; Tian, L. A pH-Responsive T1-T2 Dual-Modal MRI Contrast Agent for Cancer Imaging. *Nat Commun* **2022**, *13* (1), 7948. https://doi.org/10.1038/s41467-022-35655-x.
(244) Cao, Y.; Mao, Z.; He, Y.; Kuang, Y.; Liu, M.; Zhou, Y.; Zhang, Y.; Pei, R. Extremely Small Iron Oxide Nanoparticle-Encapsulated Nanogels as a Glutathione-Responsive T1 Contrast Agent for Tumor-Targeted Magnetic Resonance Imaging. *ACS Appl. Mater. Interfaces* **2020**, *12* (24), 26973–26981. https://doi.org/10.1021/acsami.0c07288.
(245) Liu, D.; Zhou, Z.; Wang, X.; Deng, H.; Sun, L.; Lin, H.; Kang, F.; Zhang, Y.; Wang, Z.; Yang, W.; Rao, L.; Yang, K.; Yu, G.; Du, J.; Shen, Z.; Chen, X. Yolk-Shell Nanovesicles Endow Glutathione-Responsive Concurrent Drug Release and T1 MRI Activation for Cancer Theranostics. *Biomaterials* **2020**, *244*, 119979. https://doi.org/10.1016/j.biomaterials.2020.119979.
(246) Liu, F.; Gong, S.; Shen, M.; He, T.; Liang, X.; Shu, Y.; Wang, X.; Ma, S.; Li, X.; Zhang, M.; Wu, Q.; Gong, C. A Glutathione-Activatable Nanoplatform for Enhanced Photodynamic Therapy with Simultaneous Hypoxia Relief and Glutathione Depletion. *J. Chem. Eng.* **2021**, *403*, 126305. https://doi.org/10.1016/j.cej.2020.126305.
(247) Bonnet, C. S.; Tóth, É. Metal-Based Environment-Sensitive MRI Contrast Agents. *Curr Opin Chem Biol* **2021**, *61*, 154–169. https://doi.org/10.1016/j.cbpa.2021.01.013.
(248) Major, J. L.; Parigi, G.; Luchinat, C.; Meade, T. J. The Synthesis and in Vitro Testing of a Zinc-Activated MRI Contrast Agent. *Proc. Natl. Acad. Sci.* **2007**, *104* (35), 13881–13886. https://doi.org/10.1073/pnas.0706247104.
(249) Zhao, Z.; Wang, X.; Zhang, Z.; Zhang, H.; Liu, H.; Zhu, X.; Li, H.; Chi, X.; Yin, Z.; Gao, J. Real-Time Monitoring of Arsenic Trioxide Release and Delivery by Activatable T1 Imaging. *ACS Nano* **2015**, *9* (3), 2749–2759. https://doi.org/10.1021/nn506640h.
(250) Saharan, S.; Mandal, P. K. The Emerging Role of Glutathione in Alzheimer's Disease. *J. Alzheimer's Dis.* **2014**, *40* (3), 519–529. https://doi.org/10.3233/JAD-132483.
(251) Mandal, P. K.; Saharan, S.; Tripathi, M.; Murari, G. Brain Glutathione Levels – A Novel Biomarker for Mild Cognitive Impairment and Alzheimer's Disease. *Biol. Psychiatry* **2015**, *78* (10), 702–710. https://doi.org/10.1016/j.biopsych.2015.04.005.
(252) Lin, C.-H.; Lane, H.-Y. Plasma Glutathione Levels Decreased with Cognitive Decline among People with Mild Cognitive Impairment (MCI): A Two-Year Prospective Study. *Antioxidants* **2021**, *10* (11), 1839. https://doi.org/10.3390/antiox10111839.
(253) Chen, J. J.; Thiyagarajah, M.; Song, J.; Chen, C.; Herrmann, N.; Gallagher, D.; Rapoport, M. J.; Black, S. E.; Ramirez, J.; Andreazza, A. C.; Oh, P.; Marzolini, S.; Graham, S. J.; Lanctôt, K. L. Altered Central and Blood Glutathione in Alzheimer's Disease and Mild Cognitive Impairment: A Meta-Analysis. *Alz Res Therapy* **2022**, *14* (1), 23. https://doi.org/10.1186/s13195-022-00961-5.

(254) Sekhar, R. V.; McKay, S. V.; Patel, S. G.; Guthikonda, A. P.; Reddy, V. T.; Balasubramanyam, A.; Jahoor, F. Glutathione Synthesis Is Diminished in Patients With Uncontrolled Diabetes and Restored by Dietary Supplementation With Cysteine and Glycine. *Diabetes Care* **2011**, *34* (1), 162–167. https://doi.org/10.2337/dc10-1006.
(255) Lutchmansingh, F. K.; Hsu, J. W.; Bennett, F. I.; Badaloo, A. V.; McFarlane-Anderson, N.; Gordon-Strachan, G. M.; Wright-Pascoe, R. A.; Jahoor, F.; Boyne, M. S. Glutathione Metabolism in Type 2 Diabetes and Its Relationship with Microvascular Complications and Glycemia. *PLoS One* **2018**, *13* (6), e0198626. https://doi.org/10.1371/journal.pone.0198626.
(256) Azarova, I.; Klyosova, E.; Polonikov, A. The Link between Type 2 Diabetes Mellitus and the Polymorphisms of Glutathione-Metabolizing Genes Suggests a New Hypothesis Explaining Disease Initiation and Progression. *Life* **2021**, *11* (9), 886. https://doi.org/10.3390/life11090886.
(257) Gius, D.; Spitz, D. R. Redox Signaling in Cancer Biology. *Antioxid. Redox Signal.* **2006**, *8* (7–8), 1249–1252. https://doi.org/10.1089/ars.2006.8.1249.
(258) Gamcsik, M. P.; Kasibhatla, M. S.; Teeter, S. D.; Colvin, O. M. Glutathione Levels in Human Tumors. *Biomarkers* **2012**, *17* (8), 671–691. https://doi.org/10.3109/1354750X.2012.715672.
(259) Kennedy, L.; Sandhu, J. K.; Harper, M.-E.; Cuperlovic-Culf, M. Role of Glutathione in Cancer: From Mechanisms to Therapies. *Biomolecules* **2020**, *10* (10), 1429. https://doi.org/10.3390/biom10101429.
(260) Valenti, G. E.; Tasso, B.; Traverso, N.; Domenicotti, C.; Marengo, B. Glutathione in Cancer Progression and Chemoresistance: An Update. *Redox Exp Med* **2023**, *2023* (1). https://doi.org/10.1530/REM-22-0023.
(261) Reddy, V. P.; Zhu, X.; Perry, G.; Smith, M. A. Oxidative Stress in Diabetes and Alzheimer's Disease. *J Alzheimers Dis* **2009**, *16* (4), 763–774. https://doi.org/10.3233/JAD-2009-1013.
(262) Zhu, X.; Su, B.; Wang, X.; Smith, M. A.; Perry, G. Causes of Oxidative Stress in Alzheimer Disease. *Cell. Mol. Life Sci.* **2007**, *64* (17), 2202–2210. https://doi.org/10.1007/s00018-007-7218-4.
(263) Zhang, P.; Li, T.; Wu, X.; Nice, E. C.; Huang, C.; Zhang, Y. Oxidative Stress and Diabetes: Antioxidative Strategies. *Front. Med.* **2020**, *14* (5), 583–600. https://doi.org/10.1007/s11684-019-0729-1.
(264) Petrova, V.; Annicchiarico-Petruzzelli, M.; Melino, G.; Amelio, I. The Hypoxic Tumour Microenvironment. *Oncogenesis* **2018**, *7* (1), 1–13. https://doi.org/10.1038/s41389-017-0011-9.
(265) Bansal, A.; Simon, M. C. Glutathione Metabolism in Cancer Progression and Treatment Resistance. *J. Cell Biol.* **2018**, *217* (7), 2291–2298. https://doi.org/10.1083/jcb.201804161.
(266) Boedtkjer, E.; Pedersen, S. F. The Acidic Tumor Microenvironment as a Driver of Cancer. *Annu. Rev. Physiol.* **2020**, *82* (1), 103–126. https://doi.org/10.1146/annurev-physiol-021119-034627.
(267) Xu, H. N.; Li, L. Z. Redox Subpopulations and the Risk of Cancer Progression: A New Method for Characterizing Redox Heterogeneity. In *Photonic Therapeutics and Diagnostics XII*; SPIE, 2016; Vol. 9689, pp 396–402. https://doi.org/10.1117/12.2208267.
(268) Perry, R. R.; Mazetta, J.; Levin, M.; Barranco, S. C. Glutathione Levels and Variability in Breast Tumors and Normal Tissue. *Cancer* **1993**, *72* (3), 783–787.

https://doi.org/10.1002/1097-0142(19930801)72:3<783::AID-CNCR2820720325>3.0.CO;2-U.
(269) Chung, W. J.; Chung, H. W.; Shin, M. J.; Lee, S. H.; Lee, M. H.; Lee, J. S.; Kim, M.-J.; Lee, W. K. MRI to Differentiate Benign from Malignant Soft-Tissue Tumours of the Extremities: A Simplified Systematic Imaging Approach Using Depth, Size and Heterogeneity of Signal Intensity. *Br. J. Radiol.* **2012**, *85* (1018), e831–e836. https://doi.org/10.1259/bjr/27487871.
(270) Kuppusamy, P.; Li, H.; Ilangovan, G.; Cardounel, A. J.; Zweier, J. L.; Yamada, K.; Krishna, M. C.; Mitchell, J. B. Noninvasive Imaging of Tumor Redox Status and Its Modification by Tissue Glutathione Levels1. *Cancer Res.* **2002**, *62* (1), 307–312.
(271) Reed, D. J.; Babson, J. R.; Beatty, P. W.; Brodie, A. E.; Ellis, W. W.; Potter, D. W. High-Performance Liquid Chromatography Analysis of Nanomole Levels of Glutathione, Glutathione Disulfide, and Related Thiols and Disulfides. *Anal. Biochem.* **1980**, *106* (1), 55–62. https://doi.org/10.1016/0003-2697(80)90118-9.
(272) Hamad, A.; Elshahawy, M.; Negm, A.; Mansour, F. R. Analytical Methods for Determination of Glutathione and Glutathione Disulfide in Pharmaceuticals and Biological Fluids. *Rev Anal Chem* **2019**, *38* (4). https://doi.org/10.1515/revac-2019-0019.
(273) Wang, X.; Chi, D.; Song, D.; Su, G.; Li, L.; Shao, L. Quantification of Glutathione in Plasma Samples by HPLC Using 4-Fluoro-7-Nitrobenzofurazan as a Fluorescent Labeling Reagent. *J. Chromatogr. Sci.* **2012**, *50* (2), 119–122. https://doi.org/10.1093/chromsci/bmr039.
(274) Govindaraju, V.; Young, K.; Maudsley, A. A. Proton NMR Chemical Shifts and Coupling Constants for Brain Metabolites. *NMR Biomed.* **2000**, *13* (3), 129–153. https://doi.org/10.1002/1099-1492(200005)13:3<129::AID-NBM619>3.0.CO;2-V.
(275) Carrera, C.; Digilio, G.; Baroni, S.; Burgio, D.; Consol, S.; Fedeli, F.; Longo, D.; Mortillaro, A.; Aime, S. Synthesis and Characterization of a Gd(III) Based Contrast Agent Responsive to Thiol Containing Compounds. *Dalton Trans.* **2007**, No. 43, 4980–4987. https://doi.org/10.1039/B705088G.
(276) Tsitovich, P. B.; Burns, P. J.; McKay, A. M.; Morrow, J. R. Redox-Activated MRI Contrast Agents Based on Lanthanide and Transition Metal Ions. *J. Inorg. Biochem.* **2014**, *133*, 143–154. https://doi.org/10.1016/j.jinorgbio.2014.01.016.
(277) Li, Y.; An, L.; Lin, J.; Tian, Q.; Yang, S. Smart Nanomedicine Agents for Cancer, Triggered by pH, Glutathione, H2O2, or H2S. *Int J Nanomedicine* **2019**, *14*, 5729–5749. https://doi.org/10.2147/IJN.S210116.
(278) Ding, Y.; Dai, Y.; Wu, M.; Li, L. Glutathione-Mediated Nanomedicines for Cancer Diagnosis and Therapy. *Chemical Engineering Journal* **2021**, *426*, 128880. https://doi.org/10.1016/j.cej.2021.128880.
(279) Sun, X.; Guo, F.; Ye, Q.; Zhou, J.; Han, J.; Guo, R. Fluorescent Sensing of Glutathione and Related Bio-Applications. *Biosensors* **2022**, *13* (1), 16. https://doi.org/10.3390/bios13010016.
(280) Sun, X.; Zhang, G.; Du, R.; Xu, R.; Zhu, D.; Qian, J.; Bai, G.; Yang, C.; Zhang, Z.; Zhang, X.; Zou, D.; Wu, Z. A Biodegradable MnSiO3@Fe3O4 Nanoplatform for Dual-Mode Magnetic Resonance Imaging Guided Combinatorial Cancer Therapy. *Biomater.* **2019**, *194*, 151–160. https://doi.org/10.1016/j.biomaterials.2018.12.004.
(281) Gao, Z.; Hou, Y.; Zeng, J.; Chen, L.; Liu, C.; Yang, W.; Gao, M. Tumor Microenvironment-Triggered Aggregation of Antiphagocytosis 99mTc-Labeled Fe3O4

Nanoprobes for Enhanced Tumor Imaging In Vivo. *Adv Mater* **2017**, *29* (24), 1701095. https://doi.org/10.1002/adma.201701095.
(282) Bolles, G.; Spampinato, M. V. Chapter 20 - Magnetic Resonance Contrast Agents for Neuroradiology: Current Status. In *Handbook of Neuro-Oncology Neuroimaging (Second Edition)*; Newton, H. B., Ed.; Academic Press: San Diego, 2016; pp 183–192. https://doi.org/10.1016/B978-0-12-800945-1.00020-3.
(283) Sieber, M. A.; Lengsfeld, P.; Walter, J.; Schirmer, H.; Frenzel, T.; Siegmund, F.; Weinmann, H.-J.; Pietsch, H. Gadolinium-Based Contrast Agents and Their Potential Role in the Pathogenesis of Nephrogenic Systemic Fibrosis: The Role of Excess Ligand. *J Magn Reson Imaging* **2008**, *27* (5), 955–962. https://doi.org/10.1002/jmri.21368.
(284) Thakral, C.; Alhariri, J.; Abraham, J. L. Long-Term Retention of Gadolinium in Tissues from Nephrogenic Systemic Fibrosis Patient after Multiple Gadolinium-Enhanced MRI Scans: Case Report and Implications. *Contrast Media Mol Imaging* **2007**, *2* (4), 199–205. https://doi.org/10.1002/cmmi.146.
(285) Kanda, T.; Fukusato, T.; Matsuda, M.; Toyoda, K.; Oba, H.; Kotoku, J.; Haruyama, T.; Kitajima, K.; Furui, S. Gadolinium-Based Contrast Agent Accumulates in the Brain Even in Subjects without Severe Renal Dysfunction: Evaluation of Autopsy Brain Specimens with Inductively Coupled Plasma Mass Spectroscopy. *Radiology* **2015**, *276* (1), 228–232. https://doi.org/10.1148/radiol.2015142690.
(286) Radbruch, A.; Weberling, L. D.; Kieslich, P. J.; Eidel, O.; Burth, S.; Kickingereder, P.; Heiland, S.; Wick, W.; Schlemmer, H.-P.; Bendszus, M. Gadolinium Retention in the Dentate Nucleus and Globus Pallidus Is Dependent on the Class of Contrast Agent. *Radiology* **2015**, *275* (3), 783–791. https://doi.org/10.1148/radiol.2015150337.
(287) Elizondo, G.; Fretz, C. J.; Stark, D. D.; Rocklage, S. M.; Quay, S. C.; Worah, D.; Tsang, Y. M.; Chen, M. C.; Ferrucci, J. T. Preclinical Evaluation of MnDPDP: New Paramagnetic Hepatobiliary Contrast Agent for MR Imaging. *Radiology* **1991**, *178* (1), 73–78. https://doi.org/10.1148/radiology.178.1.1898538.
(288) Pan, D.; Schmieder, A. H.; Wickline, S. A.; Lanza, G. M. Manganese-Based MRI Contrast Agents: Past, Present and Future. *Tetrahedron* **2011**, *67* (44), 8431–8444. https://doi.org/10.1016/j.tet.2011.07.076.
(289) Rolla, G. A.; Platas-Iglesias, C.; Botta, M.; Tei, L.; Helm, L. 1H and 17O NMR Relaxometric and Computational Study on Macrocyclic Mn(II) Complexes. *Inorg. Chem.* **2013**, *52* (6), 3268–3279. https://doi.org/10.1021/ic302785m.
(290) Tummanapelli, A. K.; Vasudevan, S. Ab Initio MD Simulations of the Brønsted Acidity of Glutathione in Aqueous Solutions: Predicting pK_a Shifts of the Cysteine Residue. *J. Phys. Chem. B* **2015**, *119* (49), 15353–15358. https://doi.org/10.1021/acs.jpcb.5b10093.
(291) Xie, R.-G.; Zhang, Z.-J.; Yan, J.-M.; Yuan, D.-Q. Selective Mono- and Bis-Oxidation of 2,6-Bis(Hydroxy-Methyl) Phenols with Active Manganese Dioxide. *Synth. Commun.* **1994**, *24* (1), 53–58. https://doi.org/10.1080/00397919408012625.
(292) Tomasulo, M.; Kaanumal, S. L.; Sortino, S.; Raymo, F. M. Synthesis and Properties of Benzophenone−Spiropyran and Naphthalene−Spiropyran Conjugates. *J. Org. Chem.* **2007**, *72* (2), 595–605. https://doi.org/10.1021/jo062004d.
(293) Li, C.; Wong, W.-T. A Simple, Regioselective Synthesis of 1,4-Bis(Tert-Butoxycarbonylmethyl)- Tetraazacyclododecane. *J. Org. Chem.* **2003**, *68* (7), 2956–2959. https://doi.org/10.1021/jo026436+.